

**D R A F T**  
**FINAL REPORT**  
for

**FRP-CONCRETE COMPOSITE COLUMN  
AND  
PILE JACKET SPLICING  
PHASE II**

WPI 0510700  
Contract B-9895  
State Job 99700-7604-119

Prepared for  
Dr. Mohsen Shahawy, Director  
Structural Research Center  
**The Florida Department of Transportation**  
Tallahassee, Florida

Prepared by  
Dr. Amir Mirmiran, P.E.  
Department of Civil & Environmental Engineering  
**University of Central Florida**  
Orlando, Florida

July 31, 1997

## TABLE OF CONTENTS

<u>Description</u>	<u>Page</u>
Acknowledgements	iii
List of Tables	iv
List of Figures	v
Executive Summary	viii
Problem Statement	viii
Objective	viii
Findings	viii
Conclusions	ix
1 Introduction	1
1.1 Problem Statement	1
1.2 Research Objectives	1
1.3 Report Outline	2
2 Shear Strength of Concrete-Filled FRP Tubes	3
2.1 Literature Review	3
2.2 Experimental Work	5
2.3 Analysis and Discussion	20
3 Effect of Cross Section on Confinement	29
3.1 Literature Review	29
3.2 Experimental Work	31
3.3 Analysis and Discussion	51
4 Effect of Column Length on Confinement	63
4.1 Literature Review	63
4.2 Length Effect Tests	64
4.3 Analysis and Discussion	74
5 Effect of Bond on Confinement	91
5.1 Background	91
5.2 Bond Effect Tests	92
6 Cost Optimization	110
6.1 Literature Review	110
6.2 Cost Optimization Program	111
6.3 Analysis and Discussion	115
7 Acoustic Emission	124
7.1 Literature Review	124
7.2 Characteristics of Acoustic Emission Signals	125
7.3 Acoustic Emission Tests	128
8 Conclusions	135
9 Dissemination	138
References	142

## **ACKNOWLEDGEMENTS**

The author would like to thank his Project Manager, Dr. Mohsen Shahawy, Director, Structural Research Center for his help, time, and encouragements during the course of this project. His valuable and timely suggestions helped avoid many pitfalls that are often parts of any research project. The author takes this opportunity to also thank the personnel of Florida Department of Transportation, Structural Research Center, and in particular, Tom Beitelman.

This project was made possible by generous donations of Marine Muffler Corp. of Apopka, Florida in the form of materials and labor. For this, the author is grateful to Mr. David Parks and his associates. Partial student support was also received from the University of Central Florida Division of Sponsored Research and the Department of Civil and Environmental Engineering.

Special thanks are due to graduate assistants at the University of Central Florida, Ph.D. candidate Michel Samaan, M.S. graduates Mike Scherer, Suramy Cabrera, Odell Pico, Hazem El Echary, and Juan Carlos Mastrapa. Portions of this report correspond to the theses and dissertations of these students.

## **List of Tables**

<b><u>Table</u></b>	<b><u>Page</u></b>
2.1 Test matrix for Series 1	7
2.2 Mechanical properties of glass fibers, polyester resin, and carbon sheet	7
2.3 Test results for Series 1	15
2.4 Test matrix for Series 2	16
2.5 Test results for Series 2	20
3.1 Test matrix	32
3.2 Summary of results for unconfined specimens	40
3.3 Summary of results for confined specimens	40
3.4 Material properties for fiber composites (Rochette 1997)	58
3.5 Test matrix and results of uniaxial compression tests by Rochette (1997)	59
4.1 Test matrix for length effect specimens	65
4.2 Test results for length effect specimens	69
4.3 Calculated eccentricity ratios for length effect specimens	90
5.1 Manufacturer's data for 57%-63% S-2 glass fiber unidirectional epoxy composite	93
5.2 Test results for bond effect specimens	99
5.3 Split-disk test results	107
6.1 Relative material density and cost (Deskovic, Triantafillou, and Meier 1995)	112

## List of Figures

<u>Figure</u>	<u>Page</u>
2.1 Specimen layout for Series 1	6
2.2 Control beams prior to casting of concrete	8
2.3 FRP tubes with re-bars prior to casting of concrete	8
2.4 Instrumentation of beam specimens	10
2.5 Beam shear test set up	10
2.6 Beam C2 after failure showing extreme slippage	11
2.7 Beam C2 with bulged and separated jacket	11
2.8 Beam C2 after failure (side view)	12
2.9 Beam B2 after failure showing crack inclination at fiber orientation	12
2.10 Interior of Beam B2 after failure	14
2.11 Beam B2 after failure	14
2.12 Beam D2 after failure	15
2.13 Specimen layout for Series 2	17
2.14 Control Beam E1 after failure	19
2.15 Beam G2 after failure	19
2.16 Load versus top strain for specimens of Series 2	21
2.17 Load versus bottom strain for specimens of Series 2	22
2.18 Moment-curvature for specimens of Series 2	23
2.19 Shear crack in a rectangular FRP beam with only hoop fibers	25
2.20 Shear crack in a rectangular FRP beam with $\pm\phi$ angle plies	25
2.21 Shear crack in a circular FRP beam with $\pm\phi$ angle plies	27
3.1 Grooving of the square tubes	33
3.2 Capping device for square sections	33
3.3 Instrumentation for a square tube	35
3.4 Specimen SQ6C after reloading	35
3.5 10-ply specimens after failure	36
3.6 14-ply specimens after failure	36
3.7 Stress-strain curves for plain concrete cylindrical (control) specimens	38
3.8 Stress-strain curves for plain concrete square (control) specimens	39
3.9 Biaxial stress-strain for 6-ply concrete-filled square FRP tubes	41
3.10 Biaxial stress-strain for 10-ply concrete-filled square FRP tubes	42
3.11 Biaxial stress-strain for 14-ply concrete-filled square FRP tubes	43
3.12 Average biaxial stress-strain for concrete-filled square FRP tubes	44
3.13 Average lateral strain versus axial strain for concrete-filled square FRP tubes	46
3.14 Average dilation rates for concrete-filled square FRP tubes	47
3.15 Average axial stress versus volumetric strain for concrete-filled square FRP tubes	49
3.16 Average octahedral loading surfaces for concrete-filled square FRP tubes	50
3.17 Average stress-strain curves for circular and square FRP tubes	52
3.18 Normalized stress-strain curves for circular and square FRP tubes	53

3.19 Normalized volumetric strain curves for circular and square FRP tubes	55
3.20 Dilation curves for circular and square FRP tubes	56
3.21 Lateral pressure buildup in square and circular sections	57
3.22 Ultimate strength ratio versus $\left(\frac{2R}{D}\right)\frac{f_{ru}}{f'_{\infty}}$	61
4.1 Instrumentation of composite tubes	65
4.2 Composite specimen with full instrumentation prior to loading	67
4.3 14-ply 18" tall specimens after failure	67
4.4 6-ply 24" tall specimens after failure	68
4.5 10-ply 30" tall specimens after failure	68
4.6 Stress-strain curves for 12" specimens	70
4.7 Stress-strain curves for 18" specimens	71
4.8 Stress-strain curves for 24" specimens	72
4.9 Stress-strain curves for 30" specimens	73
4.10 Stress-strain curves for 6-layer specimens	75
4.11 Stress-strain curves for 10-layer specimens	76
4.12 Stress-strain curves for 14-layer specimens	77
4.13 Axial stress versus volumetric strain for 6-layer specimens	78
4.14 Axial stress versus volumetric strain for 10-layer specimens	79
4.15 Axial stress versus volumetric strain for 14-layer specimens	80
4.16 Normalized ultimate strength versus L/D ratio	81
4.17 Normalized ultimate strain versus L/D ratio	82
4.18 Predicted versus experimental values of ultimate strength	85
4.19 Strain distribution along height of S10-24-2	87
4.20 Strain distribution along height of S14-30-1	88
4.21 Defining eccentricities based on strain variations	89
5.1 Collapsible mandrel with two S-glass tubes	95
5.2 Test setup and instrumentation	95
5.3 Failure of 1-layer unbonded specimens	96
5.4 Failure of 1-layer bonded specimens	96
5.5 Failure of 3-layer unbonded specimens	97
5.6 Failure of 3-layer bonded specimens	97
5.7 Failure of 5-layer unbonded specimens	98
5.8 Failure of 5-layer bonded specimens	98
5.9 A 7-layer unbonded specimen after removal of the jacket	101
5.10 A 7-layer bonded specimen after removal of the jacket	101
5.11 Stress-strain curves for bonded and unbonded specimens	102
5.12 Lateral strain versus axial strain	103
5.13 Volumetric strain versus axial strain	104
5.14 Axial stress versus volumetric strain	105
5.15 Dilation rate versus axial strain	106
5.16 Specimen-tab geometry for the tension coupon tests	109

6.1 Discretization of hybrid section	114
6.2 Tension control failure in hybrid column	116
6.3 Compression control failure in hybrid column	116
6.4 Normalized interaction diagrams for hybrid columns	117
6.5 Normalized moment-curvature diagrams for a hybrid column	119
6.6 Relative material cost versus reinforcement ratio for various core diameters	120
6.7 Relative material cost versus reinforcement ratio for various bending moments	121
6.8 Schematic cost optimization for hybrid columns	122
6.9 Relative total costs versus core diameter for various penalty functions	123
7.1 Propagation and detection of AE signals	126
7.2 Types of acoustic emission signals	126
7.3 Acoustic emission signal features	127
7.4 Kaiser effect and Felicity effect	127
7.5 Mounting of sensors on the specimens	128
7.6 Test setup for Specimen S6-24-1 with four sensors prior to loading	130
7.7 Preamplifiers located near the specimen	130
7.8 Hardware setup dialog box showing selected hardware settings	131
7.9 Effect of confinement on AE counts	133
7.10 Felicity effect for a 7-layer S-glass jacketed concrete specimen	134

# EXECUTIVE SUMMARY

## Problem Statement

Issues of corrosion and deterioration of steel reinforcement have led to the use of fiber reinforced plastics (FRP) in infrastructure. Florida DOT has been in the forefront of using FRP for the repair of existing bridges. A new and innovative use of fiber composites has been introduced by Virmiran and Shahawy that consists of concrete-filled FRP tubes as structural columns, piles and piers. The tube acts as the pour form, protective and confining jacket, shear stirrups, and flexural reinforcement, all at the same time. It further allows removing conventional reinforcement from the column. Feasibility of this method of construction was clearly demonstrated under Phase I of this research project. Phase I also resulted in a new model for confined concrete, and new methods of fabricating hybrid beam columns. Phase II of this research has been focused on several issues including; shear capacity of hybrid FRP-concrete columns, effect of cross-sectional shape on the degree of confinement provided by the FRP shell, effect of length and slenderness of hybrid columns on their strength and ductility, effect of bond between the concrete core and the FRP shell on the strength and ductility, and finally optimization of hybrid columns.

## Objective

The following objectives were identified for Phase II:

1. Evaluate the shear capacity of hybrid columns and develop methods to increase shear transfer between the tube and the concrete core.
2. Study the effect of cross-sectional shape, length or slenderness of the column, and bond between the tube and the core, on the strength and ductility of hybrid columns.
3. Develop procedures for optimization of hybrid FRP-concrete columns, and perform parametric studies to establish the effects of basic variables on the cost of the system.

## Findings

The experimental and analytical studies of Phase II led to several findings as outlined below:

1. Shear tests on a total of 16 hybrid beams indicated that unless shear ribs are provided, hardly any bond would exist naturally between the FRP jacket and the concrete core. As a result, slippage would not allow shear to be transferred at the concrete-FRP interface. The tube, however, still somewhat increases the shear strength of concrete by simply containing the cracked section. With the shear connectors, the slippage problem was corrected, and the tube increased the strength by at least 6 times the shear strength of unjacketed beams of the same cross section. Also, the ribbed FRP tubes proved effective in inhibiting shear failure of the beams.

2. Uniaxial compression tests on a total of 9 composite specimens with square section demonstrated that square sections are not as effective as circular sections in confining the concrete core, as the strength of concrete is increased only marginally and rather independent of the jacket thickness. However, a post-peak ductility can be expected. Failure of the square FRP-encased



specimens is accompanied by white patches around the corners, showing stress concentration at the edges. As the corner radius is increased, the confinement effectiveness and the behavior of confined concrete become closer to circular sections. The over-riding parameter in controlling

3. Uniaxial compression tests on a total of 24 composite columns with various lengths and jacket thicknesses indicated that length-to-diameter ratios of up to 5:1 would not alter the general behavior of confined concrete such as its mode of failure or dilation characteristics. No slenderness effect in the form of buckling was observed during the tests. Further analysis indicated that the maximum eccentricity was within 10-12% of the section width. Noting that ACI 318-95 considers a minimum\_eccentricity of 10% and a strength reduction of 20% for tied columns, the amount of eccentricity and the strength reductions that were noticed for L/D ratios of 2:1 to 5:1 seemed acceptable. It was therefore, concluded that the 12" cylinders should be considered adequate to represent the confinement of concrete sections. Longer specimens possess an inherent eccentricity that results in lower values of the ultimate load. However, the eccentricity is well within the acceptable range, and does not qualify for any slenderness effect.

4. Uniaxial compression tests on a total of 24 composite specimens with and without construction bond and with various jacket thicknesses indicated that the effect of construction bond on confined concrete is not significant, as long as the biaxial stresses in the jacket are considered properly for the bonded specimens.

5. Optimization studies for a variety of jacket thicknesses and core diameters indicated that adding hoop fibers at low axial loads does not increase the capacity of the section. For a specific core diameter, there is only one particular combination of axial and hoop fibers that provides the optimum solution. A penalty function was introduced to determine the significance of weight on the total cost of a hybrid column. When weight becomes a significant factor, the optimum solution shifts to a lower core diameter and higher hoop and axial fiber reinforcement ratios.

6. Acoustic emission (AE) was shown to be an efficient nondestructive evaluation technique for concrete-filled FRP tubes. Of the various AE parameters, AE energy and number of AE counts both proved to be effective measures for the response of confined concrete. It was shown that while Kaiser effect was not present for hybrid columns even at low levels of axial load, Felicity effect during loading and unloading was apparent as one would expect from fiber composites.

## Conclusions

A series of beam and column tests with a variety of design parameters helped quantify the response of hybrid FRP-concrete columns as related to shear strength, confinement, cross-section, slenderness, and construction bond. It was shown that design of hybrid columns can be optimized for any load combination and core diameter. Finally, effective use of nondestructive methods for FRP-concrete columns was demonstrated. Phase III of this project will focus on field testing of concrete filled FRP piles.

# CHAPTER 1

## INTRODUCTION

### 1.1 Problem Statement

Issues of corrosion and deterioration of steel reinforcement have led to the use of fiber composites in infrastructure. A new and innovative use of fiber composites was introduced by Mirmiran and Shahawy (1995) that consisted of concrete-filled fiber reinforced plastics (FRP) tube as structural columns, piles and piers. This idea was supported by the Florida Department of Transportation under Phase I of a research effort which was completed in 1996. Details of the construction technique, its benefits, and a multitude of useful information are provided in the Final Report of Phase I (Mirmiran 1997). That report forms the basis (or Volume I) of this document, and rather than unnecessary duplication of the materials, multiple references to that report have been made throughout this document.

Phase I of this research was focused more towards investigating the feasibility of the construction method, modeling of confined concrete, and methods of fabricating hybrid beam-columns. There were, however, several other issues that remained to be studied before the proposed system could be fully implemented. Those issues include the following:

1. Shear capacity of hybrid FRP-concrete columns.
2. Effect of cross-sectional shape on the degree of confinement provided by the FRP shell.
3. Effect of length and slenderness of hybrid columns on their strength and ductility.
4. Effect of bond between the concrete core and FRP shell on the strength and ductility.
5. Design procedures, optimization, and cost-benefit analysis for hybrid columns.
6. Field tests of hybrid columns and piles.
7. Design issues such as connections, long-term performance, environmental effects, etc.

Of the above items, the first five have been investigated under Phase II, and will be addressed in this report. Item 6 is the main focus of Phase III, which undertakes the driving of a hybrid pile at a selected site. The issue of long-term performance under item 7 is the topic of a parallel project with the National Science Foundation and the Florida Department of Transportation.

### 1.2 Research Objectives

The objectives of Phase II may be listed as follows:

1. Evaluate the shear capacity of hybrid columns and develop methods to increase shear

transfer between the tube and the concrete core.

2. Study the effect of cross-sectional shape, length or slenderness of the column, and bond between the tube and the core, on the strength and ductility of hybrid columns. It was intended to quantify these effects and make necessary modifications in the confinement model that was developed under Phase I:
3. Develop procedures for design and cost optimization of hybrid FRP-concrete columns, and perform necessary parametric studies to establish the effects of basic parameters on the cost of the system.

### 1.3 Report Outline

This report consists of nine chapters including this introduction. This Phase of the project consisted of the following program:

1. Beam Shear Tests: to establish the contribution of the FRP tube to the shear strength of the hybrid FRP-concrete beam.
2. Square Column Tests: to evaluate the effect of cross-sectional shape on the confinement provided by the FRP tube.
3. Length Effect Tests: to determine the effect of column length on the strength and ductility of concrete confined in FRP tube.
4. Bond Effect Tests: to compare the confinement effectiveness of fiber-wrapping mechanism versus concrete-filled FRP tubes.
5. Cost Optimization: to develop an analytical technique for design optimization of hybrid columns.
6. Acoustics Emission Tests: to develop a non-destructive testing method for predicting the strength of concrete-filled FRP tubes.

Of these, items 1, 4 and 6 were in the original proposal, while others were added during the course of the project. The next six chapters cover the various elements of this research as outlined above. Each chapter contains a section on literature review, experimental work (except for the chapter on cost optimization) and analysis and discussion (except for the chapter on Acoustics Emission). Chapter 8 summarizes the conclusions and discusses various recommendations. A list of all disseminated information is presented in Chapter 9. References are categorized for convenience of the reader. In this report, as in that of Phase I (Mirmiran 1997) the terms FRP-encased concrete, concrete-filled FRP tubes, hybrid FRP-concrete columns, and composite FRP-concrete columns are used interchangeably to mean the same system.

## **CHAPTER 2**

### **SHEAR STRENGTH OF CONCRETE-FILLED FRP TUBES**

#### 2.1 Literature Review

Fiber reinforced plastics (FRP) sheets and plates have often been used for repair or strengthening of beams and slabs. Bonding of FRP sheets was used in Lucerne, Switzerland to repair the Ibach Bridge when it was accidentally damaged resulting in a decreased load carrying capacity for the bridge. It was estimated that 175 kg of steel plates would have been needed to repair the bridge. Instead, only 6.2 kg of carbon fiber sheets were needed for the same repair (McKenna and Erki 1994). It was also reported that the Kattenbusch bridge in Germany was repaired with both steel and glass fiber reinforced plastic (GFRP) plates. In addition, it was noted that the GFRP plates provided the same increase in strength as the steel plates (Nanni 1995). Saadatmanesh and Eshani (1991) investigated strengthening of beams with externally bonded GFRP plates. Tests were conducted on five rectangular beams and one T-beam. Of the five beams, one was under-designed for shear and the rest were over-designed in shear according to ACI code. The flexural reinforcement included steel bars of three different reinforcement ratios. All beams were strengthened with FRP plates externally bonded to their tension sides. The test indicated that FRP plates significantly increased the flexural strength of the beams, reduced the crack size of the beams, and slightly reduced ductility. It was also noted that the greatest increase in flexural strength occurred in the beams with lower steel reinforcement ratio. Similar to this experiment was one conducted by Philip et al. (1991). There too, the results indicated an increase in strength and stiffness. None of the beams in this test, however, showed ductile behavior.

Al-Sulaimani et al. (1994a) conducted tests on the strengthening of damaged beams. Tests were conducted on ten reinforced concrete beams. The beams were under-reinforced in flexure and over-designed in shear to avoid a brittle shear failure of the damaged beams after repair. The beams were initially loaded to 85% of their ultimate load. They were then repaired by plate bonding. The beams were divided into four categories depending on the repair technique. The four categories were as follows:

1. Beams repaired by bonding a plate to the beam soffit.
2. Beams repaired with plate bonded and anchored by steel bolts to the beam soffit.
3. Beams repaired by bonding a plate to the beam soffit and additional plates bonded to the sides of the beam

#### 4. Beams repaired with an I-jacket bonded to the sides and soffit of the beam.

The beams were loaded until failure. Overall, the results indicated that the beams repaired with the bonded I-jacket provided the best anchorage system to eliminate plate separation and diagonal tension failure, and developed the flexural strength of the repaired beams. They also found that beams did show adequate ductility while developing their flexural capacity.

Al Sulaimani et al (1994b) later conducted an experiment on the effectiveness of FRP plate bonding on the shear capacity of reinforced concrete beams. In this test, sixteen reinforced concrete beams were deliberately designed to be deficient in shear capacity. As with the previous test, the beams were then loaded to a predetermined load. The damaged beams were then divided into four groups according to the form of repair. The four repair categories were as follows:

1. Control beams having no shear repair.
2. Beams repaired by shear strips.
3. Beams repaired by shear wings.
4. Beams repaired by U-jackets.

Within these four groups, the beams were further divided into two subgroups, beams having no flexural repair and beams repaired in flexure by FRP plate bonding. The beams were then loaded until failure. In general, the beams repaired with the U-jacket showed the best shear performance. The shear strength was so high that even the U-jacketed beams that were strengthened with additional FRP plates failed in flexure.

Chajes et al. (1995) conducted an experiment on the shear strength of reinforced concrete beams using externally applied composite fabrics. In this study, 12 T-beams were tested. Eight of the beams were wrapped with externally bonded composite fabrics, two were reinforced with woven aramid, E-glass, and graphite fabrics with the weave direction along and perpendicular to the beams' longitudinal axis, and two beams had plain-weave graphite fabric bonded with the weave directions rotated  $\pm 45^\circ$  from the beams' longitudinal axis. The beams were tested in a four-point loading test. All beams failed in shear with the beams reinforced with composite fabric failing at the highest loads. The externally wrapped beams displayed an increase in load carrying capacity of 60% to 150% over the control beams. The beams wrapped with the fabric oriented at  $\pm 45^\circ$  showed the highest increase in strength. It was also noted by the authors that the composite fabric had only a minor effect on the flexural stiffness of the wrapped beams.

In all the research presented, the common conclusion was that the use of fiber composite as a material to reinforce concrete members is a desirable one. Advantages of fiber composites include (Mallick 1988):

1. The high strength-to-weight ratio of FRP helps reduce the weight of the structure, making FRP a more economical choice.
2. Fibers have a lower coefficient of thermal expansion than most metals, giving fibers better

- stability over a wider temperature range.
3. The unique anisotropic properties of fibers allow one to design for stresses in a specific direction, and effectively uncouple the axial and hoop directions.
  4. The tensile stress-strain response of fibers is linear-elastic, while steel yields plastic deformations.
  5. Fiber composites can be used to enhance shear strength of concrete beams.

## 2.2 Experimental Work

An experimental study was performed to evaluate the contribution of FRP to the shear strength of concrete-filled tubes. The proposed study was to test 8 beams under a 4-point loading set up. Two unconfined (unjacketed) beams were used as control beams. These beams were lacking in any form of shear reinforcement so as to ensure a shear failure. The shear strength of the 6 jacketed specimens was then compared to the shear strength of the 2 control specimens. The effect of slippage was not considered to be of great consequence in the beam shear tests. However, it was, and a second series of tests was devised and carried out with beams containing shear connectors. The details of both series of tests are discussed below.

### Series 1

Series 1 consisted of eight 6"x6"x22" beams tested under a 4-point loading set up. The specimens were designed to ensure a shear failure if no FRP jacket was provided. Therefore, the control beams were designed with a flexural strength of about 9 times their shear strength. Clear cover for the compression and tension bars was 0.5 inch and 0.75 inch, respectively (Figure 2.1). The jacketed specimens were reinforced identical to the control beams against flexure, the only difference being the enhanced shear strength provided by the FRP jacket. The jacket was expected to increase the shear strength by over 9 times, changing the failure mode from shear to flexural, assuming full bond with the concrete core.

#### Specimen Layout

Table 2.1 shows the test matrix for Series 1. Eight specimens were divided into four groups with two identical samples from each group for repeatability verification. Two 6"x12" cylinders were also made to determine the average compressive strength of the concrete mix. The characteristics of the four groups are as follows:

1. Group A consisted of the control specimens with no shear reinforcement.
2. Group B specimens were the same as control specimens with the addition of the FRP tube.
3. Group C specimens were FRP jacketed with an additional layer of carbon fiber glued to the inside of the tube prior to casting of concrete to increase flexural strength of the beam.
4. Group D specimens were the same as Group C except that at the time of testing, the top face of the tube was cut and removed, to eliminate the continuity in the fibers.

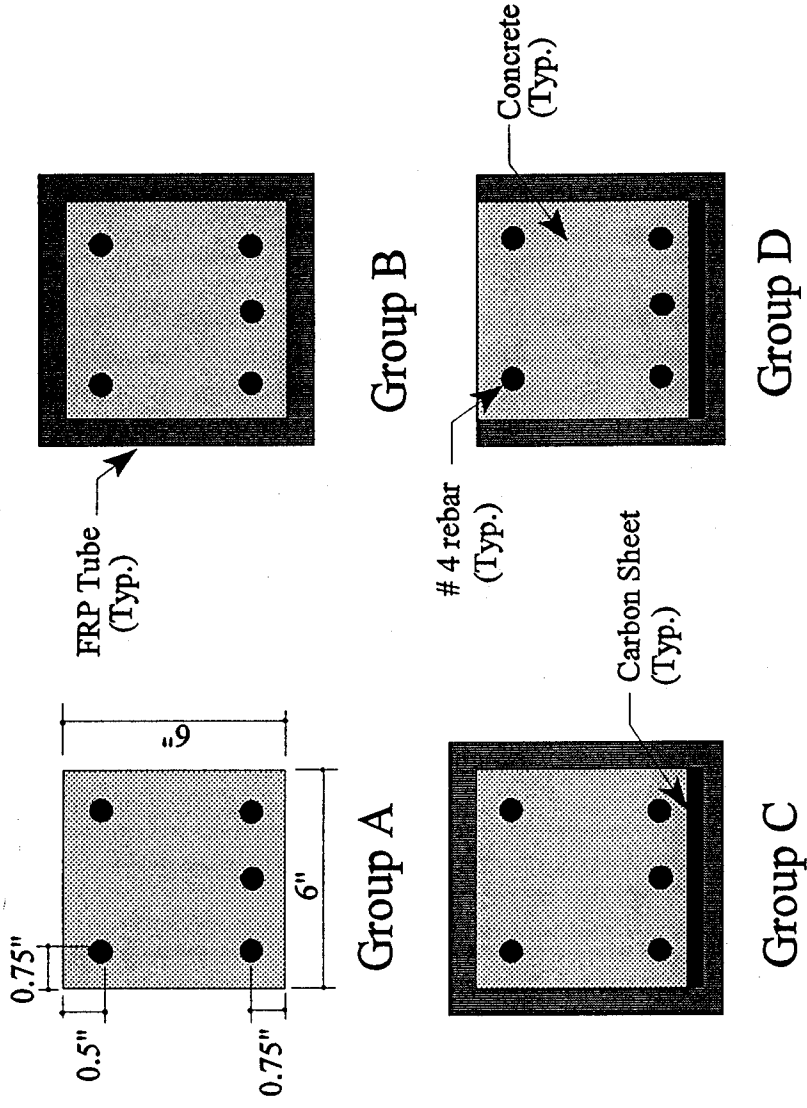


Figure 2.1 Specimen layout for Series 1

**Table 2.1 Test matrix for Series 1**

Group No.	Longitudinal Reinforcement		Shear Reinforcement
	Compression	Tension	
A	2#4 Steel Rebars	3#4 Steel Rebars	None
B	2#4 Steel Rebars	3#4 Steel Rebars	FRP Tube [7 Layers]
C	2#4 Steel Rebars	3#4 Steel Rebars Carbon Fiber Sheet	FRP Tube [7 Layers]
D	2#4 Steel Rebars	3#4 Steel Rebars Carbon Fiber Sheet	FRP Tube [7 Layers] (Top face removed prior to testing)

Tubes were made by Marine Muffler Corporation, Apopka, Florida, and consisted of 7 filament-wound  $\pm 15^\circ$  angle-ply. Material properties of the DION 6692T polyester resin, E-glass R099-660 Roving, and the Thomel T-300 carbon sheet are presented in Table 2.2 from manufacturer's data. The aggregates were provided by the Orlando Paving Company, Winter Park, Florida. Sand was natural silica with a fineness modulus of 2.2, specific gravity of 2.64, dry rodded weight of 101 pcf and moisture absorption of 2.0%. Gravel was crushed limestone with a specific gravity of 2.82, dry rodded weight of 101 pcf, and moisture absorption of 5.4%. Type II Portland Cement from Rinker Materials, Winter Park, Florida was used for concrete.

**Table 2.2 Mechanical properties of glass fibers, polyester resin, and carbon sheet**

Property	450-Yield E-Glass	Polyester Resin	Thornel Carbon Fiber T-300 12k
Specific Gravity	2.58	1.41	1.77
Tensile Strength, (ksi)	317	10.4	530
Tensile Modulus, (ksi)	10,100	630	33,500
Shear Modulus, (ksi)	4,370	232	700
Poisson's Ratio	0.22	0.36	0.20

Figures 2.2 and 2.3 show the placement of re-bars and preparation of the specimens. Re-bars were affixed to the inside of the FRP tubes with wires that were pulled through small holes drilled in the sides of the tubes 0.5 inches from the compression face and 0.75 inches from the tension face. The re-bars were tightly wound with the wires to ensure they would not slip. The bottom of the beams were sealed with a double layer of plastic sheet taped to the bottoms to prevent the concrete from seeping out. Placement of re-bars in the control beams required small U-shaped seats made of steel wire on which the tension re-bars could rest at the required distances. The compression re-bars





Figure 2.2 Control beams prior to casting of concrete

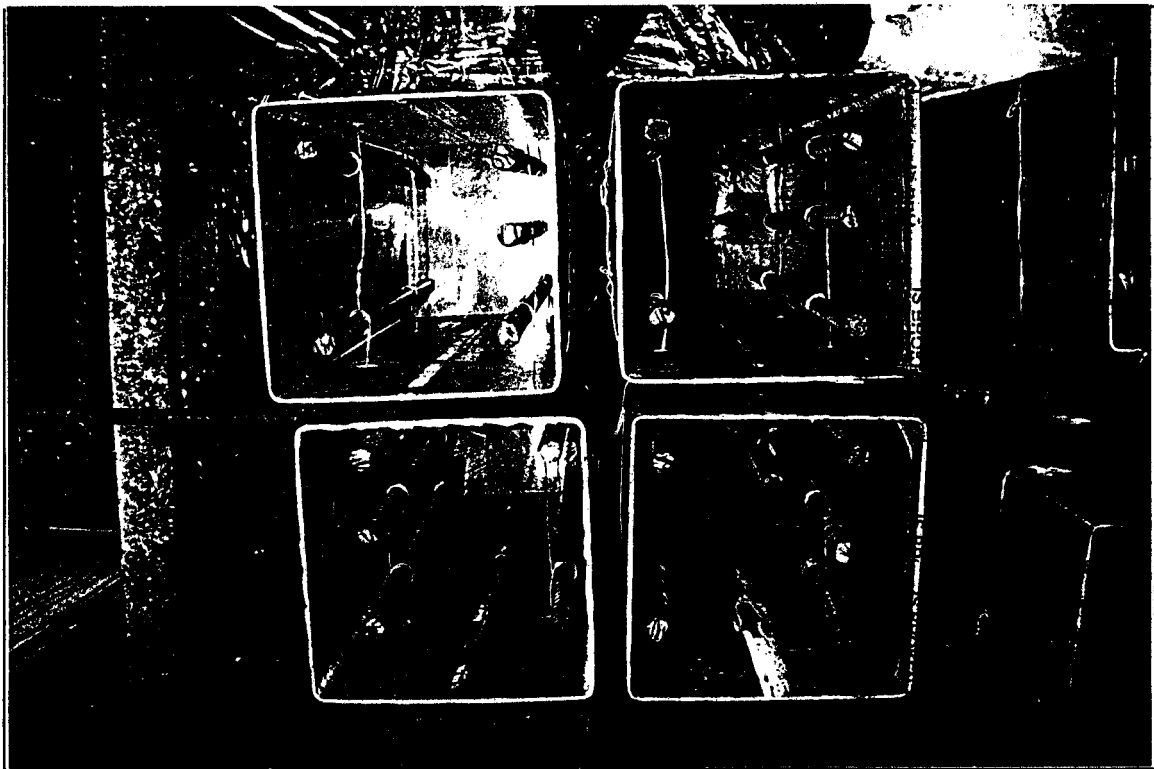


Figure 2.3 FRP tubes with re-bars prior to casting of concrete

were hung with wire at the required height.

The concrete mix was designed with a water-to-cement ratio of 0.52 (by weight) for a 28-day compressive strength of 4000 psi. The quantity of materials per cubic yard of the mix was: 665.61b cement, 344.7 lb water, 1034.11 sand, and 2078.6 lb gravel. No additives were used. Concrete was cast on November 2, 1995 at UCF using a single batch made in a 9 cubic-foot rental mixer. Exposed surface of the specimens were wetted daily for three days. After 1 week of curing outdoors, specimens were brought inside the lab. All control cylinders were sulfur capped prior to testing.

### Instrumentation

All specimens were instrumented with rosettes at mid-height on both sides of the specimens on a 45 ° line between the support and the point of load application (see Figure 2.4). The rosettes measured strain in the horizontal and vertical directions. Strain gages were also placed on the top face of the beams centered vertically and horizontally. All gages were glued onto the surface of the tube or concrete. The beams were additionally instrumented with three LVDTs at the mid-span and under the points of load application. The two control cylinders were instrumented with horizontal strain gages placed 180° apart at mid-height of the specimen.

### Test Procedure

Testing took place on December 9 and 10, 1995 at the MOT Structural Laboratory, using the MTS and MegaDAQ. Test set up for the beams is shown in Figure 2.5. It consisted of two half cylinders affixed at 18" spacing as beam supports and two rollers as loading points at 3" on either side of the midspan. A metal plate was used to transfer the load onto the two rollers. Testing was carried out in a displacement control mode. Rate of loading was 0.05 inch per minute for Specimens A1, B 1, B2, and C1, and 0.125 inch per minute for Specimens A2, C2, D1, and D2.

### Observed Behavior

Throughout testing, significant popping and cracking could be heard. Some of the noises may be attributed to the de-bonding of the tube and cracking of concrete. It was possible to see the concrete slipping out of the tube. At the time of failure, an average of  $\frac{1}{4}$  to  $\frac{1}{2}$  inch of concrete had slipped out of the tube at either end (Figure 2.6). This indicated very little bond between concrete and the tube. Square chunks of concrete at the end of some specimens completely broke off and fell out. Looking in at the ends of the specimens, it was possible to see bulging of the tube (Figure 2.7). The vertical sides of the tube also buckled outward as can be seen on the front face of specimen B2 (Figure 2.8). As the loading progressed, white lines developed in the tube indicating cracking of the tube and flow of resin. Specimens of Group C were the only ones to show flexural cracking. These specimens were even further reinforced with a carbon sheet to increase the flexural strength above that of other specimens. It is possible that the weave of the carbon sheet helped inhibit slippage on the tension face of concrete resulting in a more successful transfer of load between concrete and the tube. Generally, failure of the tube occurred on a line at the same orientation as the fibers in the tube, i.e., at  $\pm 15^\circ$  from the vertical axis (Figure 2.9). After removing the tube from the failed specimens, one could clearly see extensive shear cracking in the concrete. The tube did not increase the shear strength of the beams beyond their flexural strength. However, the shear strength was increased

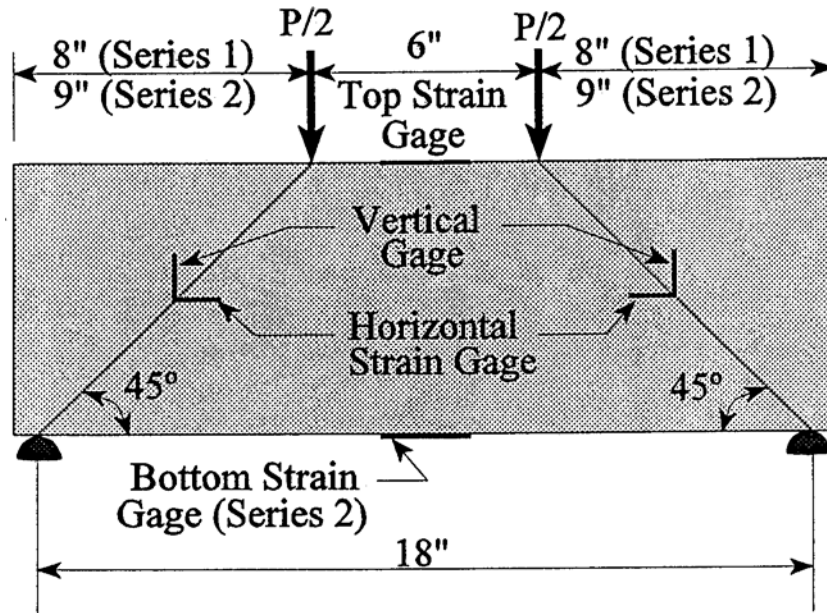


Figure 2.4 Instrumentation of beam specimens

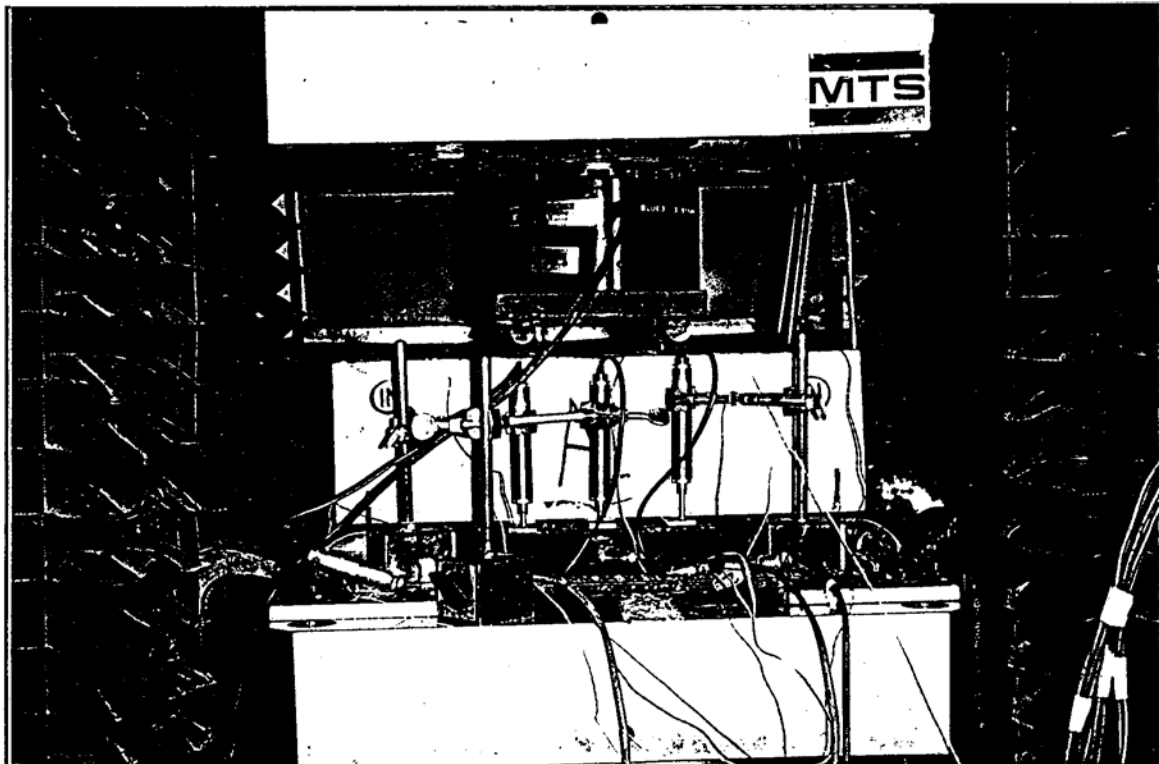


Figure 2.5 Beam shear test set up -10-

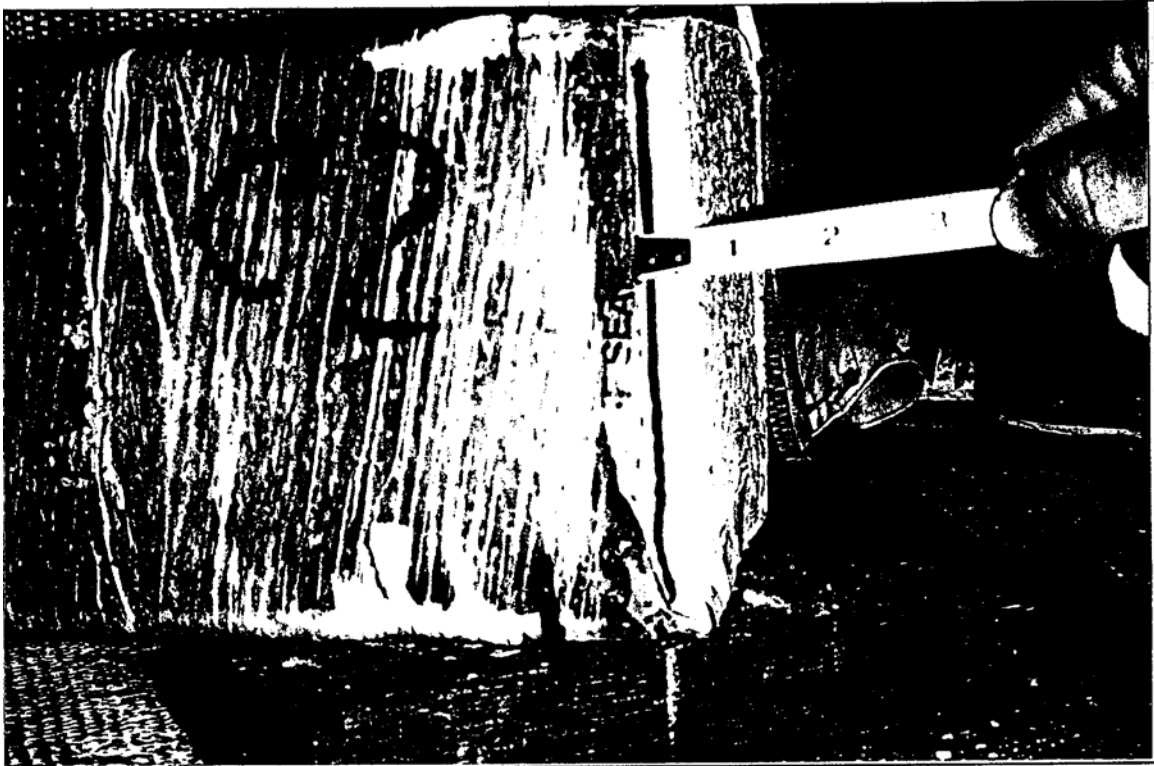


Figure 2.6 Beam C2 after failure showing extreme slippage

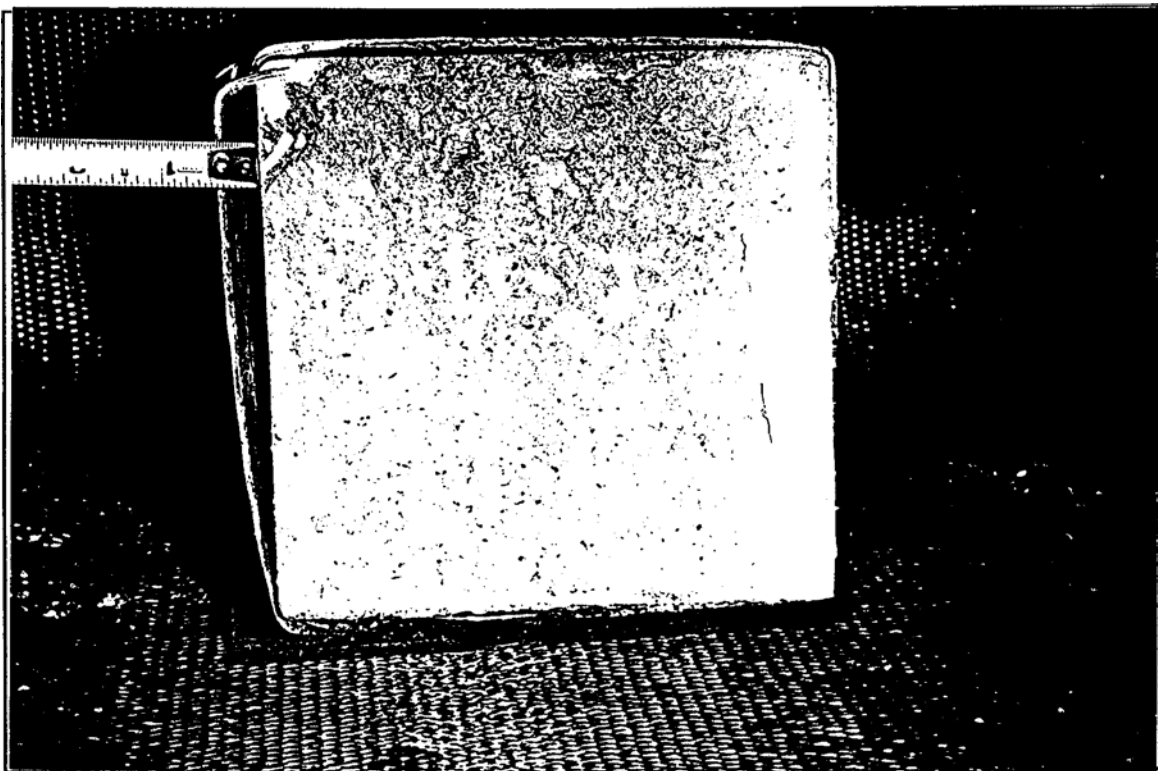


Figure 2.7 Beam C2 with bulged and separated jacket -11-

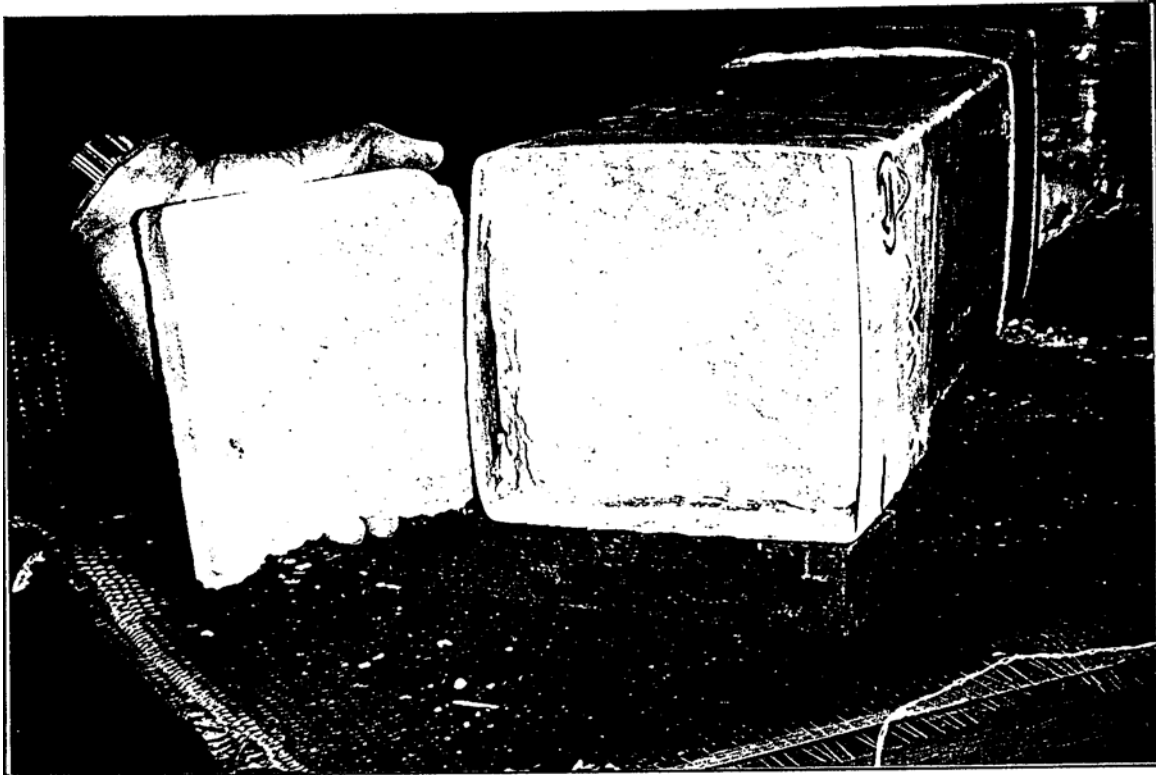


Figure 2.8 Beam C2 after failure (side view)

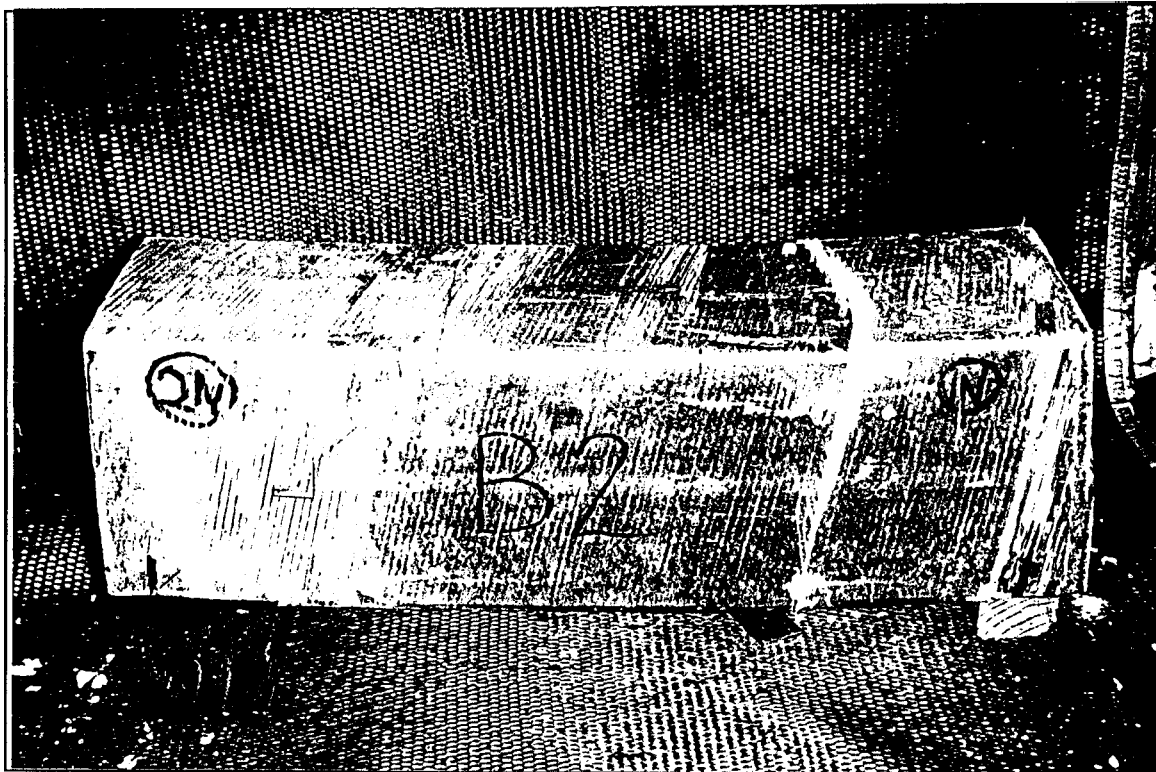


Figure 2.9 Beam B2 after failure showing crack inclination at fiber orientation -12-

considerably due to crack containment. Thus, the expected and actual failure of the control specimens was from shear. The theoretical shear strength of the jacketed specimens was calculated (from equations developed in Section 2.3 and assuming a 45° angle of crack) to be nearly double the flexural strength. Thus the failure for the jacketed specimens was expected to be flexural. However, no flexural failure was observed in any of the specimens. It is believed that the excessive amount of slippage was of great consequence to the lack of shear enhancement provided by the jacket. In order for the jacket to increase the shear strength of the beams, efficient load transfer needed to occur at the onset of the first shear crack in the concrete. However, the extensive amount of slipping indicated that very little or no transfer of load could have occurred until the concrete had completely failed. At this point, the concrete was severely damaged and large voids may have been present in the concrete. It can be seen in specimen B2 (Figure 2.10) that a chunk of the concrete broke off at the end. The jacket for that same specimen (Figure 2.11) failed along a crack near the point where the chunk of concrete broke off. At this point, concrete offered no internal support for the jacket and the jacket failed prematurely. The same was true for specimen B 1. Specimens of Group C behaved similar to those of Group B with the exception of some flexure cracking. These specimens were reinforced with a woven carbon sheet on the tension face between the concrete and the glass jacket. It was noted earlier that these specimens were the least likely to show flexural damage since they had the highest flexural strength. Upon removing the jacket from the tested beams, it was noticed that the tension face of the concrete was impressed with the weave pattern from the carbon sheet (Figure 2.12). The woven carbon sheet may have served as a mechanical bond between concrete and the tube aiding the transfer of tensile loads at the interface. Specimens of Group D behaved very similar to the control specimens. Since the jacket was provided only on three faces of the beam (no top), concrete was not confined as it was for the other specimens. It is evident from Group D that part of the enhancement in the shear strength seen for Groups B and C came from the ability of the tube to contain (rather than confine) concrete allowing it to withstand higher loads. Since the top of the jackets had been removed for specimens of Group D, the load was applied directly onto the concrete. This, and the fact that the jacket for these specimens showed no cracks, further supports the theory that no load was transferred to the jacket by concrete.

### Test Results

The strain readings from the rosettes were not consistent, possibly because the tube surface where the rosettes were placed was uneven. This unevenness made it difficult to thoroughly glue the entire rosette onto the tube surface. Therefore, the strain readings will not be included in this section. As was mentioned earlier, the control specimens were designed with a flexural strength nearly nine times their shear strength. Table 2.3 shows the increase in the shear strength for the jacketed specimens over the control specimens. Also tabulated, is a comparison of the theoretical shear strength to the experimental results. The theoretical values are calculated according to equations of Section 2.3. Having learned that in order to fully utilize the shear strength of the jacket, some bond needs to be provided between the concrete and the jacket, a second series of test was devised (Series 2) where shear connectors were provided inside the jacket.

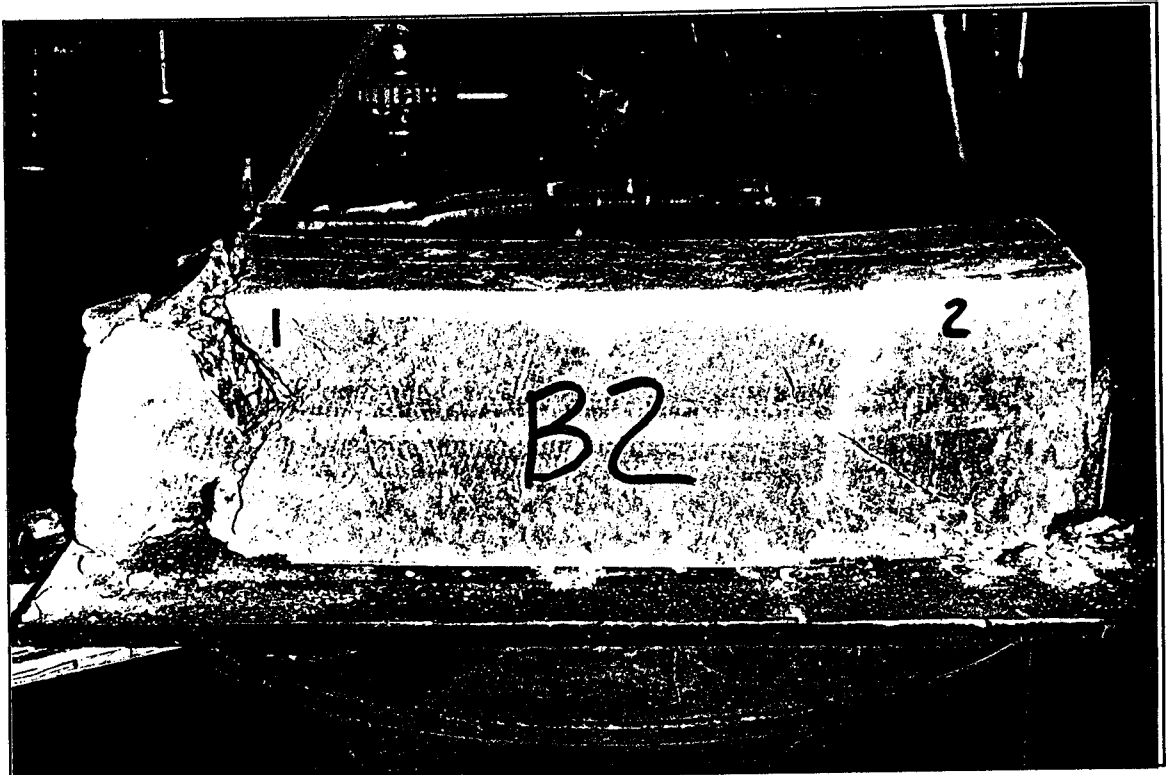


Figure 2.10 Interior of Beam B2 after failure

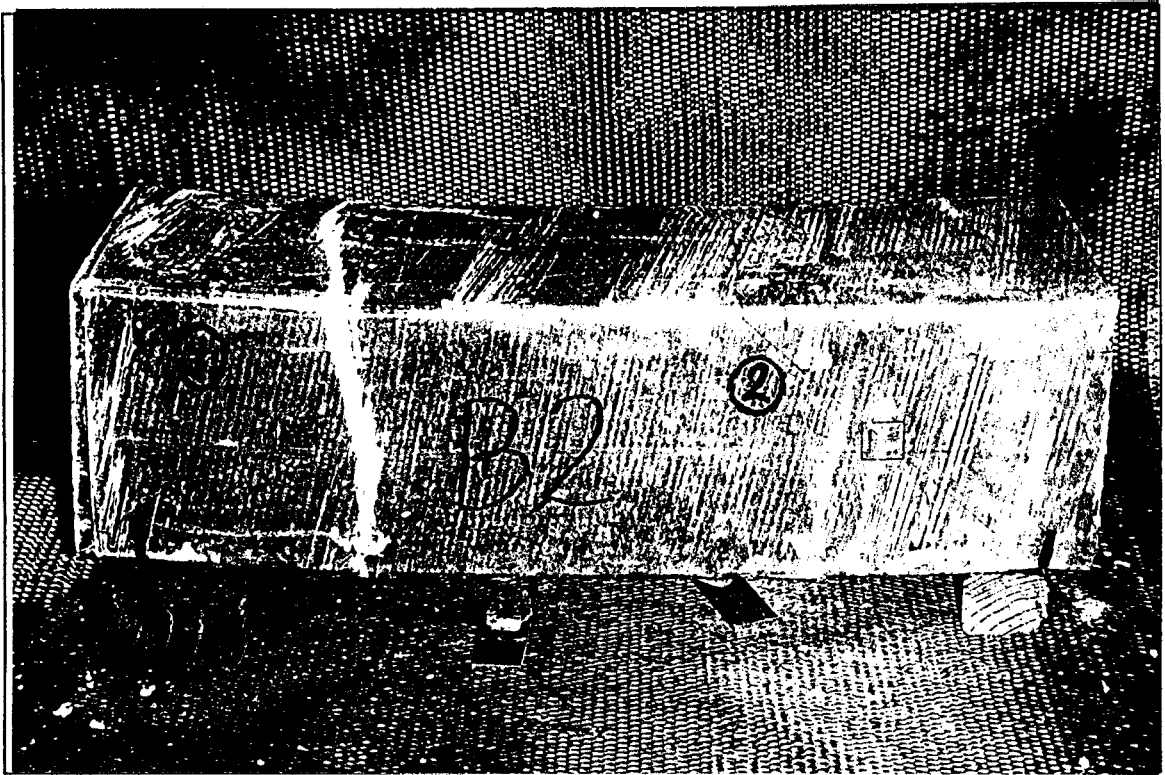


Figure 2.11 Beam B2 after failure -14-

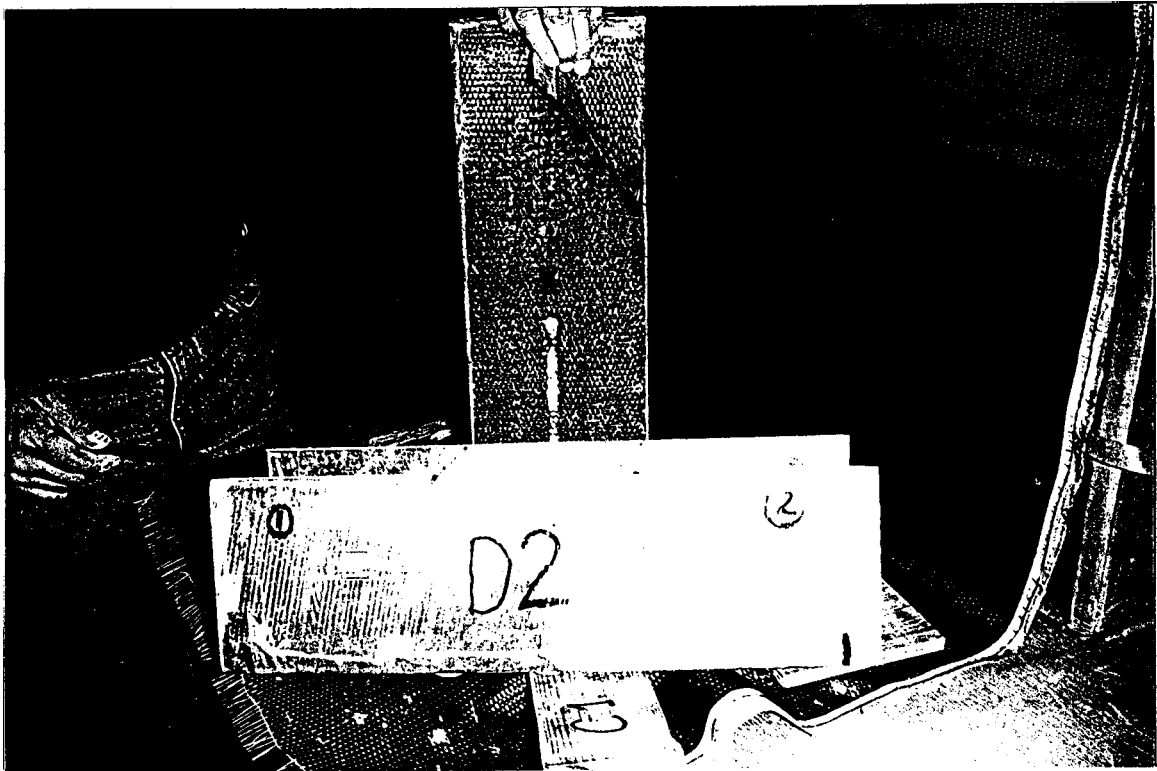


Figure 2.12 Beam D2 after failure

Table 2.3 Test results for Series 1

Specimen	Experimental $P_{max}$ (kips)	Percent increase over control beams	Theoretical $P_{max}$ (kips)	$P_{Theo}/P_{Exp}$
A1	9.96	-	4.82	0.5
A2	11.93	-	4.82	0.4
B1	20.74	89.49	62.27	3.0
B2	25.55	133.44	62.27	2.4
C1	23.74	116.90	62.27	2.6
C2	19.12	74.69	62.27	3.3
D1	14.18	29.56	62.27	4.4
D2	17.45	59.43	62.27	3.6

\* Average strength of concrete cylinders was 4.476 ksi.



## Series 2

In order to correct the slippage problem encountered with the beams of Series 1, a new type of beam was manufactured with shear connectors on all four interior faces. Series 2 beams, however are not comparable to Series 1 beams since no steel re-bars were included in these beams. A total of 8 beams were fabricated and tested for Series 2. Fabrication of the tubes and the mandrel were discussed in the Final Report of Phase I (Mirmiran 1997), and will not be repeated here. The differences between the tubes of this study and the one reported under Phase I are as follows; (1) tubes of Group H were made with 6 layers of angle plies while all other tubes and the tubes of Phase I were all made of 15 layers, and (2) no roving was used in the construct of the tube for shear tests, and only for the tubes of series G, a chopped glass fiber mat was glued after the mixture hardened and before the outside jacket was wound on.

### Specimen Layout

Table 2.4 shows the test matrix for Series 2. Eight specimens were divided into four groups with two identical samples from each group for repeatability verification. All specimens were approximately 24 inches long. Figure 2.13 shows the schematics of the specimens of each group. Four 6" x 12" concrete cylinders were also cast to determine the average strength of concrete core. The characteristics of the four groups are as follows:

1. Group E consisted of the control specimens with a glass sheet glued onto the tension side as flexural reinforcement. No other type of reinforcement was provided for the control specimens.
2. Group F specimens were reinforced with a 0.135 inch thick FRP jacket made of 15 layers of fibers. No glass sheet was provided as additional reinforcement for these specimens.
3. Group G specimens were also reinforced with a 15-layer FRP jacket. However, they differed from specimens of Group F in that a chopped glass sheet was provided as additional reinforcement on all 4 sides of the inside jacket.
4. Group H specimens consisted of a 6-layer FRP jacket with 0.054 inch thickness and no glass sheet.

**Table 2.4 Test matrix for Series 2**

Group No.	Longitudinal Reinforcement		Shear Reinforcement
	Compression	Tension	
E	None	Glass Fiber Sheet	None
F	None	None	FRP Tube [15 Layers]
G	Chopped Glass Fiber Mat on all Sides	Chopped Glass Fiber Mat on all Sides	FRP Tube [15 Layers]
H	None	None	FRP Tube [6 Layers]

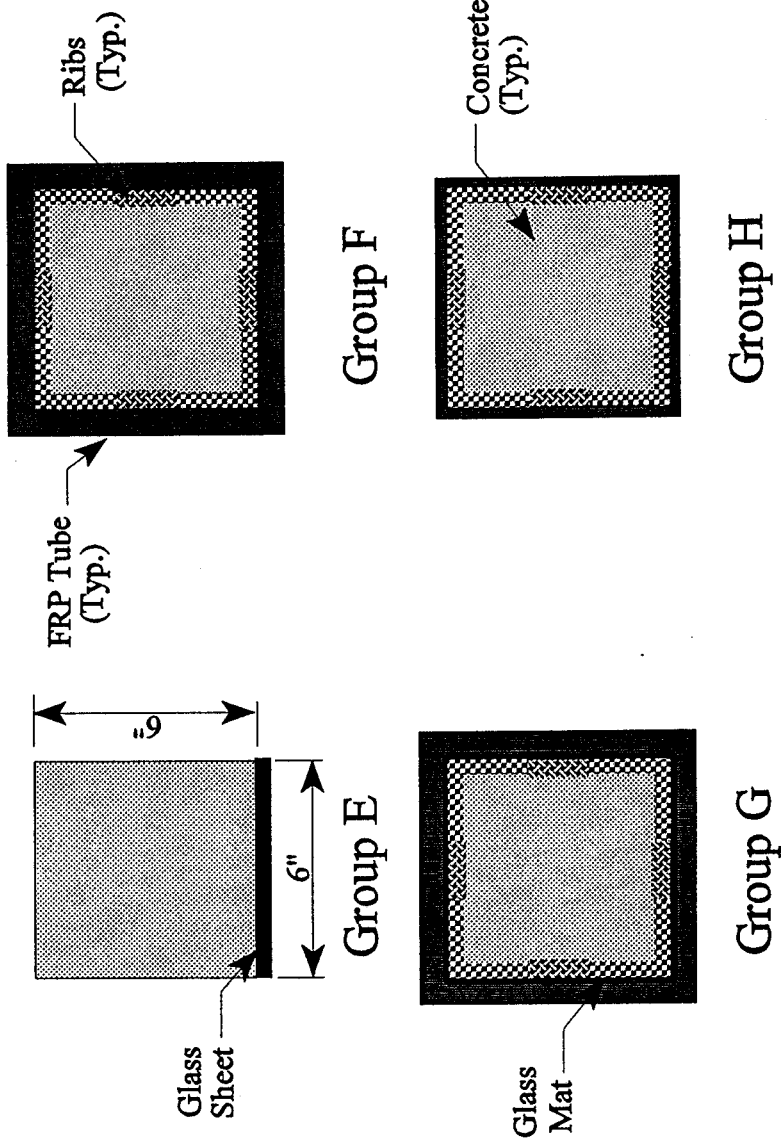


Figure 2.13 Specimen layout for Series 2

Materials were the same as those reported earlier for the specimens of Series 1, with the exception of the specific gravity of crushed limestone being 2.321. The concrete mix was designed based on a volume method with a water-to-cement ratio of 0.515 (by weight) for a 28-day compressive strength of 4000 psi. No additives were used in the mix. One cubic yard of the mix consisted of 597.7 lb cement, 308.23 lb water, 1080.87 lb sand, and 1804.15 lb gravel. Casting was done at UCF on July 1, 1996, using a 9-cubic foot rental mixer. Concrete was compacted using an electric vibrator. Other preparation tasks were the same as for Series 1.

### Instrumentation

For beams E2, F2, G2, and H2, rosettes were attached at both vertical faces on the center of a 45° line between the support and the load. The rosettes measured horizontal, vertical and the strain along the 45 ° line (see again Figure 2.4). For all the beams, strain gages were also placed centered vertically and horizontally on the top and bottom faces. The beams were also instrumented with three LVDTs one at the mid-span, and two under the points of load application.

### Test Procedure

Specimens were tested on July 31 and August 1, 1996 at the Florida Department of Transportation. Test set up and equipments were the same as for Series 1.

### Observed Behavior

As with Series 1, cracking and popping noise was heard while testing the FRP beams. Although a glass sheet was provided as reinforcement against bending and no shear reinforcement was provided, the control specimens did not fail in shear. The reason for this is that the glass fiber sheet glued to the tension face of the beams de-bonded while loading as can be seen in Figure 2.14. It was later noted that in order to prevent bond failure, it is necessary to sandblast the face of concrete and extend the glass sheet about 2 inches up the front and back face of the beam. However, the objective of Series 2 was to prevent the slippage between the concrete and the FRP jacket, and this was clearly accomplished. Beams F1, H1, and H2 failed in flexure at the midspan. Beams G1, G2, and F2 failed from excessive flexural cracks which developed under the point of load application. It should be noted that the jackets for the specimens contained some unevenness. It is suspected that the unevenness of the jacket surface for these beams prohibited even distribution of the load at both points resulting in the extreme cracking and eventual failure under the loading point (Figure 2.15). No slippage was evident for any of the beams. As a result, flexural cracking was clearly visible in most of the specimens (again see Figure 2.15). Upon removal of the jackets, there was no evidence of the extensive shear cracking present in the concrete as with the specimens for Series 1. The shear connectors had effectively retarded slippage and allowed for the concrete and the jacket to act effectively as one composite section.

### Test Result

Since none of the beams failed in shear, it was not possible to make a quantitative comparison of the increase in shear strength provided by the jacket. Therefore, the theoretical values from Section 2.3 clearly overestimate the failure load of the specimens since they all failed in flexure. Table 2.5 presents the percent increase in the load carrying capacity of the beams. Because



Figure 2.14 Control Beam E1 after failure



Figure 2.15 Beam G2 after failure -19-

none of the jacketed beams failed in shear, it is known that the shear strength of the jacketed beams was greater than the load at failure. Since the load at failure was anywhere between 2 and 6 times the strength for unjacketed specimens as given by ACI, we may conclude that the jacket enhanced the shear strength by more than 2 to 6 times the theoretical shear strength of unjacketed beams.

**Table 2.5 Test results for Series 2**

Specimen	Experimental $P_{max}$ (kips)	Percent increase over control beams	Theoretical $P_{max}$ (kips)	$P_{Theor}/P_{Exp}$
E1	4.54	-	4.95	1.1
E2	4.11	-	4.95	1.2
F1	27.55	537	155.61	5.6
F2	19.85	359	155.61	7.8
G1	10.64	146	155.61	14.6
G2	10.80	150	155.61	14.4
H1	24.68	471	54.20	6.3
H2	24.32	462	54.20	6.4

\* Average strength of concrete cylinders was 4.722 ksi.

Graphs of load versus top and bottom strains are also provided for these specimens (Figures 2.16 and 2.17). Also, Figure 2.18 shows the moment-curvature for all specimens. The curvature is calculated by dividing the algebraic difference between the top and bottom strains by the depth of the section (6"). The latter graph shows considerable ductility for jacketed specimens. It can be seen in all three graphs that the strain and load capacity for all jacketed beams are considerably increased. The beams which clearly failed in flexure at midspan show the greatest increase. It is also of interest to note that the jacketed specimens exhibit the same behavior as the unjacketed specimens up to the point where the plain concrete fails. From this point on, a clear change in the slope occurs. All jacketed beams except G2 show the same second slope in the load-strain curve. No such behavior was evident for Series 1. As with Series 1, however, the unevenness of the jacket combined with the relatively short length of the rosettes is suspected responsible for the inconsistent strain readings from the rosettes. For this reason, no charts of these readings are provided here. It is apparent from the results from Series 2 that the shear connectors successfully corrected the slippage problem encountered in Series 1. With slippage no longer a problem, the jacket acted effectively to increase the shear strength of the beams. However, fabrication of the square jackets needs to be improved to ensure a smooth, level surface.

### 2.3 Analysis and Discussion

Because of the sudden and often catastrophic nature of shear failures, it is necessary to develop a way of adequately predicting the shear strength of FRP-encased beams. In this section,

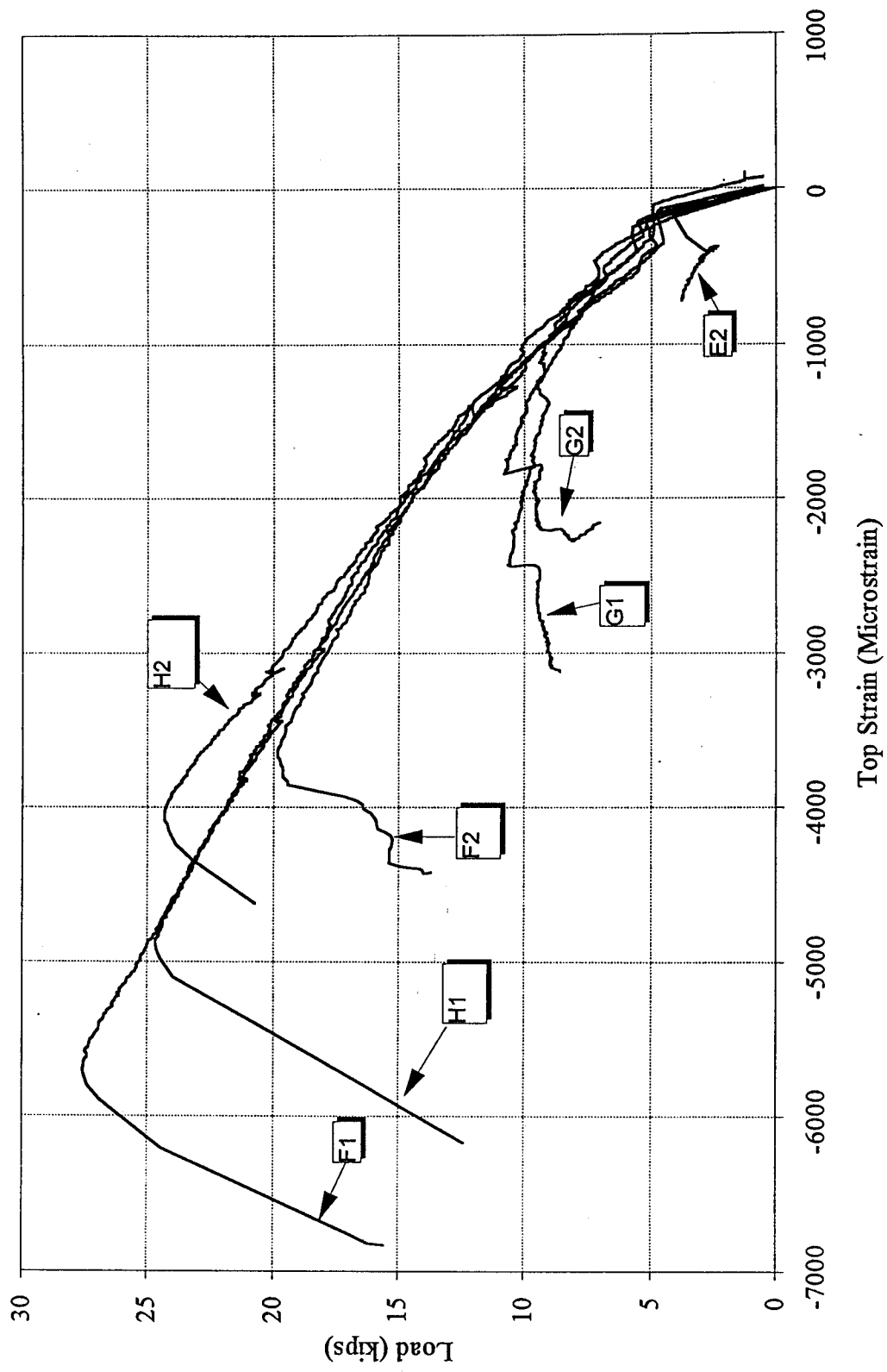


Figure 2.16 Load versus top strain for specimens of Series 2

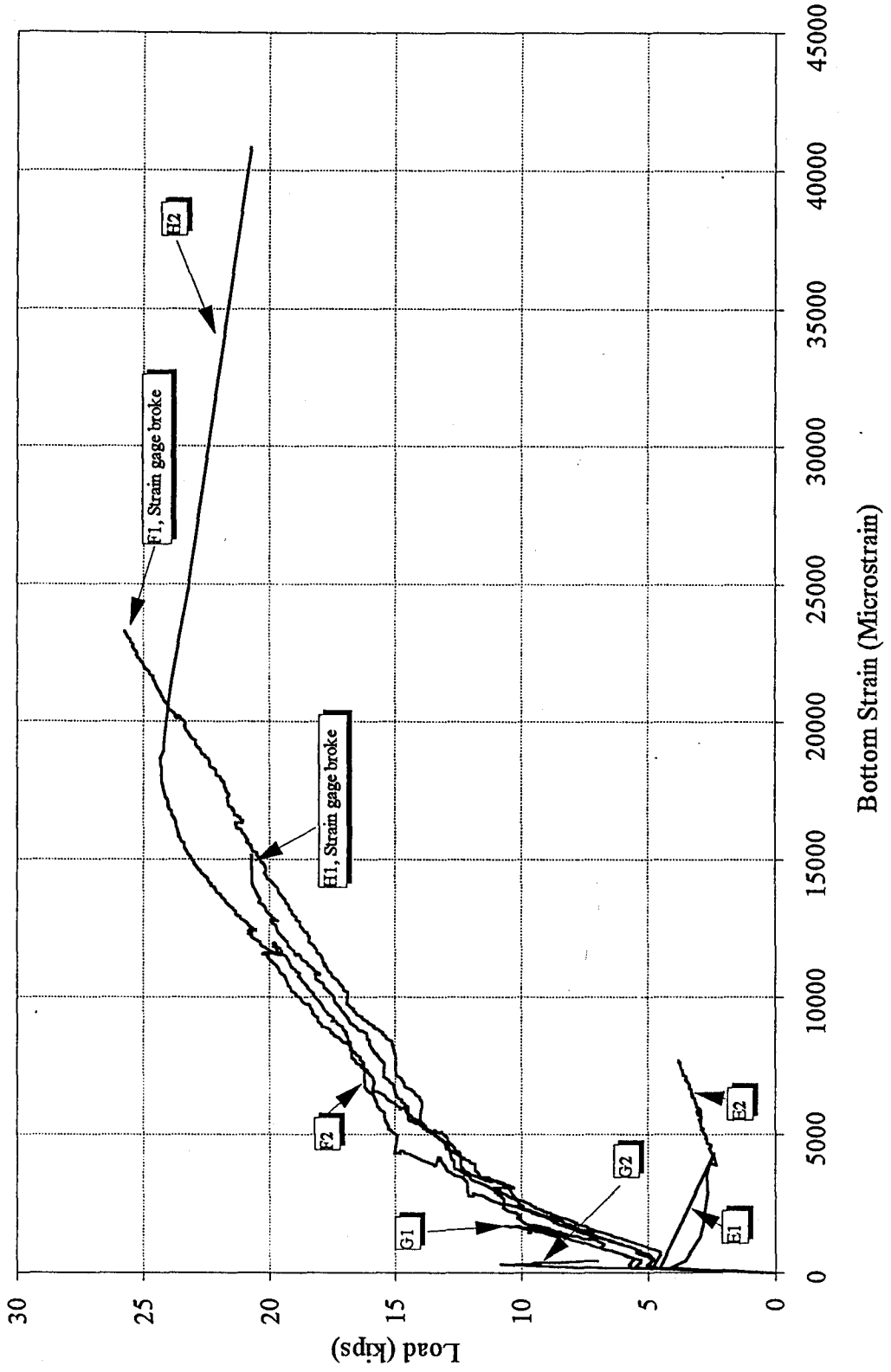


Figure 2.17 Load versus bottom strain for specimens of Series 2 .

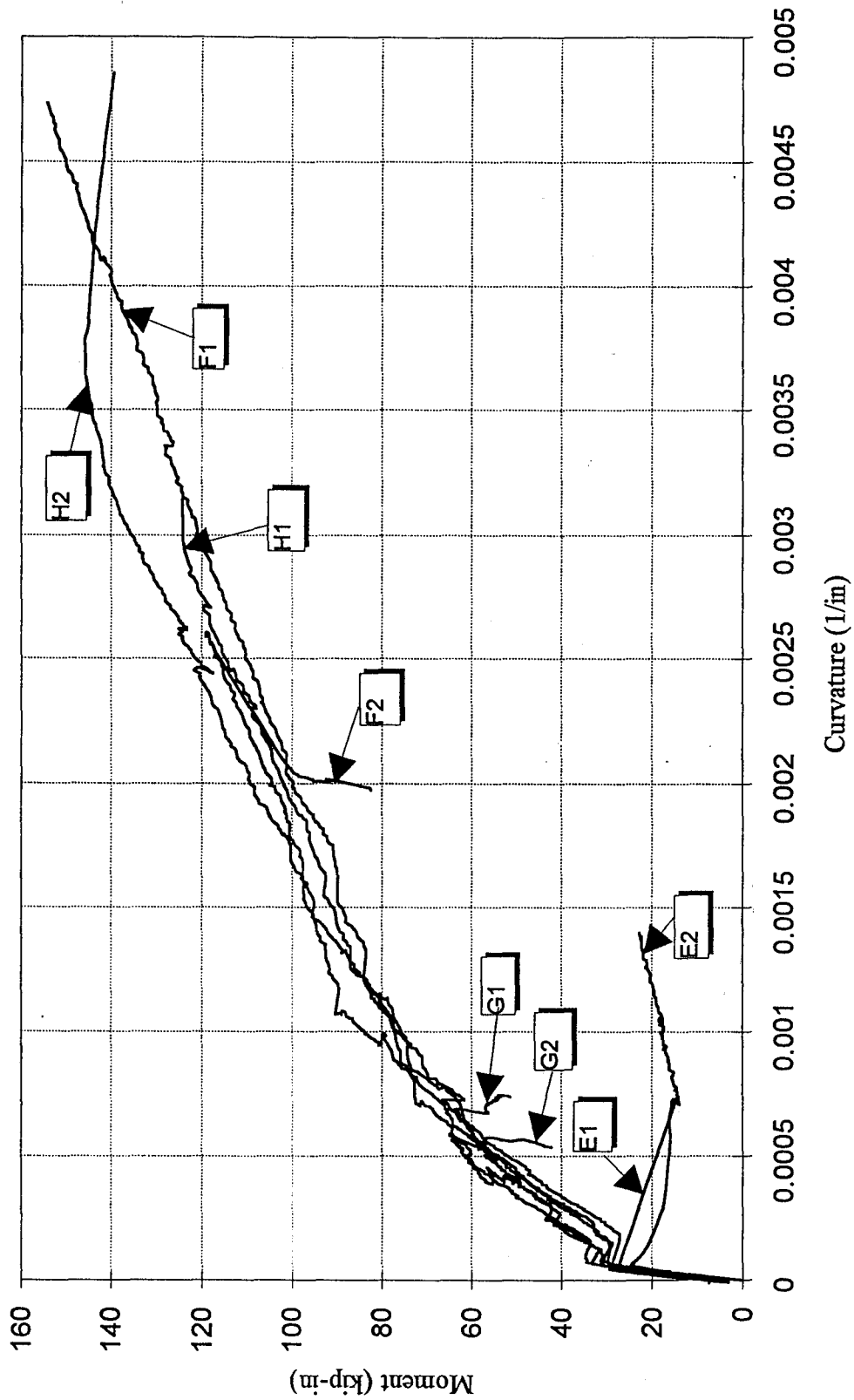


Figure 2.18 Moment-curvature for specimens of Series 2



shear strength of FRP-encased concrete beams will be discussed. The truss analogy will be used to establish the shear strength formulas. The theoretical study concentrated on members of both rectangular and circular cross sections, even though experimental work was only conducted of square sections. The underlying assumption in the derivations of shear strength is the full bond between the tube and the concrete core, and the shear failure of the cross section.

### Rectangular Sections

In order to aid in developing the equation for the shear strength provided by the FRP jacket, first, the simplest case was undertaken. That is, it was assumed that the fibers in the jacket were oriented only in the vertical direction. When concrete cracks, the crack traverses a distance  $c$  along the jacket. Figure 2.19 is an illustration of the cracked beam and the forces developed in the jacket.

The forces in the jacket exposed by the crack are given by

$$V_f = f A_f \quad (2.1)$$

where  $f_f$  is the strength of the jacket. Let  $p$  be the horizontal projection of the crack, and  $t_f$  the thickness of the jacket, the jacket area traversed by the crack will then be

$$A_f = 2 p t_f \quad (2.2)$$

Substituting the above equation in Equation (2.1),  $V_f$  becomes:

$$V_f = 2 f_f p t_f \quad (2.3)$$

Let  $d$  be the depth of the beam, and  $\theta$  the angle that the crack makes with the horizontal axis, the crack length in terms of the beam depth will then be

$$p = \frac{d}{\tan \theta} \quad (2.4)$$

and the expression for the maximum force in the jacket in its final form becomes

$$V_f = \frac{2 f_f t_f d}{\tan \theta} \quad (2.5)$$

The case of vertical fibers is only a special case of the more general equation for inclined fibers (fiber inclination =  $0^\circ$ ). Letting  $\phi$  denote the fiber inclination, the fibers are equally oriented at  $\pm\phi$  from the vertical axis. Figure 2.20 shows the forces developed in the jacket. The vertical component of the force exposed by the crack is

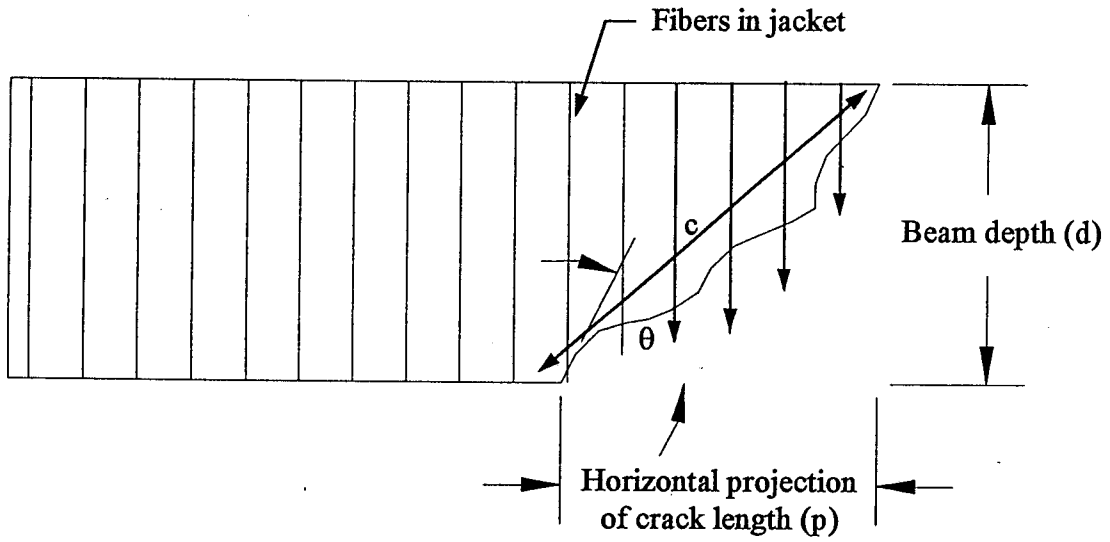


Figure 2.19 Shear crack in a rectangular FRP beam with only hoop fibers

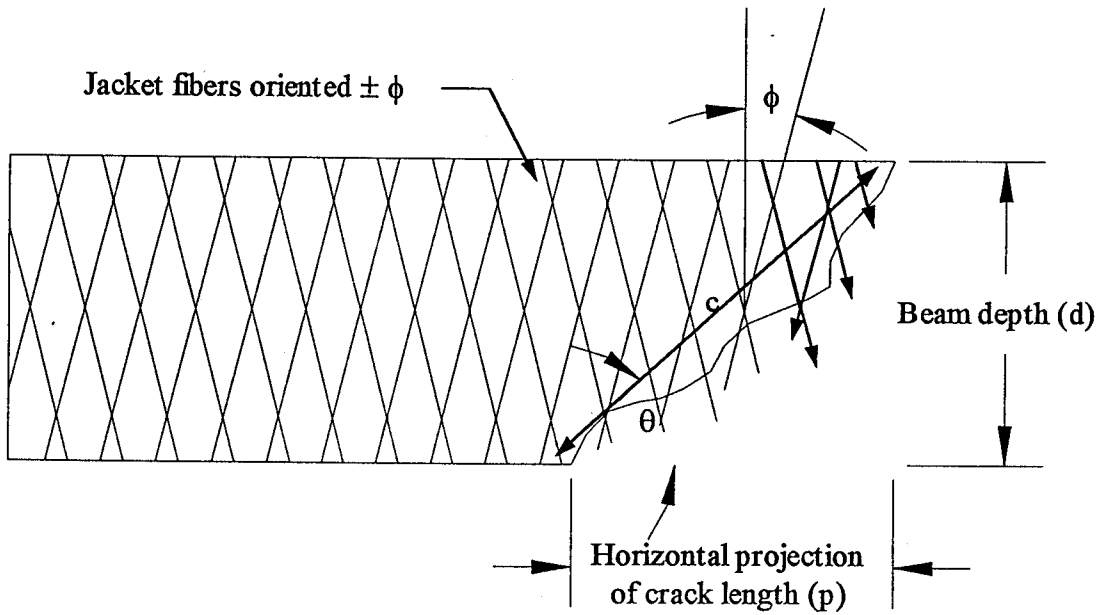


Figure 2.20 Shear crack in a rectangular FRP beam with  $\pm \phi$  angle plies

$$V_f = f_f A_j \cos \theta \quad (2.6)$$

Substituting Equation (2.2) in Equation (2.6) and relating the crack length to the dimensions of the beam, the equation for the maximum force that can be taken by the jacket becomes

$$V_f = \frac{2f_f t_f d}{\tan \theta} \cos \phi \quad (2.7)$$

which is the general expression for the shear strength provided by the jacket in a rectangular cross section.

### Circular Sections

Developing the shear strength provided by the jacket for a circular cross section requires a somewhat different approach. Chai (1991) addressed the shear strength of circular retrofitted columns with steel jackets. The same approach is taken here with slight modification to account for the possibility of fiber inclination within the jacket. Figure 2.21 shows the forces exposed by the shear failure plane. The fibers in the jacket are equally inclined at  $\pm\phi$  from horizontal and  $\alpha$  is the angle that the shear failure plane makes with the vertical axis. For an infinitesimal jacket height,  $dz$ , the shear force resisted by the jacket is

$$dV_f = 2 f_f t_f \cos \phi \sin \alpha dz \quad (2.8)$$

where  $\cos \phi$  represents the horizontal component of the fibers in the jacket. The total shear force would then be given by

$$\int dV_f = \int 2 f_f t_f \cos \phi \sin \alpha dz \quad (2.9)$$

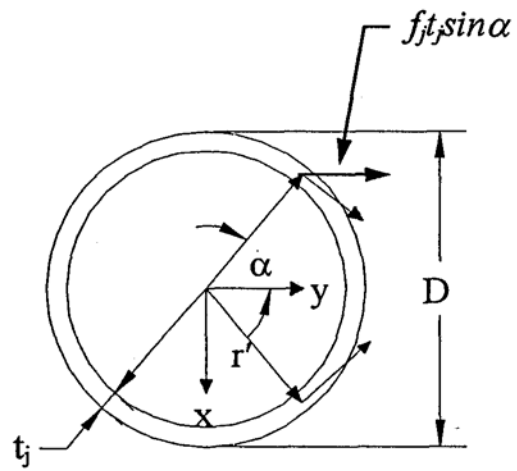
In order to solve the equation, a relationship between  $dz$  and the angle  $\alpha$  is needed, as below

$$y = r' \cos \alpha \quad (2.10)$$

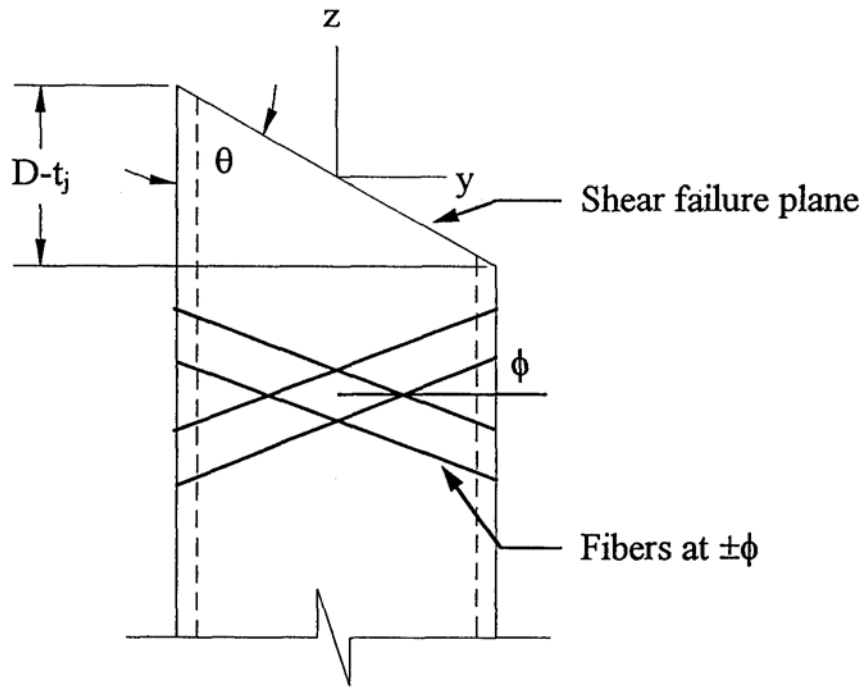
$$y = -z \tan \theta$$

$z$  may be expressed as

$$z = \frac{r' \sin \alpha}{\tan \theta} d\alpha \quad (2.11)$$



Plan



Elevation

Figure 2.21 Shear crack in a circular FRP beam with  $\pm \phi$  angle plies

from which

$$dz = \frac{r' \sin \alpha}{\tan \theta} d\alpha \quad (2.12)$$

which is the desired relationship. Substituting Equation (2.12) into Equation (2.10), the equation for the shear force becomes

$$V_f = \frac{2 f_f t_f r' \cos \phi}{\tan \theta} \int_0^{\theta} \sin^2 \alpha d\alpha \quad (2.13)$$

Noting that and evaluating the integral, the final expression for the shear strength of the jacket is arrived at and is given by

$$V_f = \frac{2 f_f t_f r' \cos \phi}{\tan \theta} \int_0^{\theta} \sin^2 \alpha d\alpha \quad (2.14)$$

This equation is the most general case allowing for any fiber inclination and any crack angle.

### Shear Strength of Concrete

The shear strength of the concrete core would also contribute to the total shear strength of the member. According to ACI 318-95 (1995), the shear strength provided by concrete is  $2\sqrt{f_c} b d$  where  $b$  is the width and  $d$  is the depth of the member and  $f_c$  is the 28 day compressive strength of concrete. The total shear strength of the member, as provided by the FRP jacket and the concrete is then given by

$$V = V_f + V_c \quad (2.15)$$

where  $V_j$  is the jacket strength and  $V_c$  is the concrete strength.

Although the strength of the jacket is expected to considerably increase the shear strength of the members, the confinement provided by the jacket also enhances the shear strength of the member. At the first onset of a crack in the concrete, the load would be transferred to the jacket. The jacket would retard any further increase in the width of the crack since the concrete would have nowhere to move to (assuming no slip). An unconfined beam would not be as efficient in crack containment. The narrower cracks would allow for a greater interface force, hence, further increasing the shear strength of the beam.

from which

$$dz = \frac{r' \sin \alpha}{\tan \theta} d\alpha \quad (2.12)$$

which is the desired relationship. Substituting Equation (2.12) into Equation (2.10), the equation for the shear force becomes

$$V_f = \frac{2f_f t_f r' \cos \phi}{\tan \theta} \int_0^{\theta} \sin^2 \alpha d\alpha \quad (2.13)$$

Noting that  $r' = \frac{D - t_j}{2}$  and evaluating the integral, the final expression for the shear strength of the jacket is arrived at and is given by

$$V_f = \frac{2f_f t_f (D - t_j) \cos \phi}{2 \tan \theta} \quad (2.14)$$

This equation is the most general case allowing for any fiber inclination and any crack angle.

### Shear Strength of Concrete

The shear strength of the concrete core would also contribute to the total shear strength of the member. According to ACI 318-95 (1995), the shear strength provided by concrete is  $2Jf_c \sim bd$  where  $b$  is the width and  $d$  is the depth of the member and  $f_c$  is the 28 day compressive strength of concrete. The total shear strength of the member, as provided by the FRP jacket and the concrete is then given by

$$V = V_j + V_c \quad (2.15)$$

where  $V_j$  is the jacket strength and  $V_c$  is the concrete strength.

Although the strength of the jacket is expected to considerably increase the shear strength of the members, the confinement provided by the jacket also enhances the shear strength of the member. At the first onset of a crack in the concrete, the load would be transferred to the jacket. The jacket would retard any further increase in the width of the crack since the concrete would have nowhere to move to (assuming no slip). An unconfined beam would not be as efficient in crack containment. The narrower cracks would allow for a greater interface force, hence, further increasing the shear strength of the beam

## CHAPTER 3

### EFFECT OF CROSS SECTION ON CONFINEMENT

#### 3.1 Literature Review

It is well known that lateral confinement of concrete increases its strength and ductility. In conventionally reinforced concrete columns, confinement is provided by transverse steel stirrups or hoops. Generally, building codes such as ACI 318-95 (1995) specify the spacing and bar size requirements for the transverse steel to allow for ductile failure of the columns under overload conditions. Another method of confining concrete is by encasing concrete in a steel tube. Concrete filled steel tubes have in recent years attracted a growing interest in the construction industry. As a result, researchers too have investigated several aspects of their performance. Ge and Usami (1996) evaluated the inelastic behavior of concrete-filled steel box columns under cyclic loading. IEjjar and Gourley (1996) developed a polynomial strength equation to represent the moment-thrust interaction diagram of concrete-filled steel tubes. Lu and Kennedy (1994) determined that concrete-filled steel tubes increased the flexural strength of hollow steel tubes by up to 30%. Prion and Boehme (1994) showed that confinement effectiveness of the tube is greatest for slenderness ratios of less than 15.

Confining of concrete columns is also advantageous for strengthening of existing columns. One such method was developed by researchers at the University of California, San Diego for the California Department of Transportation (Caltrans). In this technique two half cylinders of steel are placed around the existing column, and then welded together. The gap between the jacket and the existing column is filled by grout. Priestley et al. (1994) have shown that steel jacketing not only improves flexural strength of the column but also increases the shear capacity somewhat similar to transverse steel ties.

Another method of confinement that has been developed during the last ten years is fiber wrapping. The wrapping of unidirectional fiber composite sheets around concrete columns offers a promising technique to strengthen and repair existing bridge structures. Demers and Neale (1994) tested several circular and square specimens with fiber-wrapping made of glass or carbon fibers. They concluded that increases in strength of up to 70% are possible and that the ultimate failure strain can be of the order of seven times that of a plain concrete specimen. Extensive studies at the University of Sherbrooke have shown that circular sections are more effectively confined than rectangular sections (Picher 1995, Rochette 1997). For rectangular sections, it is the corner radius that controls the confinement effectiveness. As the corner radius increases, the behavior of the column becomes closer to a circular column confined by fiber composites.

For the last three years, the Florida Department of Transportation has sponsored a detailed investigation of concrete-filled FRP tubes with a special design. Pilot tests by Kargahi (1995) showed the feasibility of the proposed method. Scherer (1996) extended the experimental studies and developed a framework for modeling of concrete confined by fiber composites. He also studied the optimization of the tube thickness and concrete section. Cabrera (1996) studied the shear strength and seismic performance of the hybrid system. Samaan et al. (1997) developed a confinement model for circular FRP tubes. Collective studies of the last three years at UCF have proved the advantages of the proposed system as follows:

1. High strength-to-weight ratio of fiber composites reduces the necessary thickness of the tube and results in lighter and more slender sections.
2. Poisson ratio of fiber composites is more compatible with concrete as compared with steel tubes.
3. Anisotropic properties of fiber composites allow for uncoupling of the design in the axial and hoop directions.
4. Fiber composites can effectively contain the dilation tendency of concrete. This is mainly due to the linear-elastic response of fiber composites. Also, this is in contrast to the behavior of steel-encased concrete columns in which, upon yielding of steel, dilation of the concrete core becomes unstable.

Despite advances in the use of fiber composites in hybrid construction with concrete, theoretical work has often been limited to simple extension of the models developed for steel and concrete composite systems. Of great importance in concrete-filled tubes is the accurate prediction of the strength and ductility of the column as the result of confinement. The first to propose a model for confinement was Richart et al.(1929) who suggested a relation in the following form

$$f_{cc}^t - f_{co}^t = 4.1 f_r \quad (3.1)$$

where  $f_{cc}^t$  is the maximum stress of confined concrete,  $f_{co}^t$  is the peak stress of unconfined concrete, and  $f_r$  is the confining pressure.

The many models that followed the above work have all been developed for confinement with transverse steel. However, most have been applied to steel tubes, steel jackets, and even fiber wrapped columns. Perhaps one of the most known models is the one developed by Mander et al.(1988). Recent studies by Mirmiran and Shahawy (1997) and Demers and Neale (1994) have shown that Mander's model overestimates the strength while underestimating the ductility of FRP-encased concrete. Specifics of the problems associated with Mander's model as related to fiber composites have been elaborated by Kargahi (1995), Scherer (1996), and Harmon and Wang (1996). The latter indicated that since Mander's energy-balance technique only uses the strain energy of the steel



confinement to compute the internal energy and neglects the energy stored in the concrete as a simplifying assumption, it fails to predict the behavior of FRP-encased concrete where the energy of fiber composites may account for only one fifth of the total strain energy with concrete accounting for the remaining 80%. Therefore, the strain energy of the concrete core can not be neglected.

The only model specifically developed for fiber composites is that of Fardis and Ehalih (1981) which uses Equation (3.1) for estimating the maximum stress  $f_c$  of confined concrete. The failure strain is given by

$$\epsilon_{cu} = 0.002 + \frac{0.0005 f_r}{\epsilon_{ru} f'_{co}} \quad (3.2)$$

where  $E_s$  is the ultimate strain of fiber composites in the hoop direction. They further suggest a hyperbolic relation for the stress-strain response of FRP-encased concrete as follows

$$f_c = \frac{E_c \epsilon_c}{1 + \epsilon_c \left( \frac{E_c}{f'_{cu}} - \frac{1}{\epsilon_{cu}} \right)} \quad (3.3)$$

where  $\epsilon_c$  and  $f_c$  are the strain and stress in confined concrete, and  $E_c$  is the modulus of elasticity of unconfined concrete. Experimental studies by Demers and Neale (1994), however, showed that this model underestimates the ductility of the column. Moreover, it is not applicable for square sections. Most recently, Samaan, Mirmiran and Shahawy (1997) developed a simple, yet accurate, mathematical model to predict the stress-strain response of cylindrical FRP-encased concrete both in the axial and lateral directions. In this chapter, an attempt will be made to extend the model to square cross sections.

### 3.2 Experimental Work

In order to investigate the effect of cross-section on the confining behavior of FRP tubes, a series of tests was carried out on a total of fifteen specimens, including nine 6"x6"x12" concrete-filled square FRP tubes, three control cylinders (unconfined) with 6" diameter and 12" height, and three 6"x6"x12" control squares (unconfined). Three groups of tubes with jacket thicknesses of 6, 10, and 14 plies (layers) were used. For each group, three specimens of the same thickness were prepared for repeatability verification. Each specimen was labeled with SQ for square or CYL for cylinder, number of plies (6, 10, or 14, and 0 for controls), and sample number (A, B, or C). For example, SQ6B is a 6-ply square tube. All specimens were made of the same concrete batch with a target strength of 4000 psi Table 3.1 presents the test matrix. All tubes had a 1/4-inch corner radius. Also, unlike the square columns tested under Phase I, these tubes had a smooth inside edge with no shear ribs. FRP square tubes were made of the same resin and fibers as described in Chapter 2. Also, the aggregates and cement were the same as those described for Series 1 in Chapter 2.

Table 3.1 Test matrix \*

Group and Specimen No.	Cross Section	Type of Specimens	No. of Layers	Tube Thickness	Size of Specimens	Number of Samples
SQ6A, B, C	Square	Composite	6	0.083"	6" x 6" x 12"	3
SQ10A, B, C	Square	Composite	10	0.1248"	6" x 6" x 12"	3
SQ14A, B, C	Square	Composite	14	0.1617"	6" x 6" x 12"	3
SQ0A, B, C	Square	Control	-	-	6" x 6" x 12"	3
CYL0A, B, C	Circular	Control	-	-	6" (Dia.) x 12"	3

\* Design strength for concrete core was 4,000 psi.

In order to make the square FRP tubes, a collapsible mandrel was designed with aluminum angles. Four (4) aluminum angles of  $2\frac{1}{2}$ " x  $2\frac{1}{2}$ " x  $\frac{3}{8}$ " were connected with two end plates and an intermediate interior support plate, and placed on a 1-inch diameter driving shaft. There was a  $\frac{1}{2}$ " gap between the angles that was covered with masking tape. The mandrel was constructed at the UCF machine shop. However, the filament-winding process was performed at Marine Muffler Corp., Apopka, Florida. A winding angle of  $+15^\circ$  was maintained for all specimens to match the winding angles of the circular tubes. For more details, regarding the mandrel, see Final Report of Phase I (Mirmiran 1997). It should be noted that since no internal shear ribs were desired, all wooden plates were removed from the mandrel prior to the filament winding process.

The bottom of each tube was sealed with nylon to contain the concrete mix. The square control specimens were prepared using metal molds, with a wooden divider to allow for a 6" x 6" x 12" casting area. A concrete mix of 4000 psi with a 5 inch slump was designed using the volume method for a 28-day curing period. The quantities of materials per cubic yard of the mix were as follows: 610.48 lb cement, 315.51 lb water, 1055.66 lb sand, and 1800.22 lb gravel. The water cement ratio by weight was 0.517. No additive was used in the preparation of concrete specimens. The casting of all specimens was performed using a 9 cubic feet capacity rental mixer at UCF on September 5, 1996.

The top surface of each specimen was wetted daily for 5 days, to avoid any cracking of the exposed surface of concrete. Seven days after casting, the specimens were taken indoors. A  $\frac{3}{16}$ " thick groove was cut from each FRP specimen around its perimeter. This groove was cut at the top and bottom of each specimen,  $\frac{3}{4}$ " from each end. This was done to ensure that the FRP jacket acted only as confinement for the concrete core. Figure 3.1 shows the grooving process with an electric sander. To attain a purely uniaxial load and even stress distribution, all specimens were capped with sulfur mortar. A hand-made capping device was used for square sections, as can be seen in Figure 3.2. Nonetheless, the capping process is the same as the one for cylindrical specimens. The alignment guides ensure verticality of the specimen with respect to its both end surfaces.

### Instrumentation

A total of 8 PL-60 strain gages were attached to each tube, a vertical and a horizontal gage on each side of the tube at its mid-height. The surface where the gages would be placed on was first

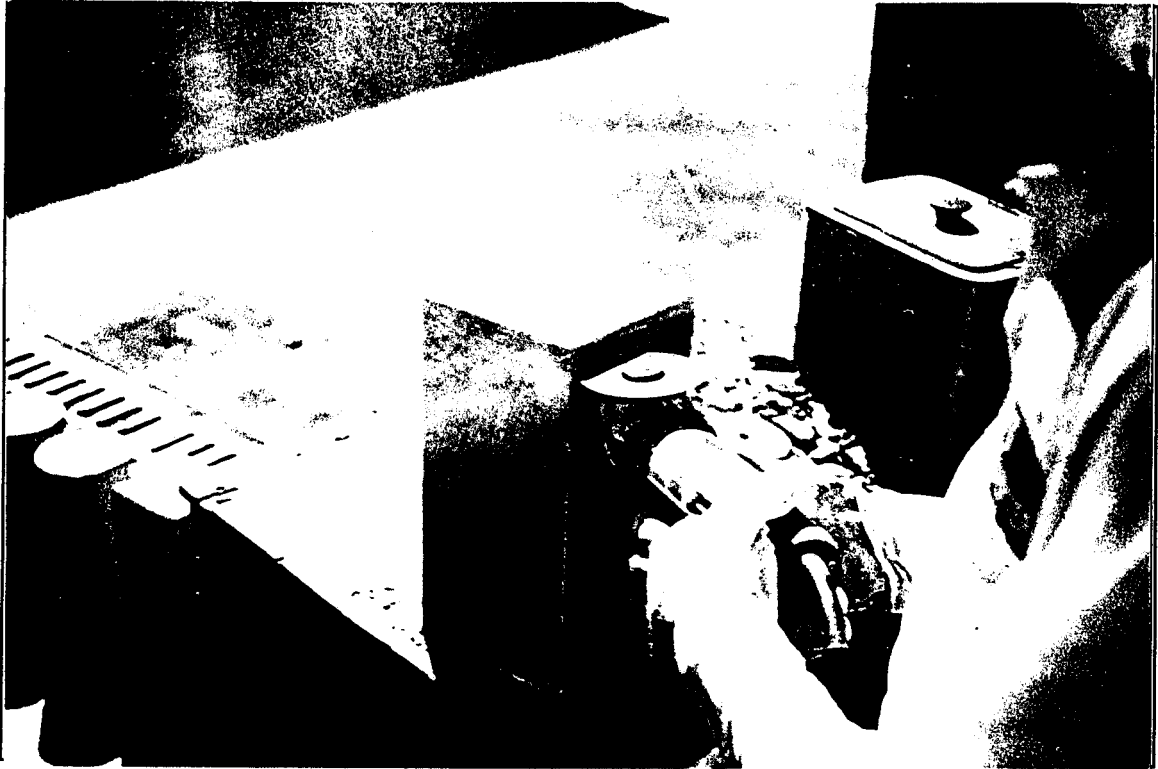


Figure 3.1 Grooving of the square tubes



Figure 3.2 Capping device for square sections

sanded and cleaned with acetone. Then, Super Glue™ was applied onto the surface and the gage oriented in the vertical (axial) direction was pressed against the glued surface. The gage oriented in the horizontal (hoop) direction was then glued on top of the axial gage. The control specimens were not instrumented with any strain gages. In addition to the strain gages, four LVDTs were used, one opposite each side of the specimen. Only three LVDTs were used for cylindrical control specimens. Figure 3.3, shows a specimen with full instrumentation prior to loading.

### **Test Procedure**

Testing of the specimens was conducted at the MOT Structural Research Lab on October 16, 1996, at the age of 41 days. Tests were performed using an MTS machine with a 550-kip capacity, and were recorded with a MegaDAQ data acquisition system (Figure 3.3). Each specimen was loaded at a constant rate of 0.22 inch per minute in a displacement control mode.

### **Observed Behavior**

As predicted, control specimens (both square and circular) failed in a shear cone mode. However, composite specimens failed in a different mode. On these, the four vertical edges began to turn white at about 50%-60% of the ultimate load. The white patches began to appear at the midheight, and then slowly spread along the entire edge, as can be seen in Figure 3.4. This was due to the plastic flow of the resin, leaving the fiberglass strands to resist the load. Then, low cracking sounds would be heard, at which point the load significantly dropped, but then stabilized. Some of the specimens hardly showed any visible signs of significant distress during loading. The only warning these delivered were the white patches and the low cracking noises, followed immediately by failure. The first composite specimen that was tested was SQ6C. It was noted that the specimen failed at a load not much higher than the failure load of the unconfined square specimens. The specimen failed very quietly, and remained intact, except for some white patches at the edges. Therefore, it was decided to reload the specimen. Upon reloading, it failed at 131 kips, compared to the initial 221 kip load. At this point, the specimen showed obvious signs of failure as the FRP tube cracked open along one of its edges (Figure 3.4). It was later concluded that this was due to the square shape of the cross-section and the stress concentration at the corners. Nonetheless, the rest of the confined specimens failed in a similar fashion, with the thickness of the jacket having little or no effect on the added strength to the concrete core. Figures 3.5 and 3.6 show the failure modes of the FRP-encased specimens with 10 and 14 plies, respectively. Note how most of the specimens appear intact, with the white patches barely visible. This clearly shows that the FRP tubes are not fully utilized as hoop tension bands. The average strength for the unconfined square specimens was 202 kips, while the average strength for the FRP-encased specimens was 233 kips. This resulted in a strength increase of only 15%, which was rather independent of the jacket thickness. For the 6-layer specimens, the average strength was 228 kips. Both the 10 and 14-layer specimens had average strengths of about 236 kips. Recalling that the average strength of all FRP-encased specimens was 233 kips, it can be seen that perhaps any thickness larger than 10 layers might be unnecessary, as the tube would be under-utilized. It should be noted, however, that for cylindrical FRP-encased specimens, strength increases of about 300% had been obtained (Mirmiran 1997). Another aspect to be noted was the duration of each test, since this was an indication of the straining capacity of the FRP-encased specimens. The average duration for the unconfined specimens was about 95 seconds,

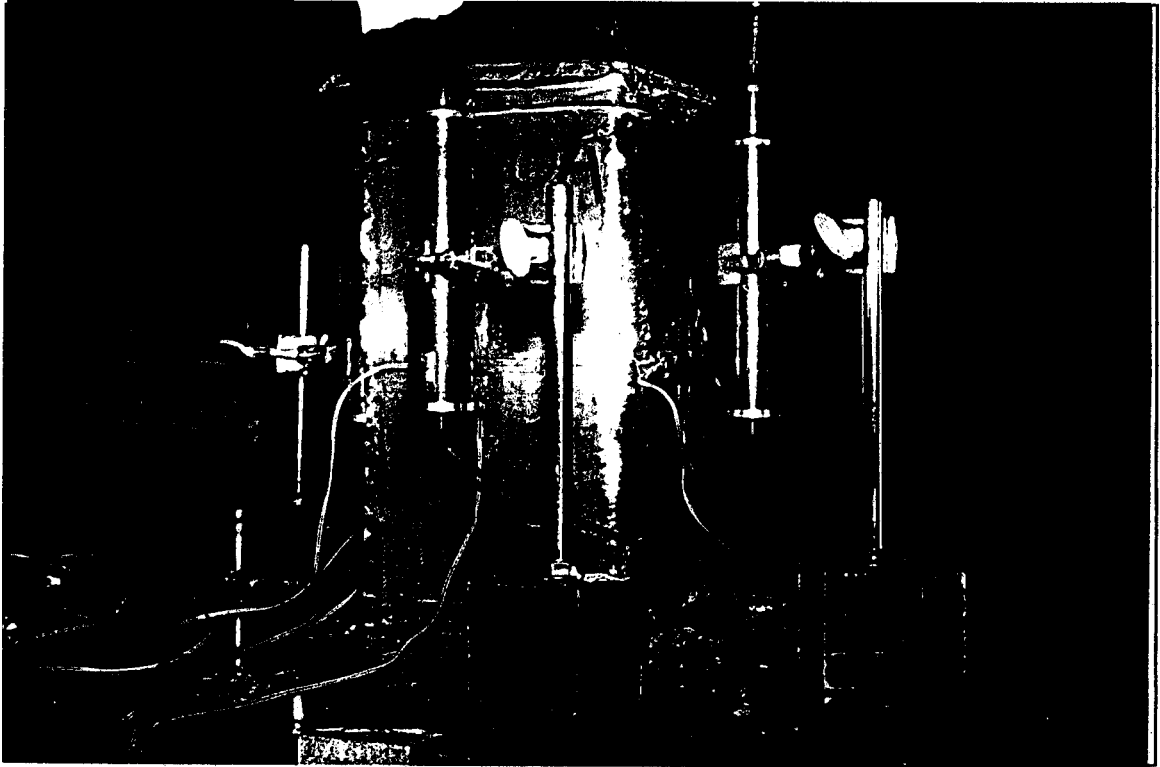


Figure 3.3 Instrumentation for a square tube

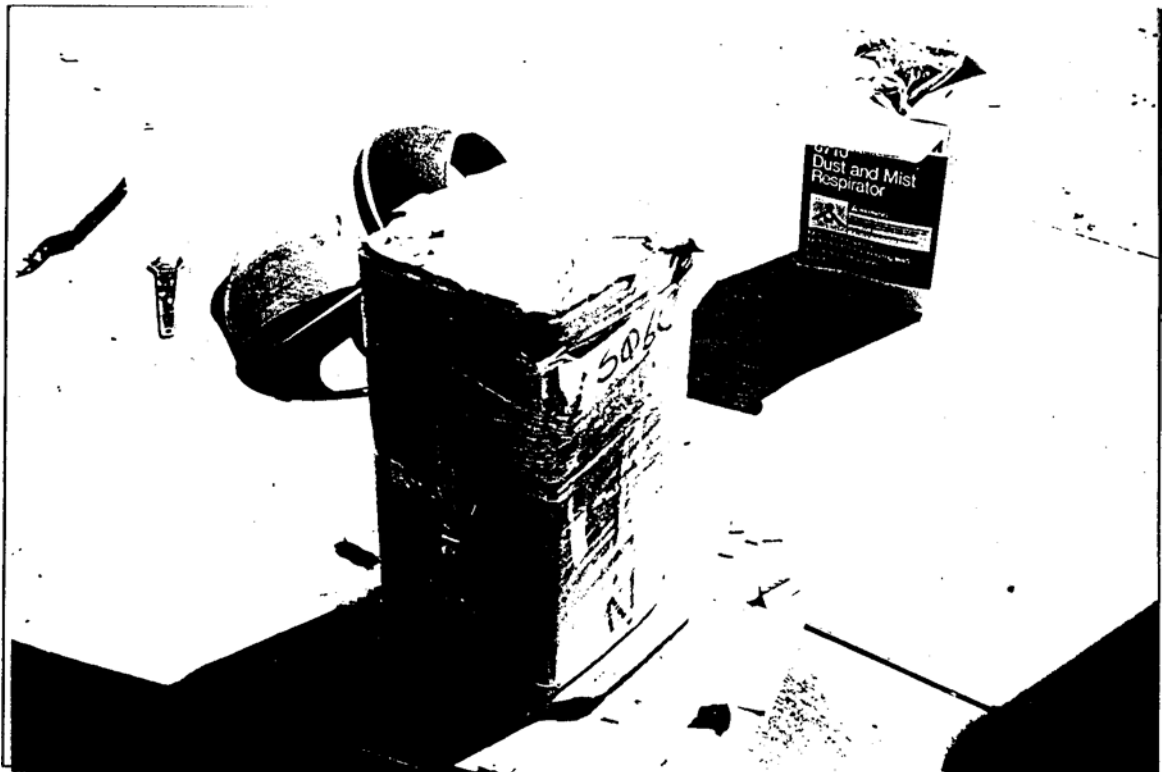


Figure 3.4 Specimen SQ6C after reloading -35-

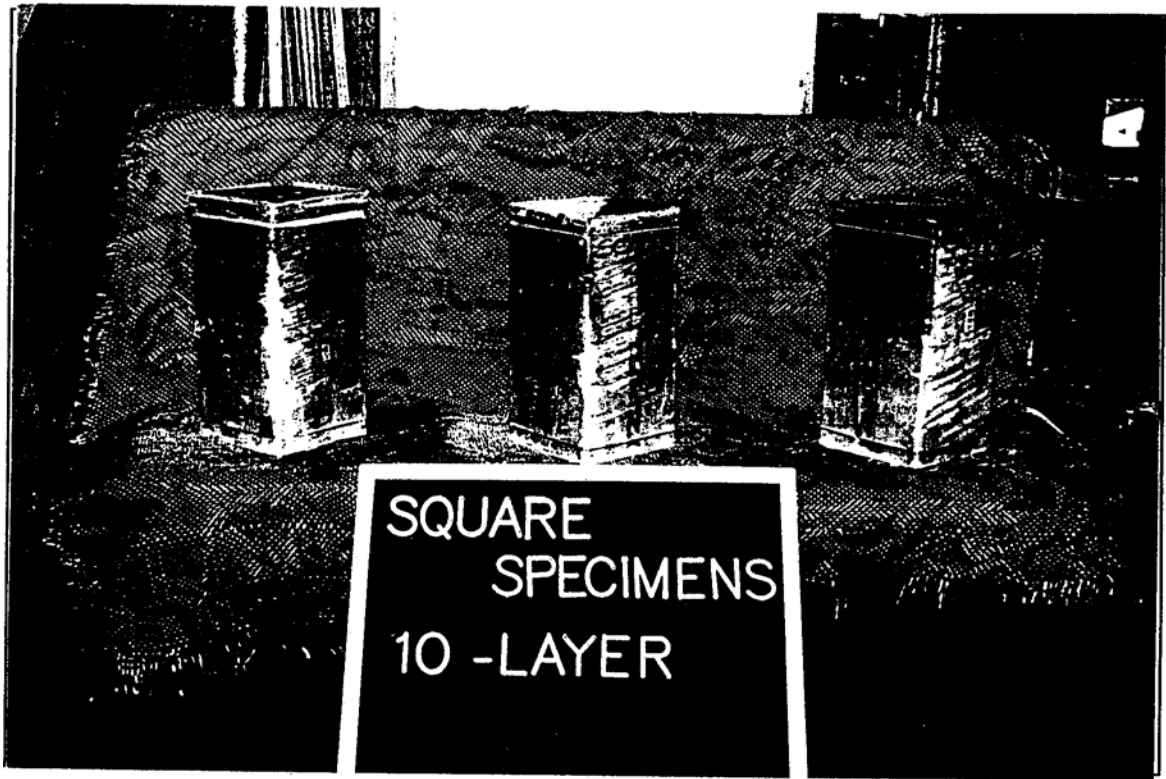


Figure 3.5 10-ply specimens after

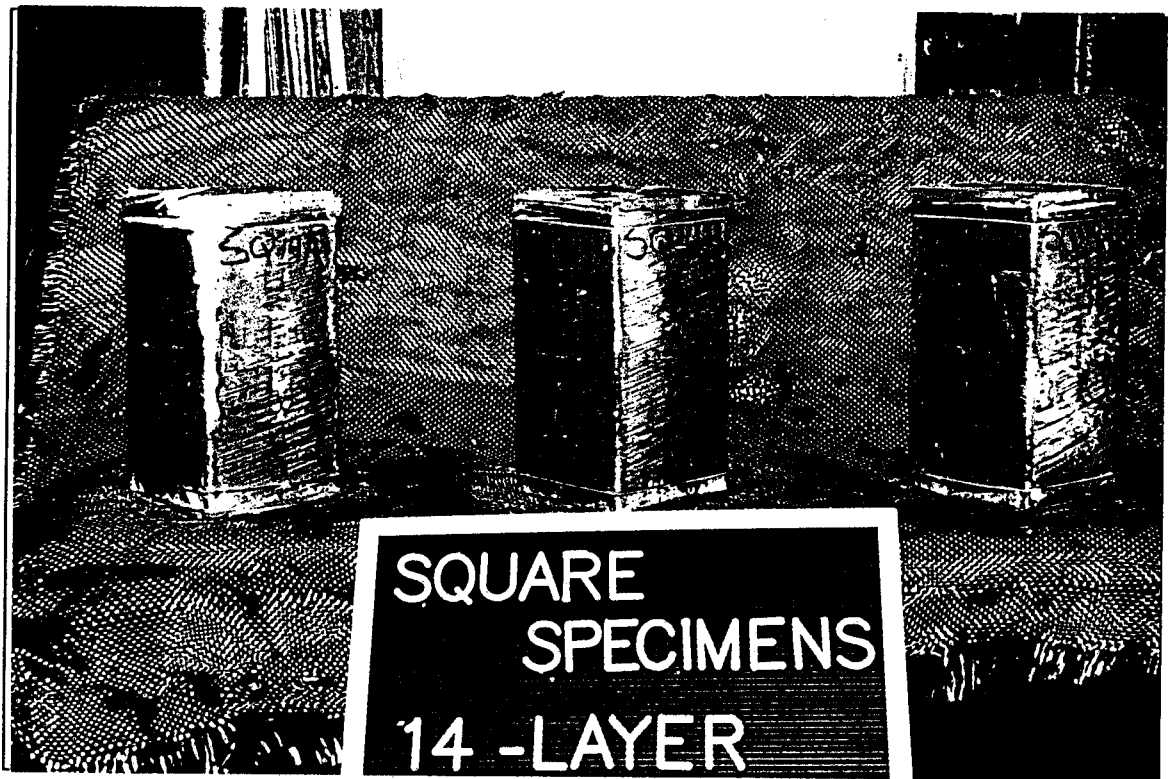


Figure 3.6 14-ply specimens after failure -36-

compared with 103 seconds for the FRP-encased specimens. Specimens SQ10C and SQ14A lasted longer than the average, failing at 153 and 136 seconds after the start of loading, respectively. If these two specimens were counted out, then the average duration for the fiber reinforced specimens would be about the same value as for the control specimens. All in all, failure of the jacketed specimens was quite passive and ductile, lacking any violent or explosive failure such as concrete pieces being shot at high speeds. Finally, three issues regarding the accuracy of test results, and the task of data reduction should be mentioned:

1. It was noticed that due to the uneven surface of FRP tubes, a few of the strain gages were partially detached from the tube during the test. This may have also been due to inadequacy of the glue used for affixing the gages. Since four strain gages were used in each direction, and since four LVDTs were also present, the gages with non-consistent readings were discarded. All in all, since the strain gages were considerably long (60mm gage length), the partial detachment did not seem to affect but the few gages that were noticed during the tests.
2. It was noticed that due to uneven surface of the tube and the capping plate, some eccentricity was present in a few of the tests. This non-verticality resulted in slight tilting of the loading platens. However, due to the short height of the specimens, this did not appear to have affected any of the test results.
3. An initial strain hardening was noticed in almost all specimens which was attributed to the soft capping materials. This was corrected in all stress-strain curves as outlined in the Final Report of Phase I (Mirmiran 1997).

### Test Results

Tables 3.2 and 3.3 show a summary of the test results. The tables show the peak strength and strain of unconfined concrete ( $f'_{co}$  and  $\epsilon_{co}$ ), as well as the peak strength, ultimate strength and strain of confined concrete ( $f'_{cc}$ ,  $f'_{cu}$ , and  $\epsilon_{cu}$ ). The value of the lateral pressure  $f_r$  from the tube is determined as

$$f_r = \frac{2f_j t_j}{D} \quad (3.4)$$

where  $f_j$ = hoop strength of the jacket,  $t_j$ = jacket thickness, and  $D$  = inside dimension of the tube.

Figure 3.7 and 3.8 show the stress-strain response of control cylindrical and square specimens, respectively. Both graphs are drawn based on the LVDT readings, as none of the control specimens were instrumented with strain gages. It is clear that neither the peak strength nor the corresponding strain are significantly affected by the cross-sectional shape of unconfined concrete. However, the elastic modulus of cylindrical specimens is on the average about 15% higher than that of square specimens. Also, regardless of the cross-sectional shape, the

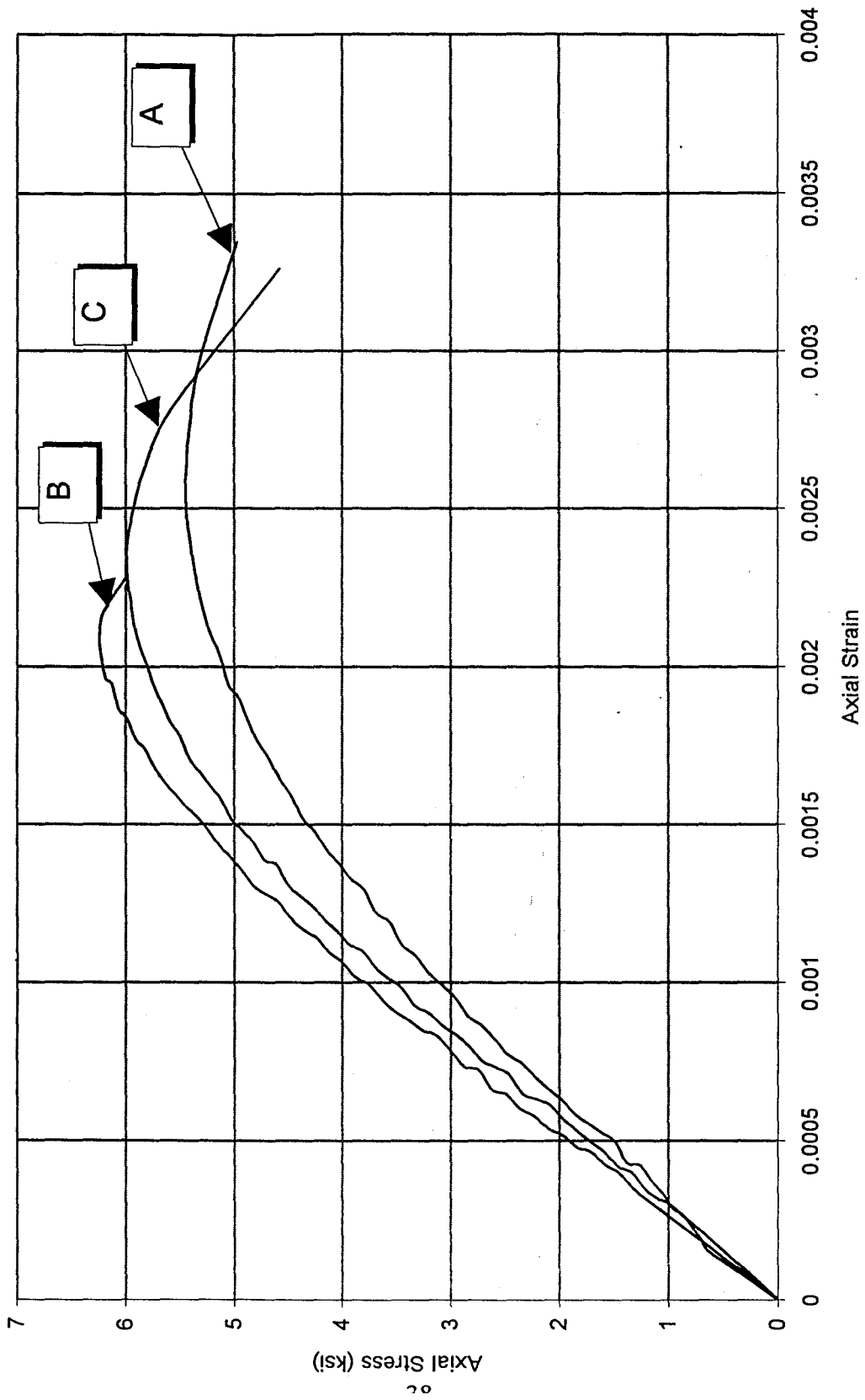


Figure 3.7 Stress-strain curves for plain concrete cylindrical (control) specimens



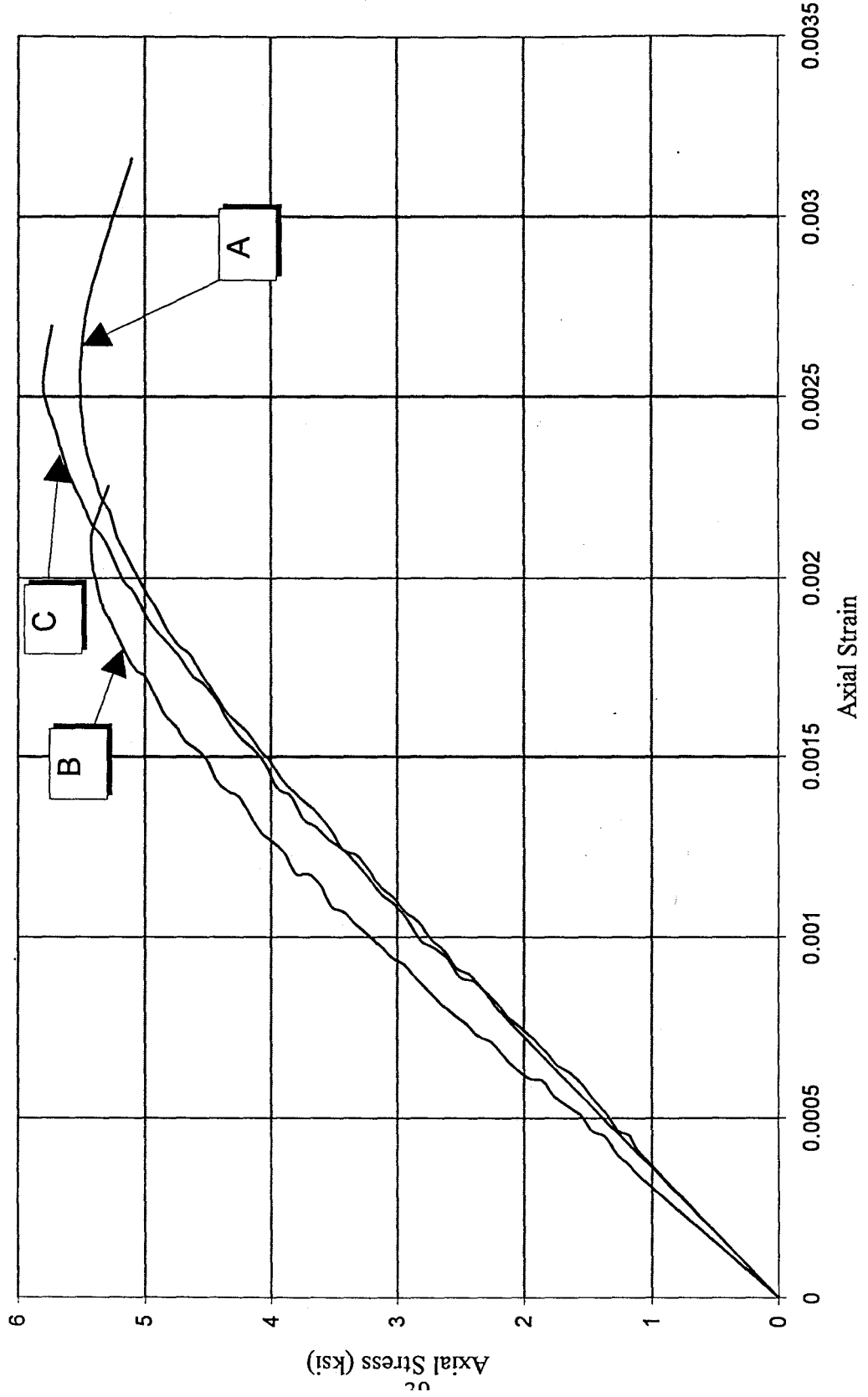


Figure 3.8 Stress-strain curves for plain concrete square (control) specimens

Table 3.2 Summary of results for unconfined specimens

Cross Section	Specimen No.	Peak Strength, $f'_{co}$ (ksi)	Peak Strain, $\epsilon_{co}$
Square	SQ0A	5.51	0.0025
	SQ0B	5.41	0.0021
	SQ0C	5.80	0.0025
Circular	CYL0A	5.44	0.0026
	CYL0B	6.24	0.0021
	CYL0C	5.99	0.0023

Table 3.3 Summary of results for confined specimens

Specimen No.	Peak Strength, $f'_{co}$ (ksi)	Ultimate Strength, $f'_{cu}$ (ksi)	Ultimate Strain, $\epsilon_{cu}$ *
SQ6A	6.93	3.3	0.0080
SQ6B	5.83	3.7	0.0100
SQ6C	6.21	3.8	0.0076
SQ10A	6.56	3.9	0.0150
SQ10B	6.74	5.0	0.0165
SQ10C	6.28	5.0	0.0165
SQ14A	6.08	4.5	0.0106
SQ14B	6.55	5.5	0.0085
SQ14C	6.95	4.8	0.0105

\* Since some of the tests were stopped soon after the load stabilized and not at subsequent load drops, the ultimate strain is to be treated as a lower bound value.

Biaxial stress-strains curves for the 6, 10, and 14-ply concrete-filled FRP tubes are shown in Figures 3.9-3.11, respectively. Figure 3.12 shows curves with the average for each specimen type, including the unconfined square specimens. As can be seen from this figure, the slope of the unconfined concrete is the same as the slope for the confined concrete. This shows that as the load is applied, concrete is taking most of the axial load in the elastic region. Upon careful observation, the stress-strain curves for all specimens depart from their linear shapes and begin to curve at about the point where the unconfined concrete nears its peak strength. This means that the specimens have entered into a transition zone. At this point, the concrete core has significantly cracked, and the FRP tube becomes effective as a hoop tension band, and the only restraint against catastrophic failure. Although increase in strength is not considerable, it is quite obvious that confinement by FRP tube provides significant ductility for concrete, as the descending branch of the curves for the FRP-encased specimens show plastic deformations not seen for any of the unconfined specimens. As mentioned in test observations, tube thicknesses of above 10 plies appear to be unnecessary for strength enhancements. From Figure 3.12, it can be seen that this is true for the peak strength of confined concrete, as the curves for the 10 and 14-ply specimens peak at about the same value.

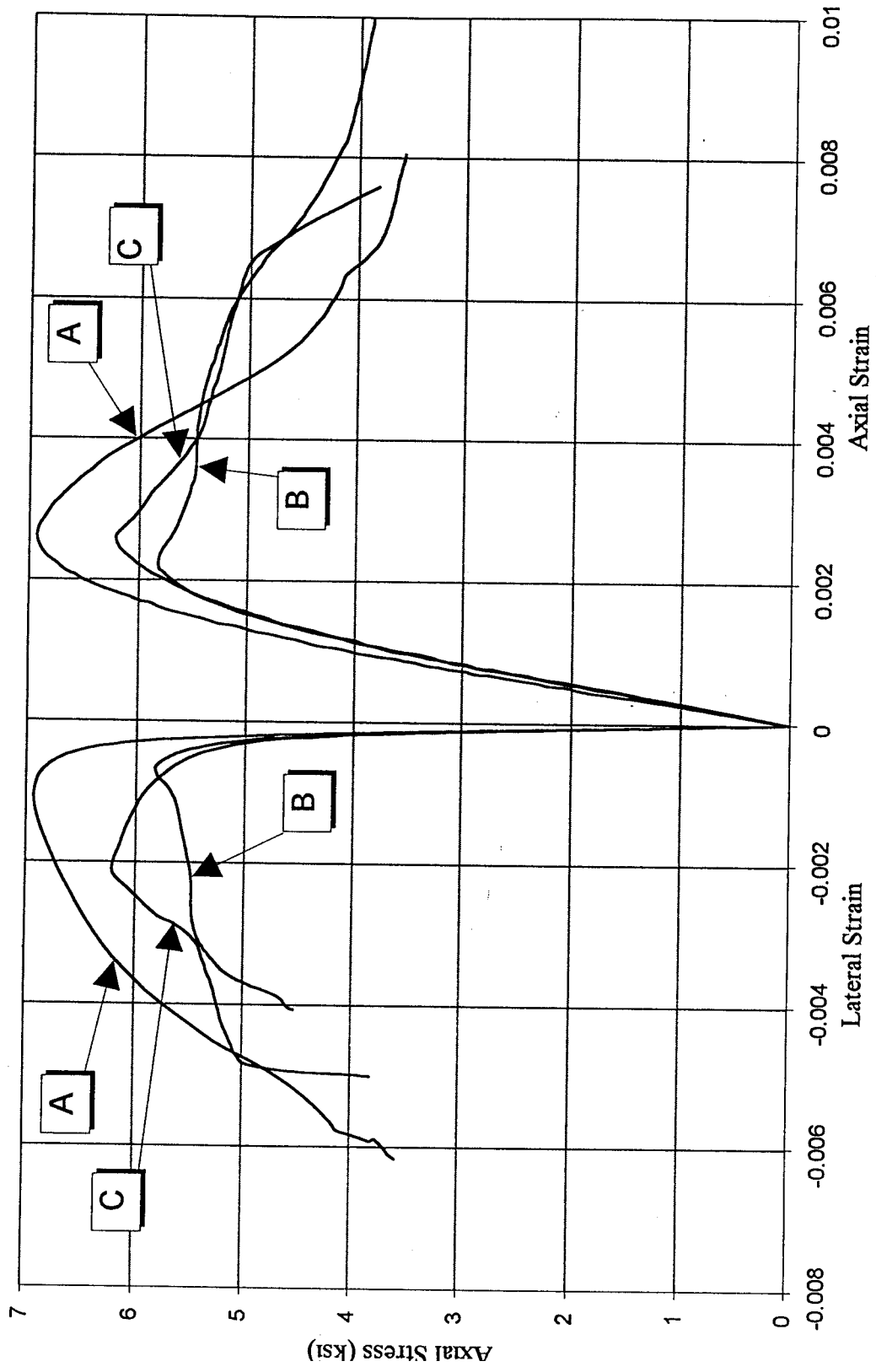


Figure 3.9 Biaxial stress-strain for 6-ply concrete-filled square FRP tubes

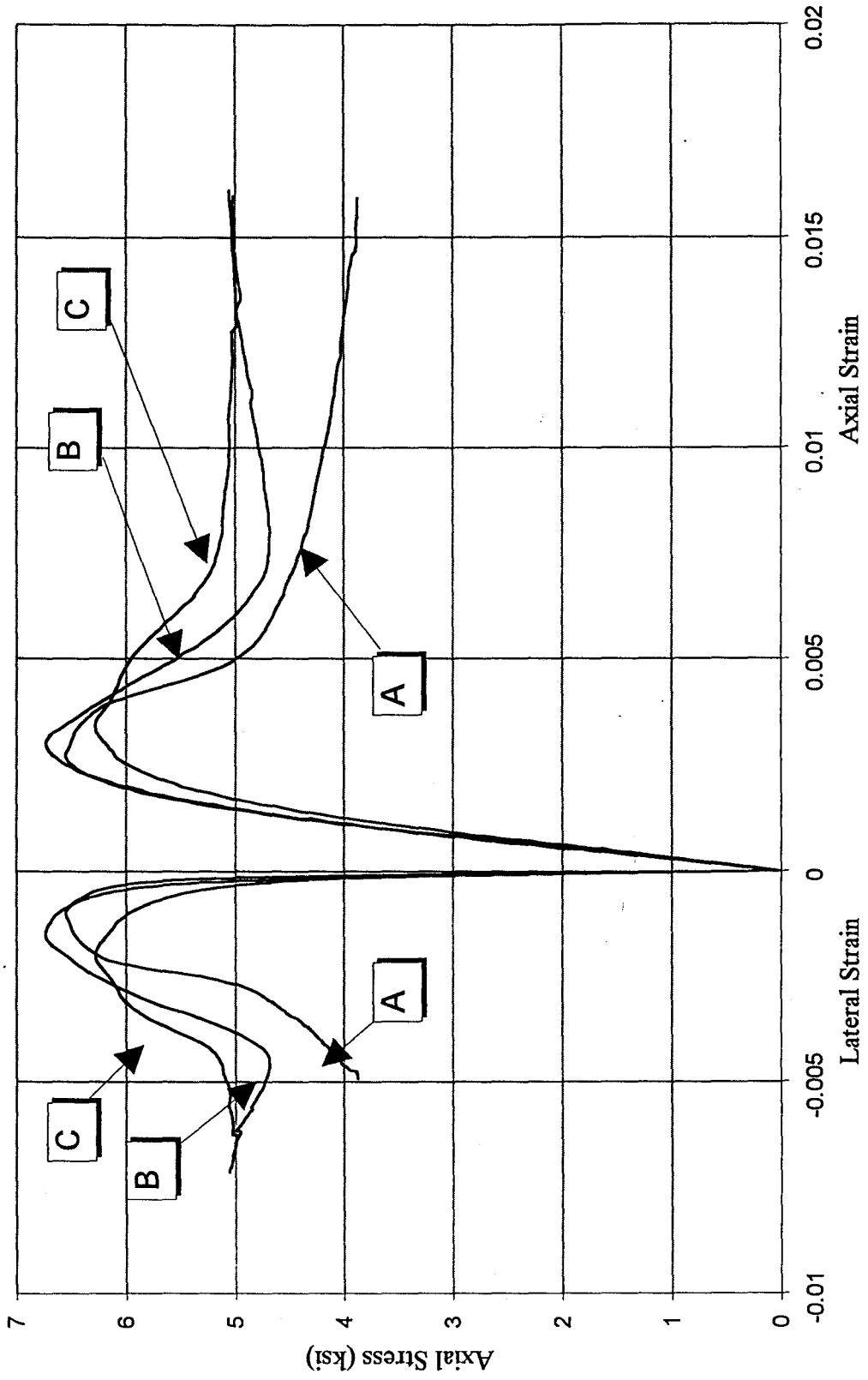


Figure 3.10 Biaxial stress-strain for 10-ply concrete-filled square FRP tubes

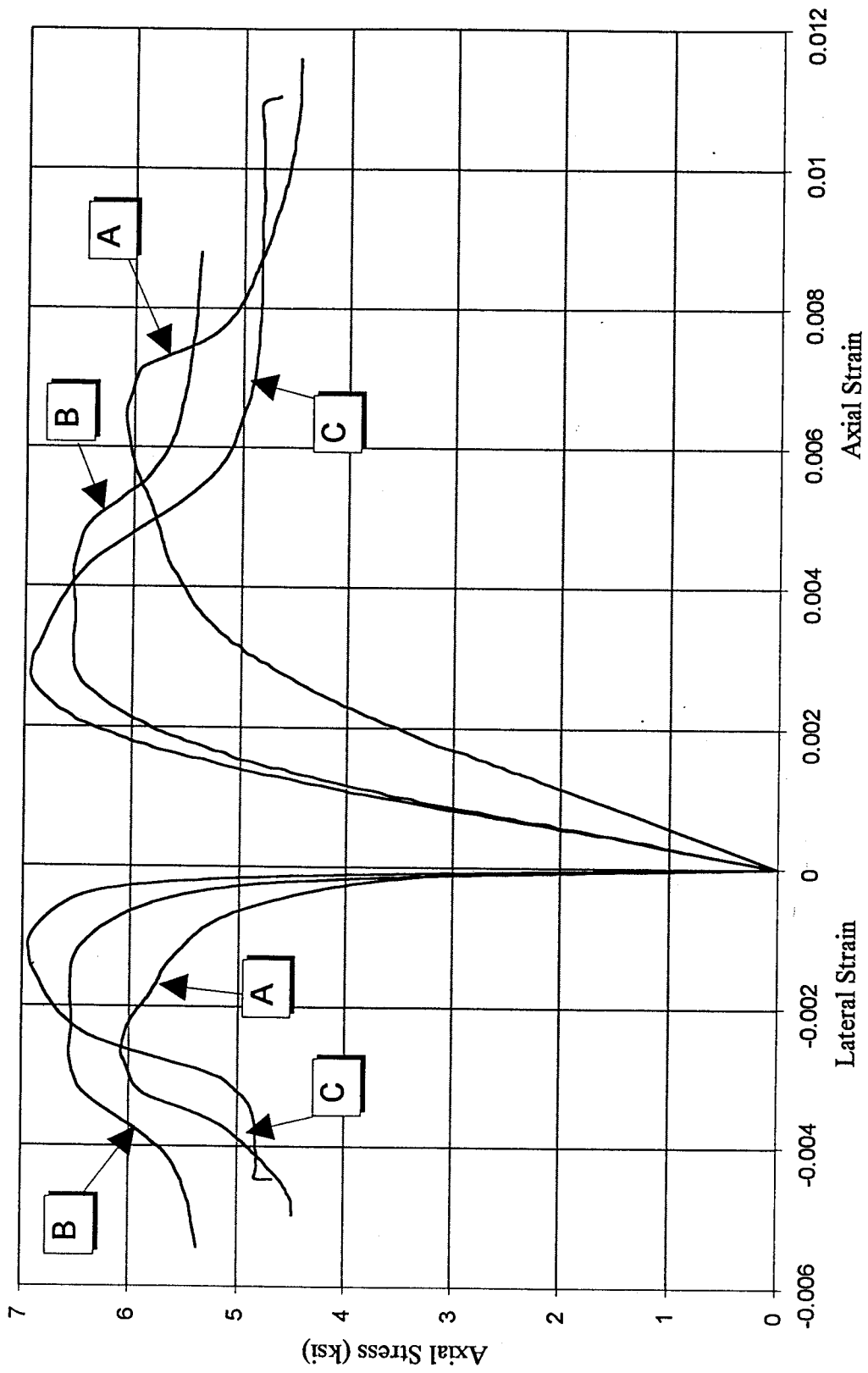


Figure 3.11 Biaxial stress-strain for 14-ply concrete-filled square FRP tubes

However, the thickness of the tube seems to have a direct effect on the descending branch. The curve for the 6-ply specimens shows complete failure shortly after the peak. The specimens with 10-ply tubes show a rather long plastic zone and a higher plastic strength. The plastic strength is further increased for the 14-ply tubes, indicating the effectiveness of the tube thickness when the concrete core is practically crushed.

Plots of lateral strains versus axial strains are shown in Figure 3.13. Each curve represents an average of the three similar specimens. It should be noted that the slope of these curves is a representative of the Poisson's expansion (or dilation) of the concrete core. The curves for all three thicknesses begin with a Poisson's ratio of about 0.15 to 0.22, which is the characteristic of plain concrete. At about an axial strain of 0.002, i.e., peak strain of plain concrete, the curves begin to shift to a higher slope, indicating that concrete has considerably cracked and become unstable. Between axial strain values of 0.002 and 0.006, lateral strains increase at a non-linear rate, while at about halfway in this range they transition through an inflection point indicating a maximum slope, and a tendency to control further dilation of concrete. This is the point when the tube becomes actively involved as a hoop tension band. After strain value of 0.008, the relationship becomes linear again, with the thinner jackets displaying a higher slope. Another observation that can be made is that thicker jackets have lower lateral strains in relation to their axial strains. This indicates that specimens with thicker jackets will take longer to reach their lateral failure strains.

There is another variable known as dilation rate that can be determined from the previous curves. Dilation rate is the rate of change of lateral strains with respect to axial strains. In mathematical terms, it is the slope or the first derivative of the lateral-axial strain plots. The experimental dilation rate,  $\mu_{exp}$  is calculated for every two consecutive readings as follows:

$$\mu_{exp} = \frac{\Delta \epsilon_r}{\Delta \epsilon_1} = \frac{\epsilon_{rnew} - \epsilon_{r old}}{\epsilon_{1new} - \epsilon_{1 old}} \quad (3.5)$$

where  $\epsilon_r$  and  $\epsilon_1$  represent the lateral and axial strains, respectively.

Figure 3.14 shows the average plots of dilation rates versus axial strains. Each curve represents an average of the three similar specimens. The dilation curves show three distinct regions. The first region indicates a gradual increase in the dilation rate from a starting point of about 0.15 to 0.20, which is the Poisson's ratio for plain concrete. As concrete begins to crack, the curve becomes steeper, resulting in a rapid increase in the dilation rate. The dilation rate keeps increasing until it reaches a peak. Thicker jackets have lower peaks, since they provide more confining pressure. It appears that the peak dilation rate occurs at an axial strain of about 0.004, which is the ultimate strain of unconfined concrete. After the peak, dilation rate decreases rapidly, indicating that the jacket is effectively containing the crack openings. Eventually, dilation rate stabilizes around a constant value. At this point, the concrete has reached its maximum lateral straining rate and the jacket is effectively containing the internal cracks of the concrete core.

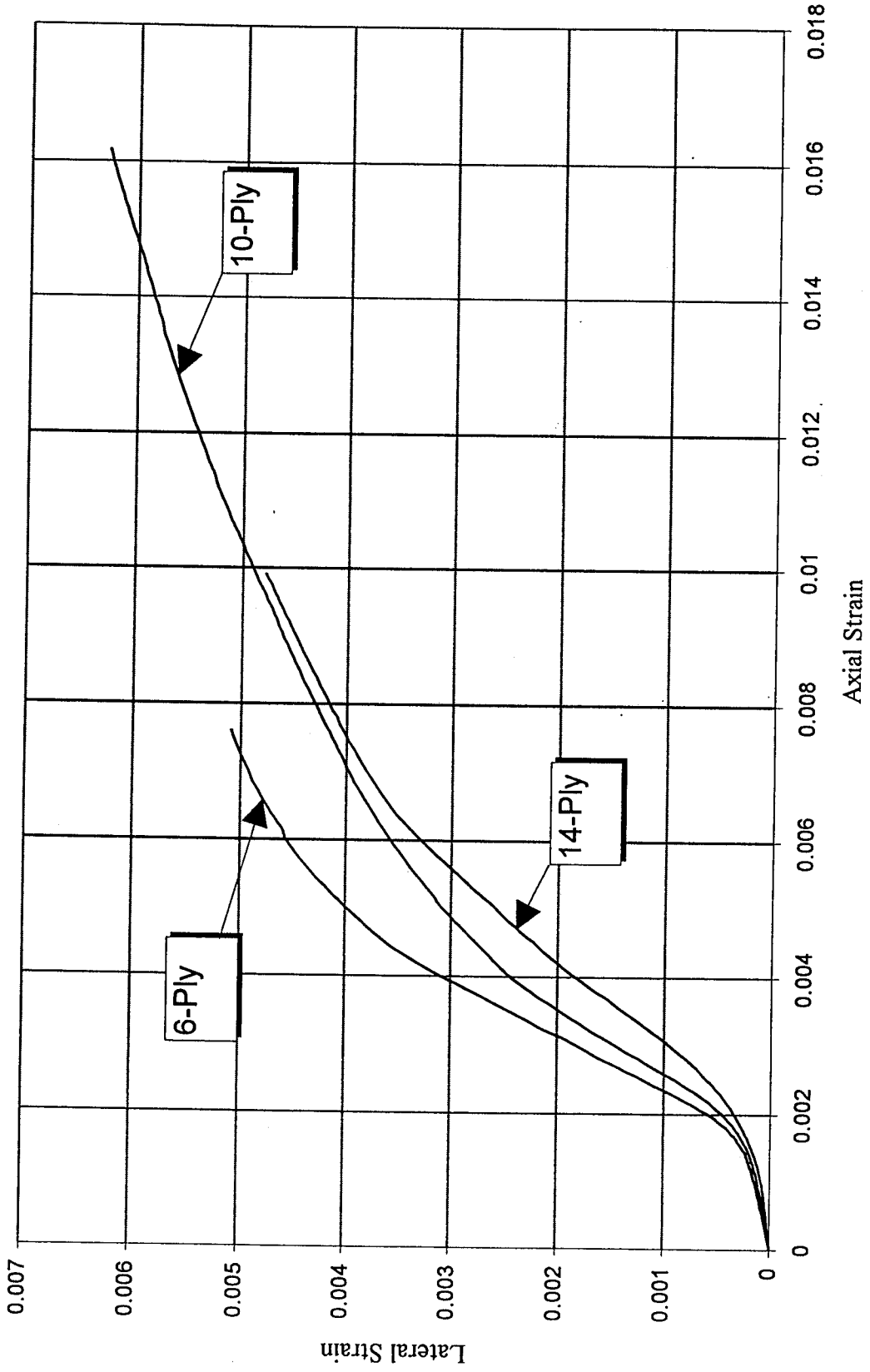


Figure 3.13 Average lateral strain versus axial strain for concrete-filled square FRP tubes

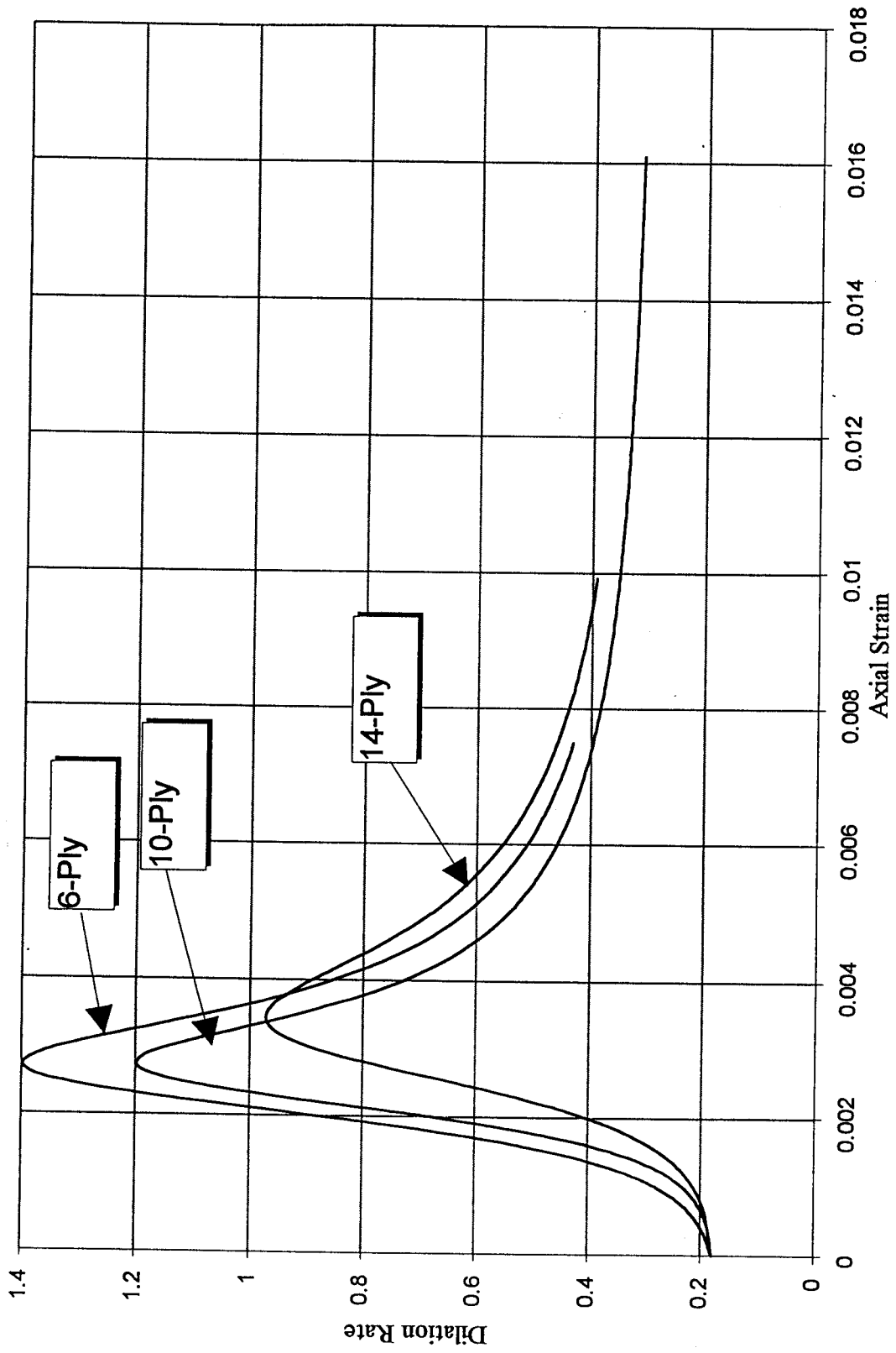


Figure 3.14 Average dilation rates for concrete-filled square FRP tubes



The plastification of FRP-encased concrete in the descending branch can also be looked at in terms of its volumetric strain. Figure 3.15 show the average plots of axial stress versus volumetric strain for each tube thickness. The horizontal axis in all these figures represents the change in volume per unit volume of concrete. This is calculated by adding the axial and lateral strains as

$$\frac{\Delta V}{V} = \epsilon_v = \epsilon_1 + 2 \epsilon_r \quad (3.6)$$

where  $\epsilon_v$  = volumetric strain,  $\epsilon_1$  = axial strain, and  $\epsilon_r$  = lateral strain. Sign convention is negative for lateral strains which are tensile strains. Also, positive volumetric strains represent volume reduction while negative values indicate volume expansion (dilation). Referring back to Figure 3.15, all specimens begin to gradually decrease in volume until they reach a point of maximum compaction. At this point, the specimens enter a zone of expansion until failure happens. As can be seen in the figure, specimens with thicker jackets have a lower slope in the volume reduction zone, indicating better confinement than specimens with thinner jackets. One important point that should be discussed is how these plots compare with the ones obtained from cylindrical specimens of Phase I (Mirmiran 1997). Although both circular and square sections appear to effectively contain the dilation of concrete core, and leading the specimen to the compaction (or volume reduction) zone, the reversal occurs at higher stresses for circular sections as compared to square sections. That is why plastification of the section takes place within the post-peak response of the square sections.

From the standpoint of plasticity in concrete, plots of octahedral shear stresses versus octahedral normal stresses indicate the true loading surface of the specimen, and its deviation from the pure uniaxial compression. Figure 3.16 shows the average octahedral loading surfaces

$$\begin{aligned} \tau_{oct} &= \frac{\sqrt{2}}{3} (f_c - f_r) \\ \sigma_{oct} &= \frac{1}{3} (f_c + 2 f_r) \end{aligned} \quad (3.7)$$

where  $\tau_{oct}$  = octahedral shear stress,  $\sigma_{oct}$  = octahedral normal stress,  $f_c$  = axial stress, and  $f_r$  = lateral stress. The lateral stress is determined from the following equation:

$$f_r = \frac{2 E_j t_j}{D} \epsilon_r \quad (3.8)$$

where  $E_j$  = modulus of elasticity of the tube in the hoop direction. The straight line with the slope of d:2:1 represents the pure uniaxial compression test with no confining pressure. As confining pressure increases, deviation from this line becomes more significant. Referring back to Figure 3.16,

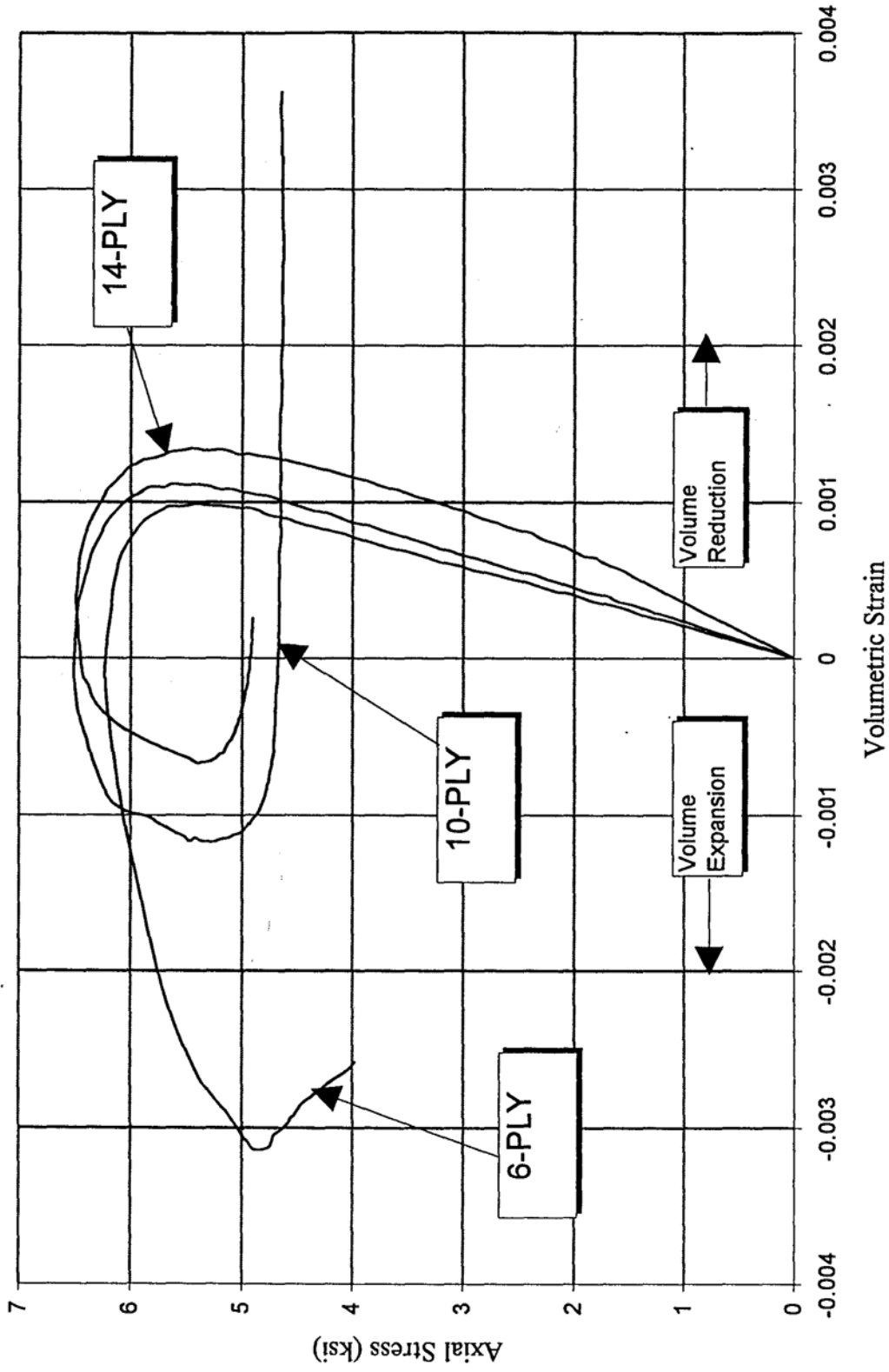


Figure 3.15 Average axial stress versus volumetric strain for concrete-filled square FRP tubes

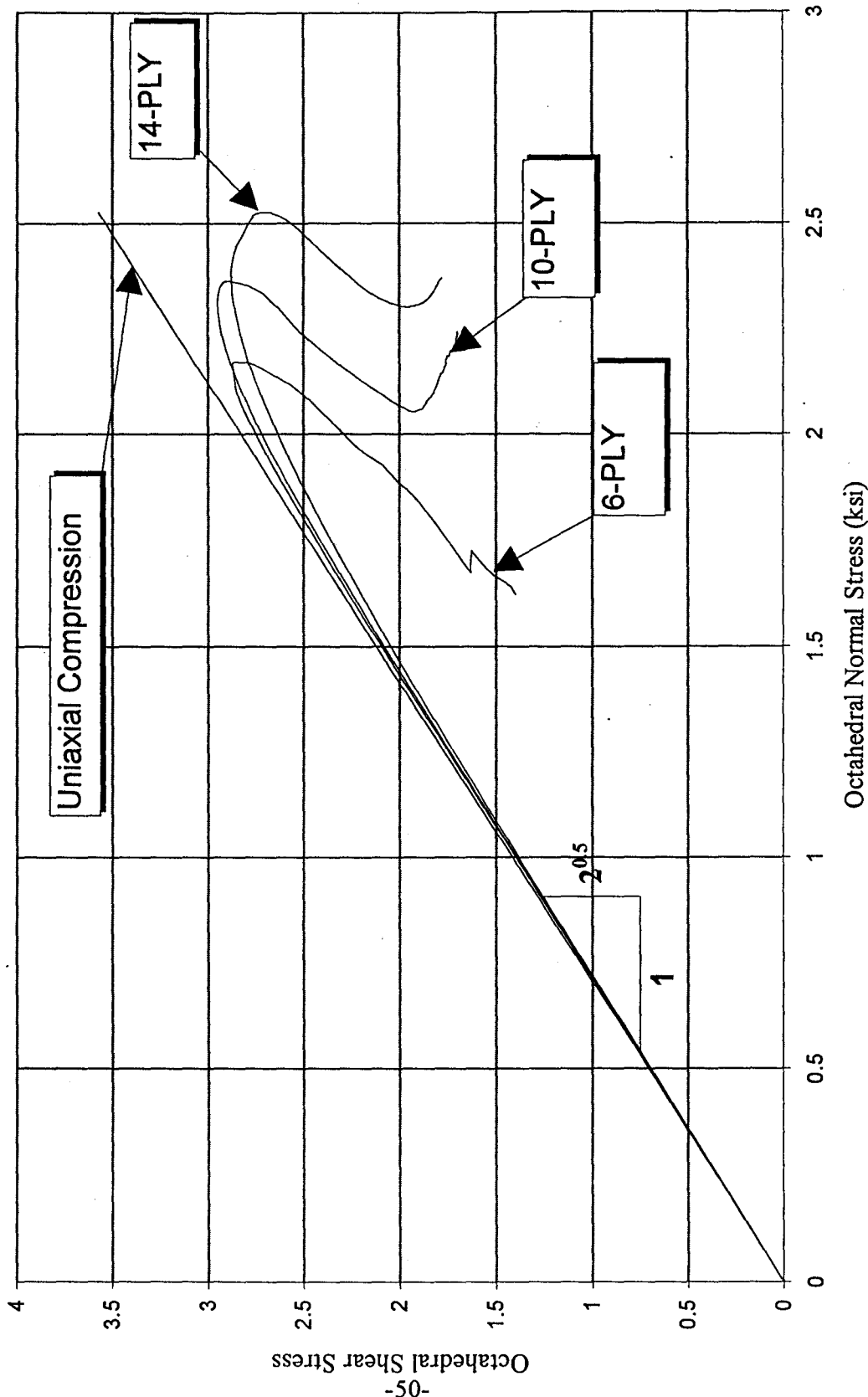


Figure 3.16 Average octahedral loading surfaces for concrete-filled square FRP tubes

it is clear that this deviation occurs earlier for the thicker tubes, indicating that thicker tubes become activated as hoop tension bands sooner than thinner tubes. The peak octahedral shear strength, however, does not appear to depend very much on the tube thickness. On the other hand, the octahedral shear and normal stresses, around which some level of plasticity occurs, seem to be a function of jacket thickness. These are indicative of post-peak response of square sections. Results of Phase I (Mirmiran 1997) indicate that for circular sections the octahedral loading surfaces have a totally different pattern, as no peak stress nor descending branch is present in their response.

### 3.3 Analysis and Discussion

In this section, an attempt is made to model the true response of FRP-confined concrete sections. First, experimental results of the square sections are compared with those of circular sections tested under Phase I (Mirmiran 1997). To shed more light on the reasons for the observed behavioral differences, results of extensive tests at the University of Sherbrooke on fiber-wrapped square and circular concrete specimens are analyzed next (Rochette 1997). Finally, an equation is proposed for confinement with square tubes.

#### Comparison of the Responses of Circular and Square Sections

Under Phase I, 24 6"x12" concrete-filled FRP cylinders were tested as Series D, in 3 batches of concrete and with 3 different jacket thicknesses, equivalent of 6, 10, and 14 plies (layers). These tests were part of the total 52 concrete cylinders under uniaxial compression. Results were modeled in the Final Report (Mirmiran 1997). Figure 3.17 shows the average axial stress-strain curves for circular tubes of Series D, Batch C of Phase I together with the average curves for the square tubes of Phase II. Notice that the number of plies in both studies were kept the same. As the figure clearly shows, there are two major differences between the responses of circular and square sections:

- (1) Confinement effectiveness of circular sections is much higher, resulting in a strain hardening behavior after the peak strength of unconfined concrete, while square sections show a descending post-peak response, with little or no increase in their peak strength over that of unconfined concrete.
- (2) Ductility of circular sections is considerably higher by a factor of 6 to 7. While square sections reach their crushing ultimate strain at about 0.005 to 0.007, circular sections extend the ultimate strain of concrete to 0.03-0.045.

The figure, however, can not truly reveal the effect of cross-sectional shape, because the compressive strengths of the concrete core for the two experiments are different. Therefore, to eliminate the effect of unconfined concrete strength and to isolate the effect of cross sectional shape, the curves of Figure 3.17 are normalized and shown in Figure 3.18 by dividing values of each curve by the peak stress and strain of their corresponding unconfined concrete core. The figure shows that while jacket thickness greatly affects the response of circular tubes, for square sections, this effect is minimal. It appears that the descending branch of the response is stabilized at about 70% of the peak strength of unconfined concrete, irrespective of the tube thickness. Of course, there seems to be a threshold thickness between 6 to 10 layers, below which little or no post-peak plasticity occurs.

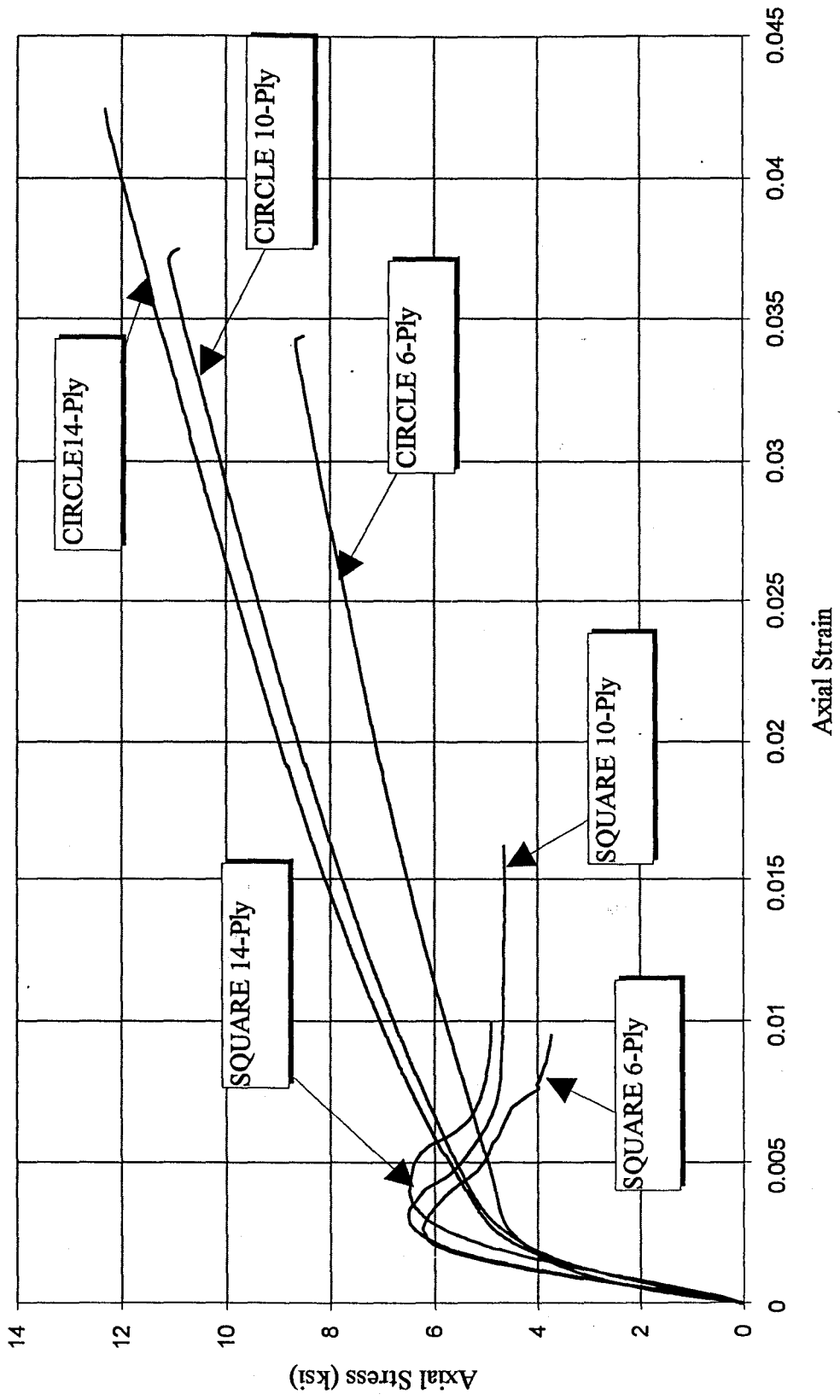


Figure 3.17 Average stress-strain curves for circular and square FRP tubes

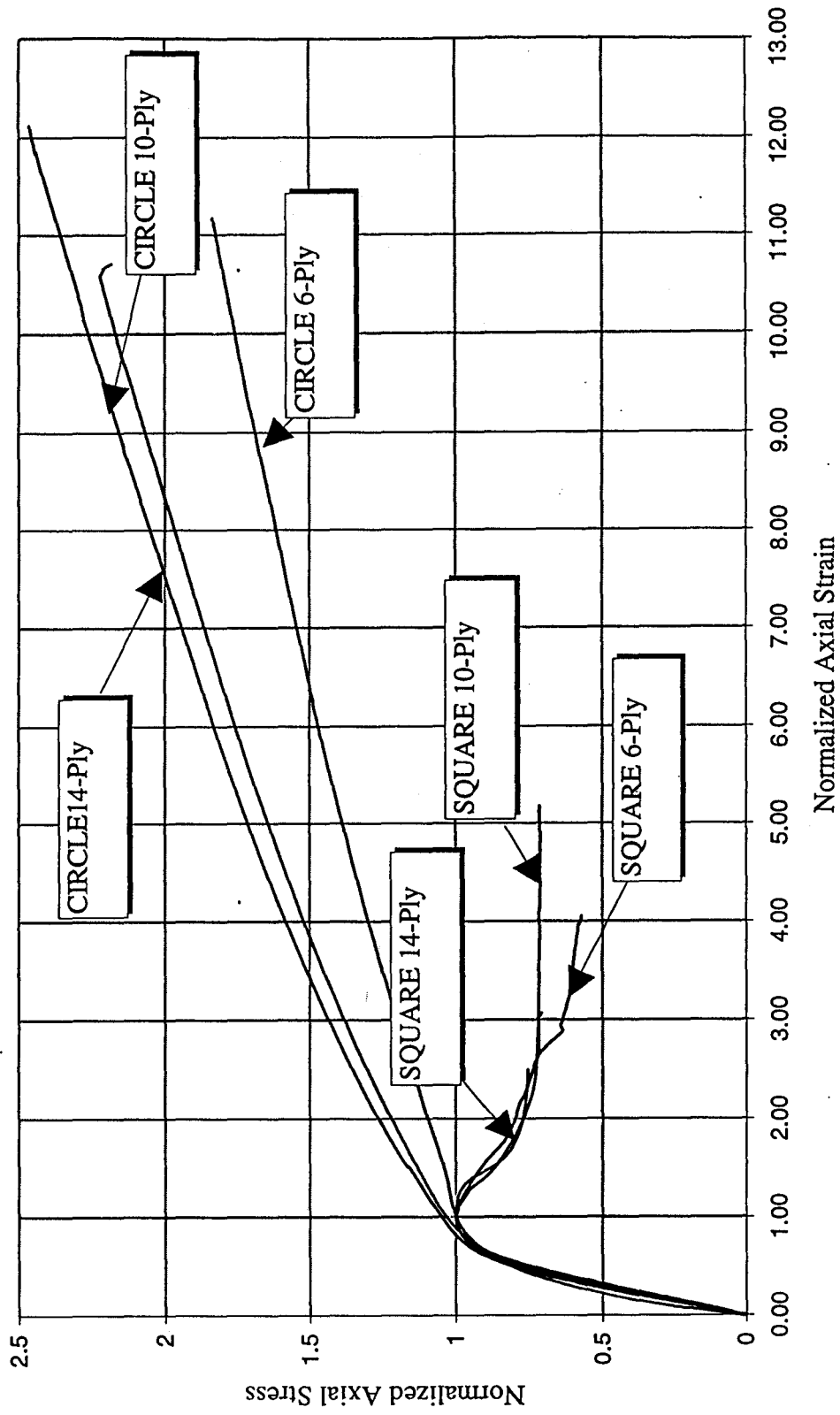


Figure 3.18 Normalized stress-strain curves for circular and square FRP tubes

Another important comparison between the square and circular sections is in their volumetric responses. Figure 3.19 shows the axial stress versus volumetric strain for the circular specimens of Series D, Batch C of Phase I, along with the square tubes of Phase II. The curves are again normalized in both directions to eliminate the effect of different concrete batches. As shown in the figure, circular sections tend to effectively curtail the dilation tendency of concrete while continually increasing the strength of the cross section. On the other hand, square sections achieve some level of crack dilatancy containment. However, in this process, strength of the cross sections does not increase, and is only stabilized after considerable post-peak strength degradation. The figure clearly shows that even though square sections are not as effective in confining the concrete core as circular sections, presence of FRP-materials contains the crack dilatancy of concrete much in the same fashion. When compared with steel-encased concrete, FRP materials reverse the direction of volumetric strains, and do not result in unstable dilation.

Finally, comparison of dilation rates for the circular and square sections can clarify some aspects of the behavioral differences between the two types of cross-sections. Figure 3.20 shows the average dilation rates for the 6, 10, and 14-ply circular tubes of Series D, Batch C of Phase I, and the square sections of Phase II. It is clear that the general shape of dilation curves is the same for both circular and square FRP sections, indicating that dilation response is a function of material properties of the tube rather than the cross-sectional shape. One needs to recall the dilation rate for an unconfined concrete which becomes unstable and approaches very large values at about the peak strength. Also, it should be noted that for steel-encased concrete, dilation rate, although initially contained, becomes unstable and approaches very large values as soon as the steel tube yields. There are however some differences in the dilation curves of the square and circular FRP tubes. First, it is clear that the peak dilation rate is higher for the square sections. This points to the fact that activation of the crack containment is delayed for square tubes. This may be explained by the distribution of lateral pressure in the circular and square sections.

Figure 3.21 shows the lateral pressure buildup in square and circular sections. This schematic diagram is modified after the work of Saatcioglu and Razvi (1992) on the confining effect of steel hoops. Passive confinement pressure exerted by a tube depends on the restraining force developed within the tube. For circular sections, maximum confining pressure can be developed because the tube can effectively act as a hoop tension band. Moreover, the hoop stresses and the confining pressures are, at least theoretically, uniform around the perimeter of the tube. On the other hand, for square sections, the tube can generate high restraining forces at the comers, where it is supported laterally by the transverse sides, and low restraining action between the comers. The restraining force at the corners depends on the force that can be developed in the transverse sides of the tube, which in turn relates to the thickness and hoop strength of the tube. However, the restraining action of the tube in between the comers is a function of the flexural rigidity rather than membrane action of the plate between the comers. The flexural rigidity of the FRP plate on each side of the tube depends on the thickness and materials of the tube as well as the unsupported length of the plate in the circumferential direction. Therefore, from Figure 3.21 it is clear that most of the confining pressure is built up around the comers of the tube, and as the comer radius is increased, the pressure distribution becomes more uniform. As such, it appears that the corner radius as well as the overall

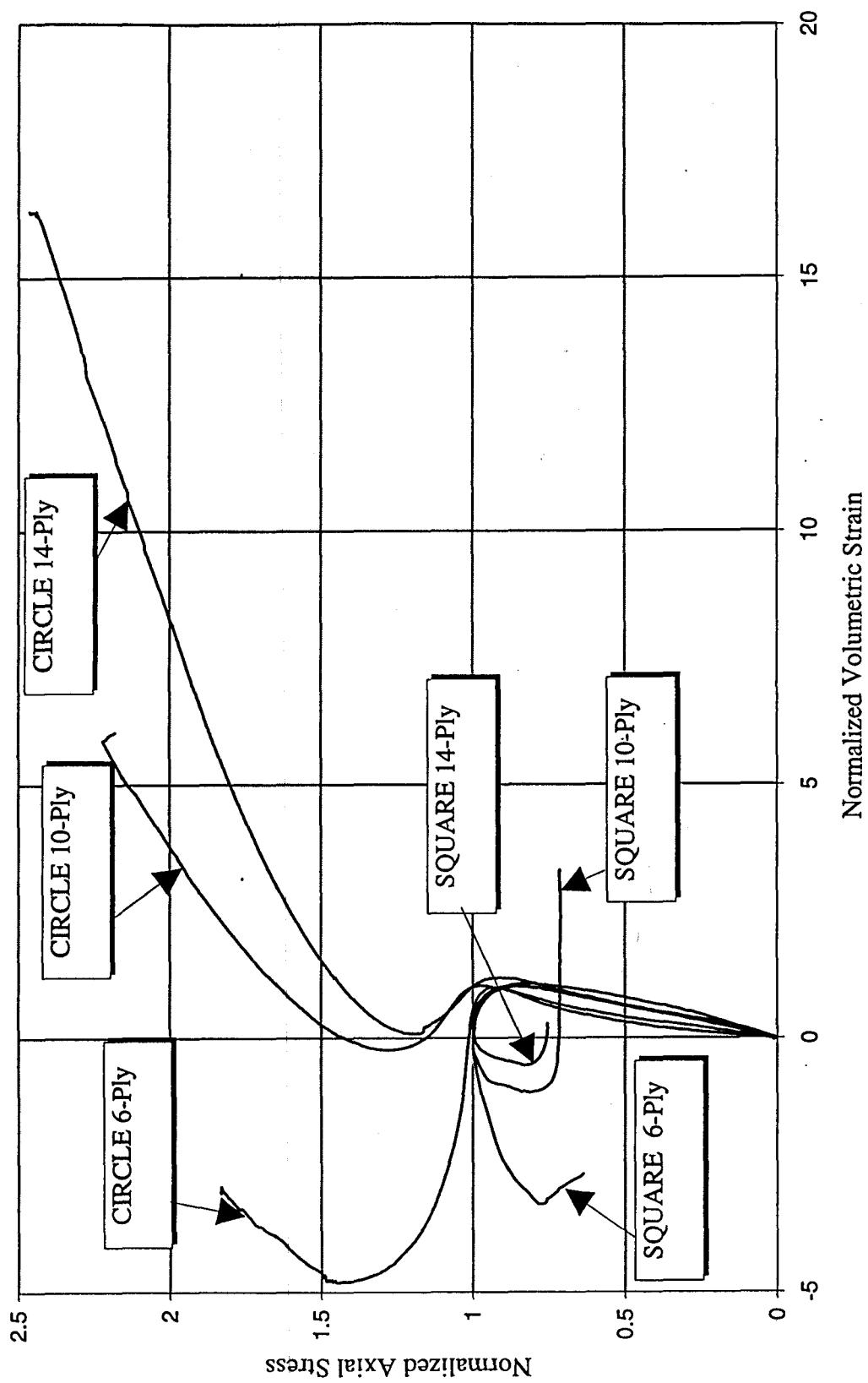


Figure 3.19 Normalized volumetric strain curves for circular and square FRP tubes



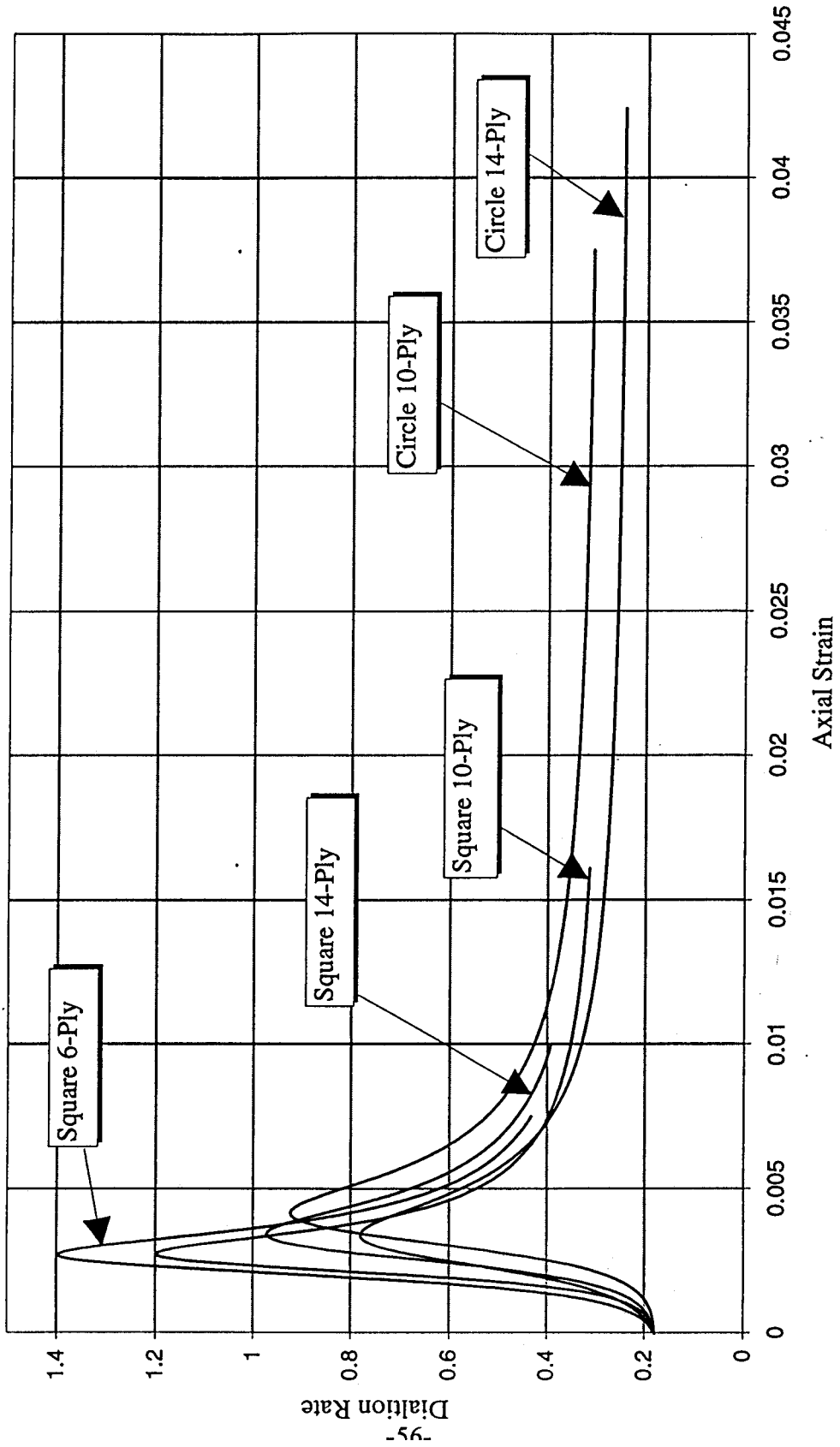


Figure 3.20 Dilation curves for circular and square FRP tubes

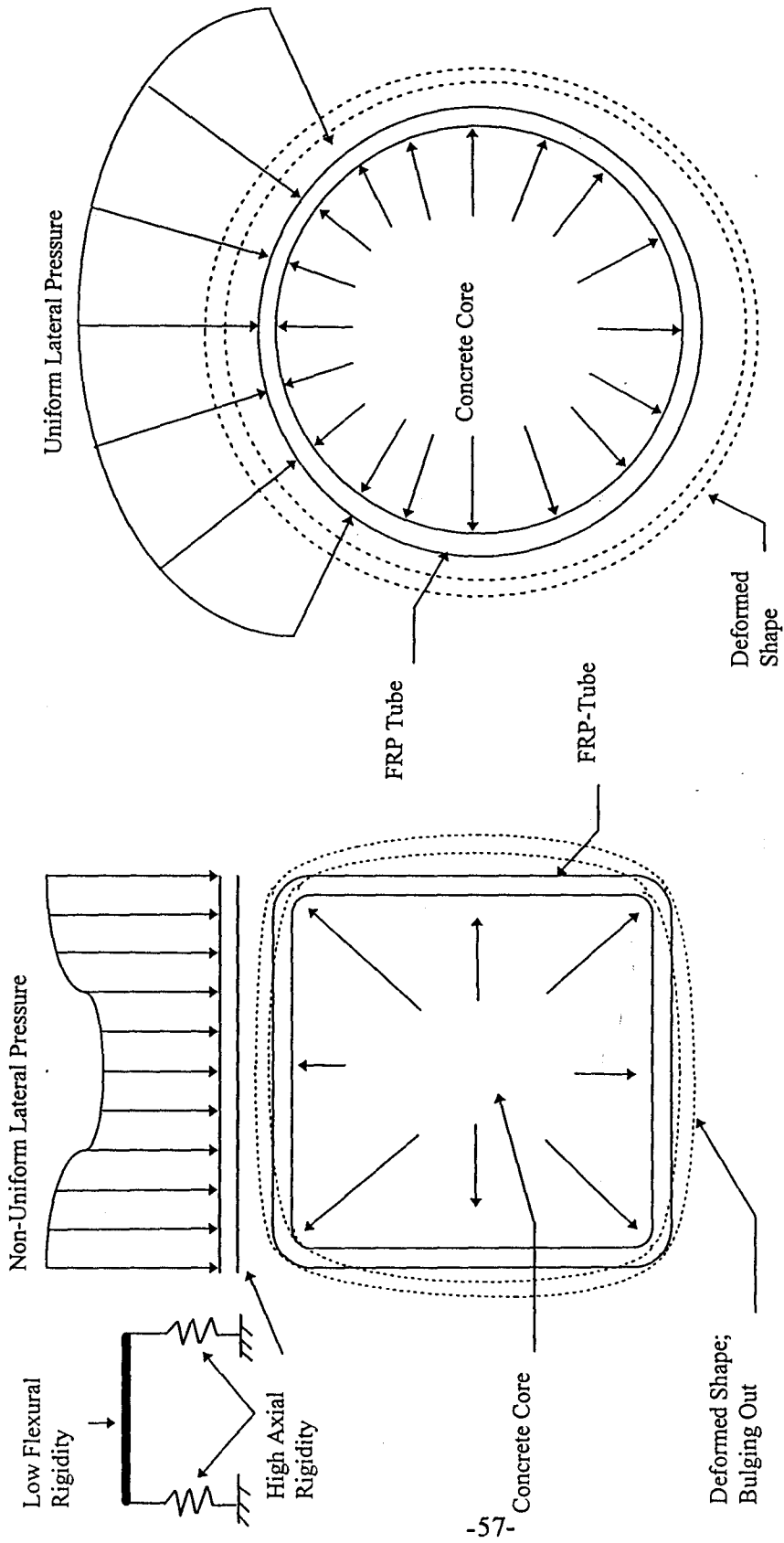


Figure 3.21 Lateral pressure buildup in square and circular sections

dimensions of the section have great impact on the confinement effectiveness of the square section. While the effect of the former can be modeled (as will be discussed at the end of this section), the latter parameter (size of the section) seems to impose an important restriction on the applicability of any such confinement model. In other words, while for circular sections, scale factor is not likely to cause a great impact on the modeling process, the unsupported length of large square sections most likely makes full-scale tests more necessary.

Finally, recalling Figure 3.20, and in light of the above discussion, without any attempt to quantify the dilation rates of the square sections, one notes the following:

1. The peak dilation rate of square sections is up to 20% larger than that of circular sections.
2. The ultimate dilation rate of square sections seems to be independent of the jacket thickness, but about the same as that of circular sections.

### Comparison with Fiber-Wrapped Specimens

To shed more light on the reasons for the observed behavioral differences between the circular and square tubes, in this section we shall examine some of the results of the extensive experiments on fiber-wrapped specimens conducted at the University of Sherbrooke in three separate studies (Demers and Neale 1994, Picher 1995, and Rochette 1997). Of these, the one by Rochette (1997) addresses the confinement of short square and rectangular columns with composite materials. It should be noted that there are some differences between the response of fiber-wrapped specimens and concrete-filled FRP-tubes (see Chapter 5). Despite the differences, general behavior of FRP-encased concrete, whether bonded or not, is the same, and therefore, it is reasonably justified to expand the limited database of the present study by tapping into the more extensive set of tests conducted in Canada (Demers and Neale 1994, Picher 1995, and Rochette 1997).

Rochette (1997) tested a total of 33 fiber-wrapped specimens and 5 control (unconfined) specimens. All specimens were tested in uniaxial compression. The parameters studied included cross-sectional shape (circular, square, and rectangular), fiber type (carbon and aramid), corner radius, number of composite layers or wraps (2 to 5 layers for carbon, and 3 to 12 layers for aramid). The concrete strength, although from different batches, generally ranged between 4.2 to 6.4 ksi. Table 3.4 shows the properties of fiber composites as provided by the manufacturer. Table 3.5 shows the test matrix and the results of uniaxial compression tests.

**Table 3.4 Material properties for fiber composites (Rochette 1997)**

Material	Modulus	Tensile Strength	Tensile Strain	Thickness
	(ksi)	(ksi)	(%)	(in)
Carbon	11993.0	183.5	1.5	0.012
Aramid	1972.2	33.3	1.69	0.016

Table 3.5 Test matrix and results of uniaxial compression tests by Rochette (1997)

Specimen	Section	Specimen Size	$t_j$ *	R *	$f'_{co}$ *	No. of Layers	Fiber
			(in)	(in)	(ksi)		
1A1	Circle	4"(dia.)x8"	0.02	1.97	6.09	2	Carbon
1A2	Circle	4"(dia.)x8"	0.02	1.97	6.09	2	Carbon
1A3	Circle	4"(dia.)x8"	0.02	1.97	6.09	2	Carbon
2B	Square	6"x6"x12"	0.04	0.20	6.09	3	Carbon
2C	Square	6"x6"x12"	0.06	0.20	6.37	5	Carbon
2D1	Square	6"x6"x12"	0.04	0.98	6.09	3	Carbon
2D2	Square	6"x6"x12"	0.04	0.98	6.09	3	Carbon
2E	Square	6"x6"x12"	0.05	0.98	6.37	4	Carbon
2G1	Square	6"x6"x12"	0.04	1.50	6.09	3	Carbon
2G2	Square	6"x6"x12"	0.04	1.50	6.09	3	Carbon
3B	Square	6"x6"x12"	0.05	0.98	5.19	4	Carbon
3C	Square	6"x6"x12"	0.06	0.98	5.19	5	Carbon
3D	Square	6"x6"x12"	0.05	1.50	5.19	4	Carbon
3E	Square	6"x6"x12"	0.06	1.50	5.19	5	Carbon
4B	Rectangle	6"x8"x20"	0.06	0.20	6.37	5	Carbon
4C	Rectangle	6"x8"x20"	0.04	0.98	6.09	3	Carbon
4D	Rectangle	6"x8"x20"	0.05	0.98	6.37	4	Carbon
4E	Rectangle	6"x8"x20"	0.04	1.50	6.09	3	Carbon
5A	Circle	6"(dia.)x12"	0.05	2.95	6.24	3	Aramid
5B	Circle	6"(dia.)x12"	0.10	2.95	6.24	6	Aramid
5C	Circle	6"(dia.)x12"	0.15	2.95	6.24	9	Aramid
5D	Circle	6"(dia.)x12"	0.20	2.95	6.24	12	Aramid
6A	Square	6"x6"x12"	0.05	0.20	6.24	3	Aramid
6B	Square	6"x6"x12"	0.10	0.20	6.24	6	Aramid
6C	Square	6"x6"x12"	0.15	0.20	6.24	9	Aramid
6D	Square	6"x6"x12"	0.20	0.20	6.24	12	Aramid
6E	Square	6"x6"x12"	0.05	0.98	6.24	3	Aramid
6F	Square	6"x6"x12"	0.10	0.98	6.24	6	Aramid
6G	Square	6"x6"x12"	0.15	0.98	6.24	9	Aramid
6H	Square	6"x6"x12"	0.20	0.98	6.24	12	Aramid
6I	Square	6"x6"x12"	0.10	1.50	6.24	6	Aramid
6J	Square	6"x6"x12"	0.15	1.50	6.24	9	Aramid

\*  $t_j$  = jacket thickness, R = corner radius,  $f'_{co}$  = strength of unconfined concrete.

Rochette (1997) indicated that there are two variables that affect the response of fiber-wrapped specimens; corner radius and the thickness of the jacket. Our evaluation of test results indicate that these variables can best be described by  $\left(\frac{2R}{D}\right)\frac{f_{ru}}{f'_{co}}$ , where R is the corner radius, D is the inside dimension of the tube,  $f'$  is the compressive strength of unconfined concrete (concrete core) and  $f_{,,}$  is the ultimate confining pressure as given below

$$f_{ru} = \frac{2f_{ju}t_j}{D} \quad (3.9)$$

where  $f_{ju}$  is the ultimate hoop strength of the jacket, and  $t_j$  is the jacket thickness. Figure 3.22 shows a plot of  $\frac{f'_{ru}}{f'_{cc}}$  versus  $\left(\frac{2R}{D}\right)\frac{f_{ru}}{f'_{co}}$  for all specimens tested by Rochette (1997) as well as the square tubes tested under Phase II. In this figure,  $f'_{cu}$  indicates the ultimate strength of the section, while  $f'_{oc}$  is the maximum (peak) strength of the section. Notice that for circular sections, this ratio is always 1.0, while for square and rectangular sections, depending on the degree of confinement and the corner radius, this value maybe considerably less than 1.0. Also, notice that the  $\left(\frac{2R}{D}\right)$  ratio for circular sections is equal to 1.0, and therefore, only the confining pressure is of any consequence. Revisiting Figure 3.22, it becomes clear that the collective parameters of corner radius and confining pressure dictates whether or not a descending branch will be present in the response curve. It appears that for  $\left(\frac{2R}{D}\right)\frac{f_{ru}}{f'_{co}}$  of less than 10%, the jacket is not very effective in strengthening the concrete core.

Although, there will be considerable additional ductility due to crack dilatancy containment, no strength increase should be expected. Low confining effects may be due to thin jackets; i.e., low  $f'_{ru}$ . or cross-sectional shape; i.e., square or rectangular sections with sharp edges. As the sharp comers are rounded, the jacket becomes more effective. A careful examination of the data in Figure 3.22 reveals that for low confinements and non-circular sections, despite the considerable dispersion, a logarithmic trend can produce a reasonable estimate of the post-peak response. Prior studies on concrete confined with steel indicates that the stress level in a confined concrete zone is not to be dropped below 30% of the confined concrete strength (Yong et al. 1988). Mugurmna et al. (1992) proposed that this plateau be at 50% of the confined concrete strength. Bjerkly et al. (1990) have attributed this post-peak minimum stress level to the degree of confinement. Although a logarithmic

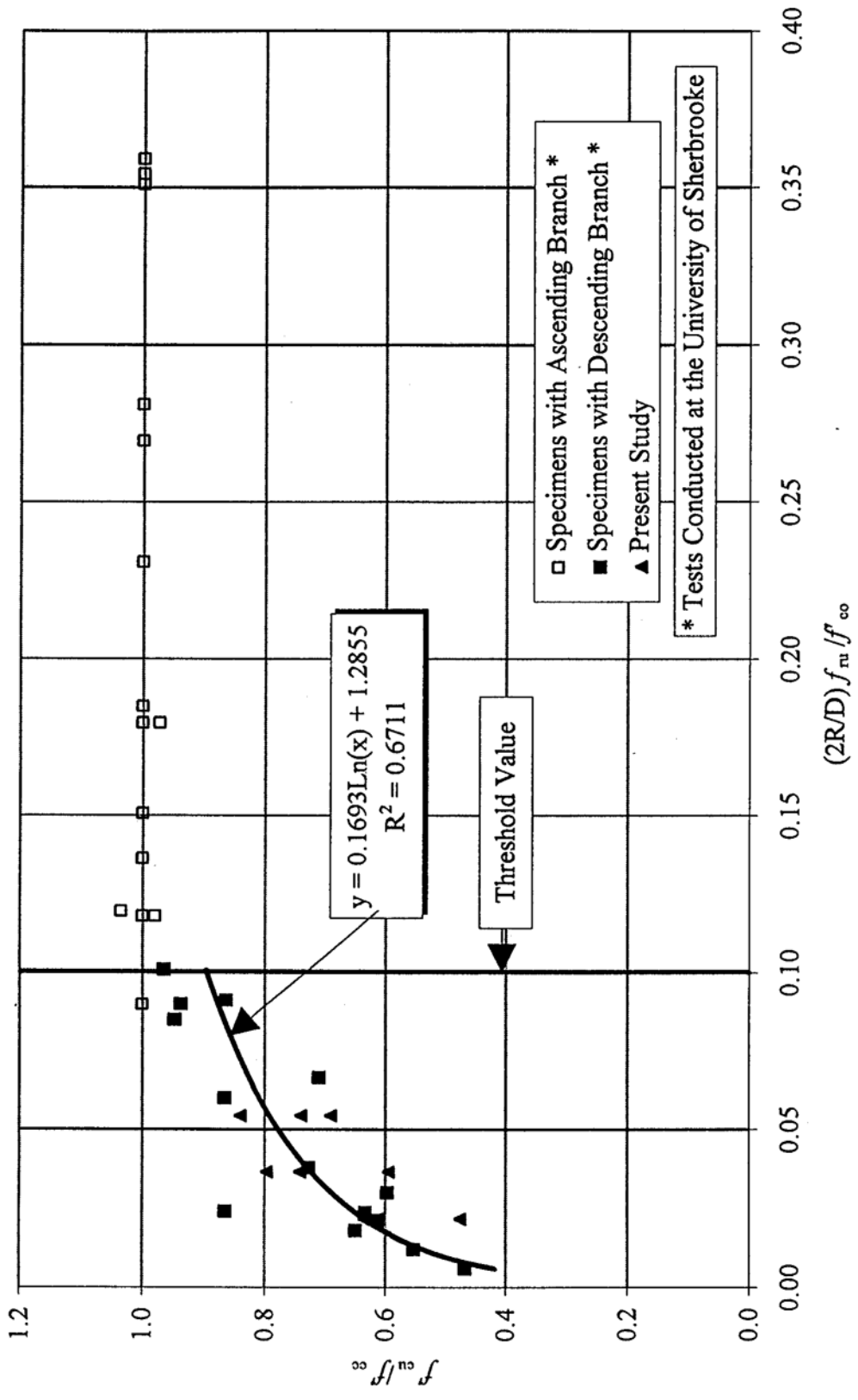


Figure 3.22 Ultimate strength ratio versus  $(2R/D)f_{ru}/f_\infty$

trend does not render a value for  $\left( \frac{2 R}{D} \right) \frac{f_{ru}}{f'_{\infty}} = 0$  , it is not expected that exact sharp corners or

zero confinement be of any concern in the confinement analysis. Therefore, the following relationship is proposed for the post-peak minimum stress level:

$$\frac{f'_{cu}}{f'_{cu}} = 0.1693 \operatorname{Ln} \left[ \left( \frac{2 R}{D} \right) \frac{f_{ru}}{f'_{\infty}} \right] + 1.2855 \quad ( R^2 = 67.11\% ) \quad (3.10)$$

where  $R^2$  represents the statistical correlation.

## CHAPTER 4

### EFFECT OF COLUMN LENGTH ON CONFINEMENT

#### 4.1 Literature Review

Of the main characteristics of FRP-reinforced concrete are the low stiffness and high " deformability as compared to conventional steel-reinforced concrete. Therefore, it is necessary to revisit the effect of lateral deflections and secondary moments on the load-carrying capacity of beam columns reinforced with FRP. Concrete columns may be reinforced internally with FRP reinforcing bars, or externally by encasing concrete in an FRP tube which also serves as the pour form. Even though the confining characteristics of the two reinforcing methods are very different, the slenderness effects can be studied under the same principles.

In contrast with the vast database available on FRP-reinforced beams and slabs, literature on beam-columns is few and limited. The primary concerns for FRP-reinforced concrete columns include: ultimate strength, ductility, confinement, and slenderness. Paramanatham (1993) and Daniali and Paramanatham (1994) studied the behavior of FRP-reinforced concrete columns, and developed equations similar to those in the ACI building code. They tested fourteen 8"x8"x72" columns reinforced with E-glass/vinylester rebars under combined axial and flexural loading, and concluded that FRP rebars in compression would only be stressed up to 20%-30% of their strength. In pure flexure, they noted that the maximum tensile stress in FRP rebars was about 70% of their ultimate strength. Kawaguchi (1993) tested twelve 6"x8"x56" concrete columns reinforced with aramid rebars and subjected to eccentric tension or compression. He noted a rather small ductility for the columns, however, as for the analytical procedure, he did not find any marked difference with the conventional reinforced concrete. Kobayashi and Fujisaki (1995) tested a multitude of 8"x8"x26" concrete columns reinforced with aramid, carbon, or glass rebars under concentric loads, and concluded that ductile failure of concrete columns depends very much on the compressive strength of FRP reinforcement. They also noted that compressive strength of FRP rebars could be as low as 10% of their tensile strength. Amer, et al. (1996) tested eight 6"x6"x96" concrete columns reinforced with four 0.3" diameter carbon rebars under various eccentric loads. They noted considerable differences of up to 37% between their theoretical and experimental values for axial loads. Use of concrete-filled FRP tube with no internal reinforcement as a structural column is unique and innovative (Mirmiran and Shahawy 1995). The experimental interaction diagram of five 7"x7"x52" concrete-filled FRP tubes made of E-glass/polyester corresponded to a reinforced concrete column of the same cross section with more than 5% steel rebars (Mirmiran 1997). However, test results indicated that secondary moments could be of great significance due to low stiffness of FRP materials. Therefore, length effects need to be considered.



## 4.2 Length Effect Tests

To evaluate the effects of length-to-diameter and diameter-to-thickness (LAD and D/t) ratios of the column on confinement of concrete, a series of tests was conducted. It has been stated (Harries 1997) that specimens with LAD ratio of 2:1 can not truly represent confinement of concrete. The reason being the friction zone that is created at each end plate which further prevents lateral expansion of concrete beyond the resistance of the confining jacket. Therefore, the question is the extent of this friction zone, and how it affects the confinement at the mid-height of the specimen. Assuming a 45° distribution angle, for a 12" cylinder a 6" central section still exists that stays free of the effects of the friction zone of the end plates. However, to evaluate the effect of the end plates on the confinement mechanism, and to see if strength or ductility of the member changes with separation of the end plate friction zones, this series of tests was carried out. It is also necessary to evaluate the L/D ratio for which slenderness is not critical. Finally, another objective of this research was to make necessary refinements to the proposed confinement model of Phase I (Mirmiran 1997).

### Specimen Layout

A total of 24 composite specimens with three different tube thicknesses (6, 10, and 14 layers) and four different lengths (12", 18", 24", and 30") were tested. Table 4.1 shows the test matrix and instrumentation. For each tube length and thickness two identical samples were prepared for repeatability verification. The tubes were labeled by the character S (for slenderness), number of plies (6, 10, or 14), length (12, 18, 24, or 30), and sample number (1 or 2). The ply arrangement, tube thickness, fibers and resin, and winding angle were all the same as specimens of Series D from Phase I (Mirmiran 1997). Tubes were made of E-glass fibers and polyester resin wound at  $\pm 15^\circ$  with respect to the cross section of the tube, or  $\pm 75^\circ$  with respect to the axis of the mandrel. Thickness of the tubes were 0.057, 0.087, and 0.117 inch for the 6, 10, and 14 layer tubes, respectively. The inside diameter of the tubes was 5.71" as controlled by the diameter of the mandrel making the tubes. Therefore, the diameter-to-thickness (D/t) ratios of the 6, 10, and 14 layer tubes were approximately 100, 65, and 50, respectively. Usually, concrete-filled tubes with D/t ratios of less than 50 are considered stocky, while very slender tubes have a D/t ratio of over 100 (US-Japan Planning Group 1992). According to these definitions, the tubes under study are considered to be in between the stocky and very slender columns. Of course, it should be noted that these definitions are made for steel tubes. As for the L/D ratio of the tubes, a range from approximately 2:1 to 5:1 was selected which still qualifies as short column. Therefore, slenderness and secondary moments were not expected to be an issue in these tests. However, eccentricities and slenderness effects are studied in more detail later in this chapter. In addition, three 6"x12" control cylinders were made to determine the average strength of concrete core.

Casting was performed at UCF on February 19, 1997. Concrete was ready mix as delivered from Rinker with a target strength of 4,000 psi, a slump of 4", and maximum aggregate size of 1" (DOT #57). However, the initial slump taken from the truck was zero. Therefore, 2 gallons of water was added to the 1 cubic yard of concrete in the mixer truck. This resulted in a slump of 4". The zero slump concrete was only used in the S14-24-1, S14-24-2, S14-30-1, and S14-30-2. No control cylinder was taken from the zero slump concrete, and therefore, the results for the above 4 specimens should be looked upon with caution, as it is expected that the concrete core in these specimens may

be stronger than the rest. All specimens were grooved near the top and bottom end surfaces, and were capped with sulfur mortar prior to testing, same as specimens of Phase I (Mirmiran 1997). It should be noted that as part of a parallel NSF project, an innovative component was added to this study which was the non-destructive testing, i.e., Acoustic Emission (AE) along with the traditional strain gage and LVDT instrumentation. A discussion of the AE test results are presented in Chapter 7.

Table 4.1 Test matrix for length effect specimens:

Specimen Numbers			Length (in.)	L/D Ratio	No. of Strain Gages	No. of LVDTs	No. of AE Sensors*
6 Plies $t_j = 0.057''$ (D/t = 100)	10 Plies $t_j = 0.087''$ (D/t = 65)	14 Plies $t_j = 0.117''$ (D/t = 50)					
S6-12-1 S6-12-2	S10-12-1 S10-12-2	S14-12-1 S14-12-2	12	2 : 1	4	3	2
S6-18-1 S6-18-2	S10-18-1 S10-18-2	S14-18-1 S14-18-2	18	3 : 1	4	3	2
S6-24-1 S6-24-2	S10-24-1 S10-24-2	S14-24-1 S14-24-2	24	4 : 1	12	3	2 (4‡)
S6-30-1 S6-30-2	S10-30-1 S10-30-2	S14-30-1 S14-30-2	30	5 : 1	12	3	2

\* See Chapter 7 for more details on AE tests.

‡ Only for S6-24-1, 4 sensors were used.

**Instrumentation**

All specimens were instrumented with TML (PL-60) strain gages (60 mm gage lengths). Number of gages for each type of specimen is shown in Table 4.1. The 12" and 18" cylinders were only instrumented at their mid-heights with two vertical and two horizontal gages placed at 180° opposite from each other. The horizontal and vertical gages were glued to the surface of the tube with one gage located on top of the other. The 24" and 30" cylinders were instrumented at the top and bottom quarters as well as mid-height with a total of 12 strain gages arranged similar to that described for the 12" and 18" cylinders. Figure 4.1 shows the strain gage arrangements for the tubes. In addition to surface gages, three LVDTs were used for each specimen to measure the average axial strains. Control cylinders were only instrumented with LVDTs.

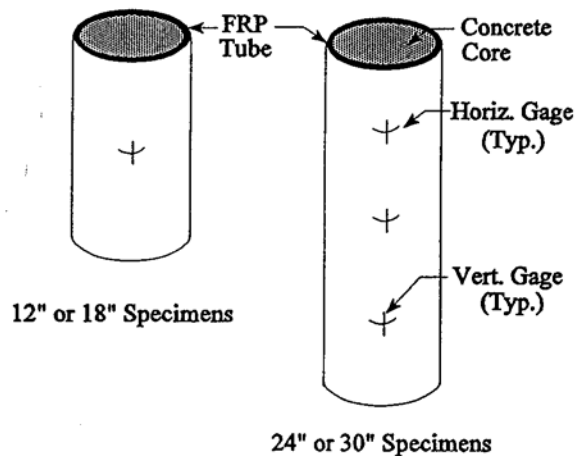


Figure 4.1 Instrumentation of composite tubes

## Test Procedure

All specimens of this series were tested on May 13-15, 1997 at the FDOT Structures Lab at the age of 83-85 days. Three of the specimens (S14-18-2, S6-24-2, and S10-24-1) fell on the floor during the handling process, and were slightly damaged. These were then marked for comparison. However, all but one (S6-24-2) failed at about the same ultimate load as others when tested. A monotonic loading at a rate of 0.22 inch per minute as in Series D of Phase I was applied to all specimens. Tests were conducted using a 550-kip MTS machine, and data were recorded by a Mega DAQ data acquisition system. Figure 4.2 shows the test set up and one of the composite specimens with full instrumentation. All specimens were tested under uniaxial compression.

## Observed Behavior

General failure mode of composite specimens was not any different from that observed in, Phase I. Typical failure was marked by fiber rupture at point of maximum stress concentration, which was preceded by snapping of inner layers of the tube, appearance of white patches, and noises from inside the tube. White patches were indicative of the flow of resin, leaving white glass fibers to take the load. Sounds heard during the early to middle stages of loading were attributed to the micro cracking of concrete and shifting and settling of aggregates. Snapping of the inner layers of the fiberglass could be heard near the end of the loading process. Failure, while sudden, was physically detectable and predictable. Although some local buckling and waving in the tubes were observed, shear failure was noted as the primary mode of failure for the tubes. It was also noted that specimens typically remained intact after failure. No form of violent failure was observed. Location and extent of fiber rupture for each specimen is indicated in Table 4.2. In the group of the 12" specimens, all but two failed at or around the middle band. One of these two specimens (S 14-12-2) failed at the top groove. This specimen was also the only one in the entire series that failed due to the weakness at the groove, and upon its failure, except for the grooved ring that came off the specimen remained intact. In the group of the 18" specimens, on the other hand, all but two failed at the top or bottom quarters. In the group of the 24" specimens, all but one failed at somewhere away from the mid-height. Finally, in the group of the 30" specimens, no single specimen fractured at mid-height. Slenderness effects in the form of buckling, even if present, was not noticeable during the tests or when photos of failed specimens were being taken. Later, analysis revealed that only minor eccentricities were present. Figures 4.3-4.5 show the 18" (14 layers), 24" (6 layers), and 30" (10 layers) specimens after failure.

## Test Results

Recorded data from Mega DAQ was reduced and adjusted for the balance load and the initial straining of the capping materials same as in Phase I (Mirmiran 1997). After careful review of all readings from strain gages and LVDTs, average values were obtained to represent actual strains for each specimen. Test results for the control and composite specimens are summarized in Table 4.2. In this table,  $t_j$  is the tube thickness,  $L$  is the overall length of the specimen including the capping materials,  $f'_{cu}$  is the ultimate strength,  $f'_{co}$  is the average strength of concrete core,  $f_c$  is the confining pressure provided by the jacket, and  $\epsilon_{cu}$  and  $\epsilon_{ru}$  are the ultimate axial and lateral strains, respectively. The table clearly shows that considerable increase in strength and ductility can be achieved regardless of the length of the column, and that length effects are not very significant.

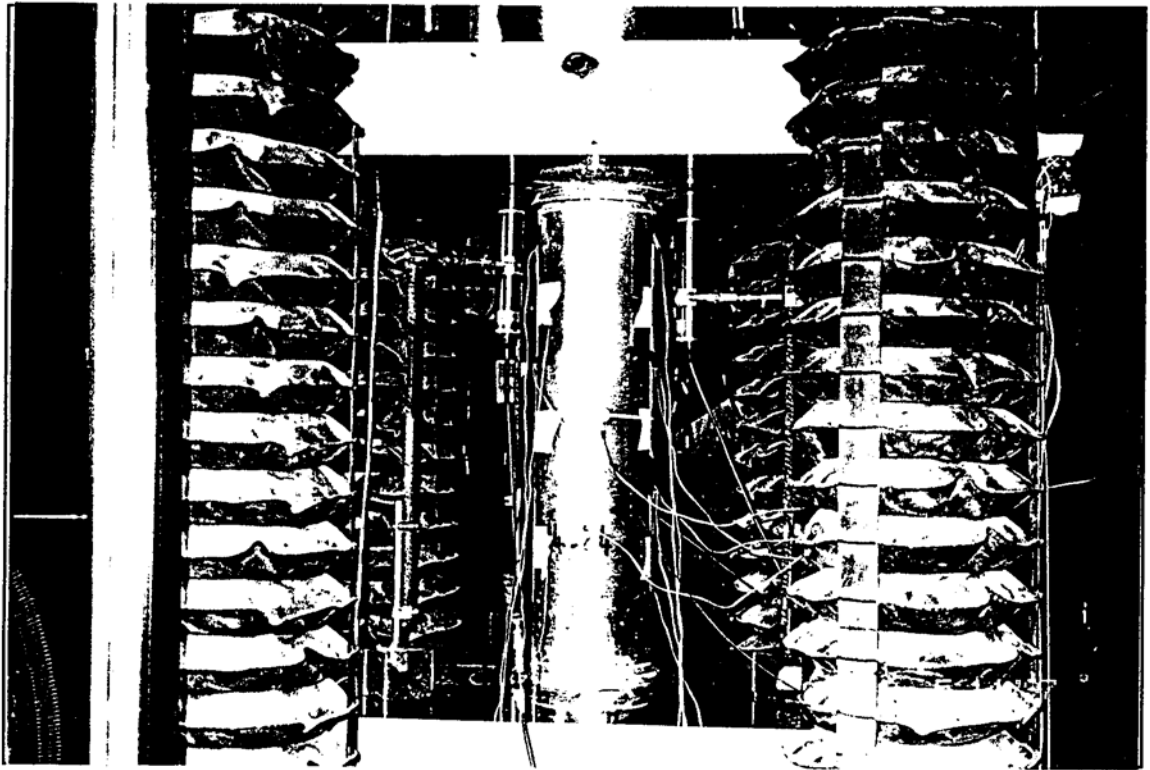


Figure 4.2 Composite specimen with full instrumentation prior to loading

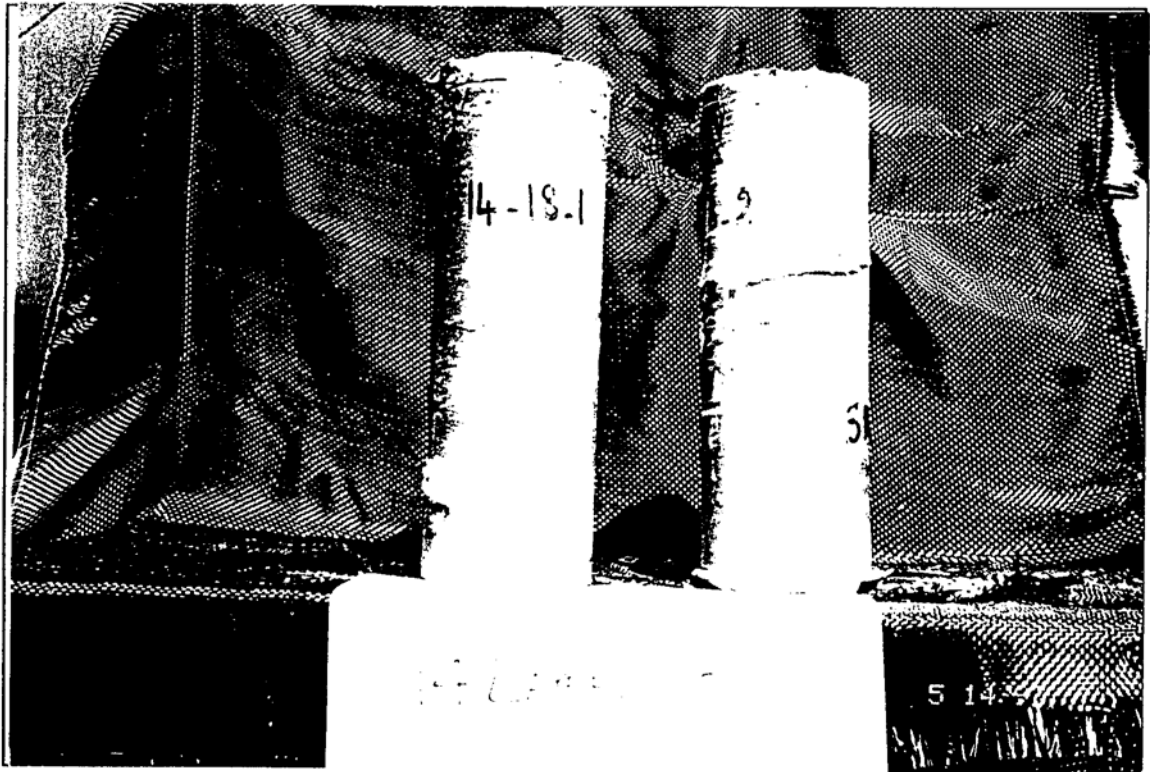


Figure 4.3 14-ply 18" tall specimens after failure